Synergistic targeting of ovarian cancer cells through simultaneous inhibition of key metabolic enzymes

Dissertation

zur Erlangung des Doktorgrades der Naturwissenschaften
- Dr. rer. nat. -

angefertigt am Biochemischen Institut
Fachbereich Medizin und dem Fachbereich Biologie und
Chemie der Justus-Liebig-Universität Gießen

vorgelegt von

Jan Dreute

Gießen, Juli 2023

Dekan: **Prof. Dr. Thomas Wilke**
Institut für Tierökologie und Systematik
Fachbereich Biologie und Chemie
Justus-Liebig-Universität Gießen

1. Gutachter: **Prof. Dr. Reinhard Dammann**
Institut für Genetik
Fachbereich Biologie und Chemie
Justus-Liebig-Universität Gießen

2. Gutachter: **Prof. Dr. M. Lienhard Schmitz**
Biochemisches Institut
Fachbereich Medizin
Justus-Liebig-Universität Gießen

Eidesstattliche Erklärung

„Ich erkläre: Ich habe die vorgelegte Dissertation selbstständig und ohne unerlaubte fremde Hilfe und nur mit den Hilfen angefertigt, die ich in der Dissertation angegeben habe. Alle Textstellen, die wörtlich oder sinngemäß aus veröffentlichten Schriften entnommen sind, und alle Angaben, die auf mündlichen Auskünften beruhen, sind als solche kenntlich gemacht. Ich stimme einer evtl. Überprüfung meiner Dissertation durch eine Antiplagiat-Software zu. Bei den von mir durchgeführten und in der Dissertation erwähnten Untersuchungen habe ich die Grundsätze guter wissenschaftlicher Praxis, wie sie in der „Satzung der Justus-Liebig-Universität Gießen zur Sicherung guter wissenschaftlicher Praxis“ niedergelegt sind, eingehalten.“

Jan Dreute
Gießen, 28. Juli 2023

Table of contents

1 Introduction

1.1 Cancer

1.1.1 Overview

The human body consists of approximately 37 trillion cells, each containing about 3 billion basepairs. A single base mutation but also epigenetic changes at a specific genomic location can be the starting point for cancer. Cancer is a family of diseases defined by the uncontrolled growth and spread of abnormal cells. It is one of the leading causes of death worldwide and affects humans of all ages, races and ethnicities (Cooper, 2000).

Mutations are caused by DNA damage, replication errors or can also occur spontaneously. External factors such as ionizing radiation, ultraviolet radiation from the sun, exposure to chemicals, toxins, air pollution, smoke, viral infections, diet, obesity, and age are amongst the most prevalent inducers of DNA mutations (Huebner and Todaro, 1969; Leanderson and Tagesson, 1992; Morris, Eddleston and Crook, 1995; De Pergola and Silvestris, 2013; Schuch *et al.*, 2017; Turner *et al.*, 2020). Additionally, internal factors such as errors in DNA replication, DNA damaging reactive oxygen species (ROS) and inherited mutations contribute to cancer development (Brown, 2002; Poirier, 2004; Ogrunc *et al.*, 2014; Srinivas *et al.*, 2019; Lucas *et al.*, 2021). Such DNA mutations can lead to changes of the encoded protein or they also occur in non-coding DNA and lead to changes in expression levels or chromatin architecture (Akdemir *et al.*, 2020; Rheinbay *et al.*, 2020). To avoid mutations, cells closely monitor their genome integrity to detect DNA damage and repair lesions (Jiricny, 2006; Sedgwick *et al.*, 2007). Sometimes these repair mechanisms fail, or the extent of DNA damage is too great, eventually leading to mutations (Chatterjee and Walker, 2017). Although mutations can be harmful, some have no effect at all or may even be beneficial as part of natural selection (Desai and Fisher, 2007).

1.1.2 Proto-oncogenes and tumor-suppressor genes

Proto-oncogenes and tumor-suppressor genes are important for normal cell function as they regulate proliferation and division (Nordling, 1953; Lee and Muller, 2010). Mutations however, can transform proto-oncogenes into oncogenes in several ways: (I) overexpression/amplification (e.g., Myc), (II) loss of suppression or hyperactivation (e.g., Kras^{G12V}, PI3K^{E545K}) or (III) chromosomal translocation, resulting in harmful fusion proteins (e.g., BCR-ABL) (Pearson, Edamura and Cleary, 2005; Ligresti *et al.*, 2009; Dang, 2012; Kang *et al.*, 2016; J. Zhang *et al.*, 2020). The most prominent tumor-suppressor gene is *TP53*, which is mutated in many cancers (Giacomelli *et al.*, 2018; Mantovani, Collavin and Del Sal, 2019). Mutations in the DNA binding domain of p53 suppress its function as a transcription factor (Muller and Vousden, 2013). Since p53 is the central DNA damage sensor of the cell, loss of function leads to accumulation of DNA damage and more mutations, eventually resulting in cancer-development according to the multi-hit model of carcinogenesis (Sutherl and Bailar, 1984; Yue *et al.*, 2017; Chernoff, 2021).

1.1.3 Hallmarks of cancer

The Hallmarks of Cancer concept proposed by Douglas Hanahan and Robert Weinberg in 2000 has become a cornerstone of cancer research (Hanahan and Weinberg, 2000). The hallmarks of cancer refer to the essential changes that occur in normal cells when they transform into cancer cells. More and more hallmarks are added regularly (Hanahan and Weinberg, 2011; Hanahan, 2022). To date, there are ten hallmarks of cancer (Fig. 1), which are (1) sustained proliferative signaling, (2) evasion of growth suppressors, (3) resistance to cell death, (4) acquirement of replicative immortality, (5) promotion of invasion and metastasis, (6) promotion of angiogenesis, (7) immune evasion, (8) deregulated energy metabolism, (9) genome instability leading to mutations and (10) tumor-promoting inflammation. As harmful as these hallmarks may be, they also serve as a possible point of intervention for the development of cancer therapies (Buckley *et al.*, 2020).

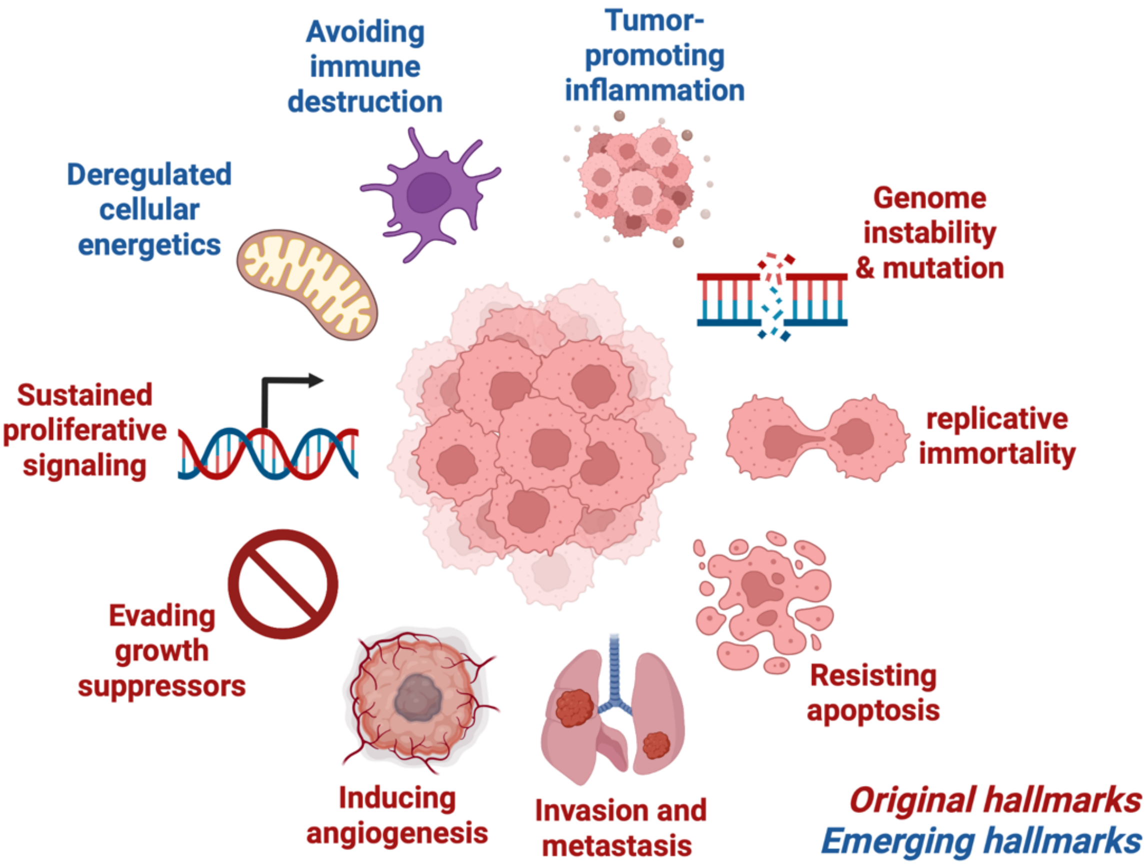

Fig. 1: The hallmarks of cancer.
Original and emerging hallmarks highlighted (Hanahan, 2022). Created with BioRender.

1.2 High-grade serous ovarian cancer

1.2.1 Overview

The collective term ovarian cancer describes a highly heterogenous disease comprised of at least four histologically and molecularly distinct types of cancer, namely endometroid, mucinous, clear cell and serous ovarian carcinoma (Lisio *et al.*, 2019). These subtypes can be divided into two groups, Type I and Type II (Khashaba *et al.*, 2022). Type I or low-grade ovarian cancers are slow growing, generally confined to the ovary and do not show genetic instability. Type II or high-grade ovarian cancers progress rapidly, metastasize and exhibit wide-spread DNA copy number alterations as a result of genetic instability (Am and R, 2010; Koshiyama, Matsumura and Konishi, 2014, 2017; Lisio *et al.*, 2019).

Up to 75% of ovarian cancer patients are diagnosed with high-grade serous ovarian cancer (HGSOC) (Torre *et al.*, 2018; Arora, Mullangi and Lekkala, 2022;

Dalmartello *et al.*, 2022). HGSOC is not only the most common form of ovarian cancer, but by far the deadliest gynecologic cancer worldwide, with a 5-year survival rate of only about 35% (Reid, Permuth and Sellers, 2017; Radziszewska *et al.*, 2018; Wu *et al.*, 2019). The main reason for this high lethality is its asymptomatic nature, which results in a very late diagnosis (Sipos *et al.*, 2021; Asangba *et al.*, 2023). At this point, the cancer has usually spread to both ovaries, the abdomen, the liver and the peritoneum, which is classified as stage III or IV (Lengyel, 2010; Lisio *et al.*, 2019).

1.2.2 Development

The pathogenesis of HGSOC is still unclear and several hypothetical models suggest the mechanisms leading to the development of this disease. Although it is likely that HGSOC has various cellular origins (Am and R, 2010; Zhang *et al.*, 2019; Colvin and Howell, 2020), the most widely accepted model is the "incessant ovulation" model defined by Fathalla (Fathalla, 1971). During the menstrual cycle, the follicle, which encapsulates the oocyte, is maturating and moves towards the cortex of the ovary. Ovulation begins 13 to 14 days after the onset of the menstrual cycle. During ovulation, the follicle releases proteolytic enzymes that digest the follicular membrane and the ovarian surface epithelium (Thiyagarajan, Basit and Jeanmonod, 2022). This process involves the destruction of intact cells, causing release of proinflammatory cytokines and other mediators such ROS and estrogens, which together create a unique milieu likely to cause DNA damage to cells in close proximity to the ovary (Agarwal, Gupta and Sharma, 2005). In particular, it has been shown that secretory epithelial cells located at the distal fimbriae of the fallopian tube can undergo malignant transformation leading to the development of high-grade serous ovarian cancer (Kindelberger *et al.*, 2007; Lee *et al.*, 2007; Erickson, Conner and Landen, 2013; Labidi-Galy *et al.*, 2017a). The cancerous transformation of fallopian tube secretory epithelial cells (FTSECs) is initiated through mutations in the *TP53* gene, decreasing the ability of p53 to sense DNA damage and orchestrate an adequate DNA damage response (Eckert *et al.*, 2016; Bronder *et al.*, 2021). This p53 signature is present in up to 96% of patients and therefore considered to be the hallmark of HGSOC, also suggesting that loss of p53 function is the starting point for cancer development (Bell *et al.*, 2011; Cole *et al.*, 2016; Tuna *et al.*, 2020). Repetitive genotoxic stress (monthly ovulatory cycles) leads to the accumulation of more mutations eventually resulting in serous tubal intraepithelial carcinoma (STIC) (Byun *et al.*, 2023) (Fig. 2). With time, a STIC will transform into HGSOC in a step-wise fashion, which will further spread into distant organs (Am and R, 2010; Nakamura *et al.*, 2017; Mei *et al.*, 2021).

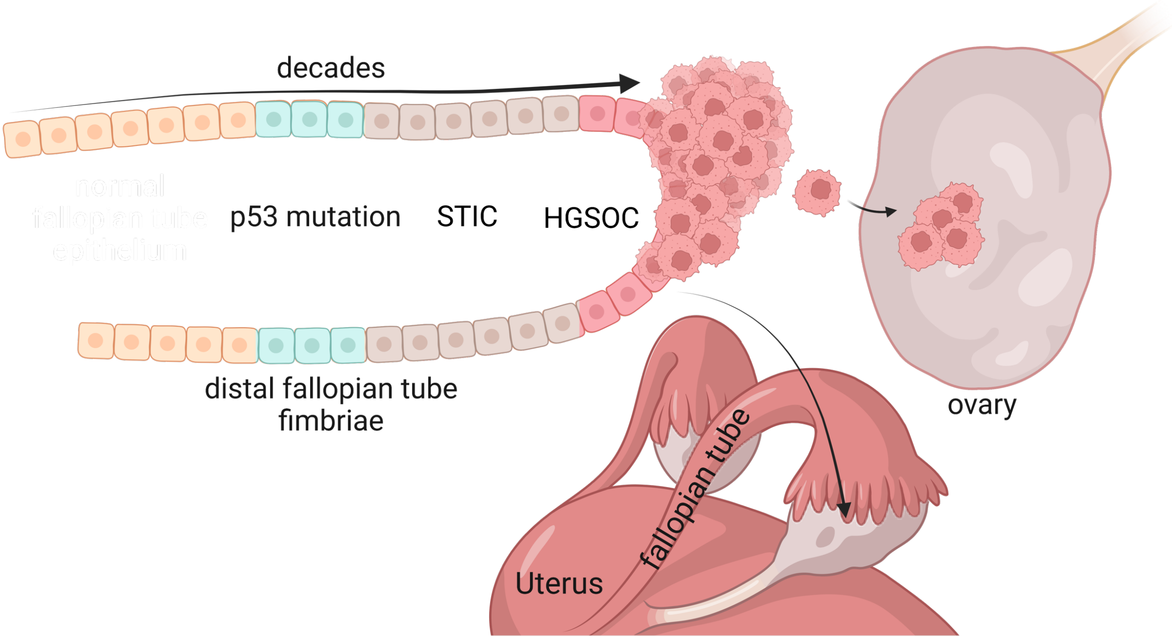

Fig. 2: Development of high-grade serous ovarian cancer.
Secretory epithelial cells, located at the distal fimbriae of the fallopian tube, are exposed to repeated genotoxic stress by ovulation. After acquiring p53 mutations, the accumulation of further mutations leads to serous tubal intraepithelial carcinoma, which progresses to invasive HGSOC. Created with BioRender.

1.2.3 Mutational landscape

The cancer genome atlas project (TCGA) analyzed 489 clinically annotated stage II - IV HGSOC cancer samples with respect to their mutational status and alterations in DNA copy number, expression of mRNA and miRNA, DNA methylation and protein expression. Thus, the TCGA dataset provides the most comprehensive report describing the molecular alterations of HGSOC (Bell *et al.*, 2011).

The mutational landscape of HGSOC is relatively narrow (Bell *et al.*, 2011). Next to the omnipresent p53 signature, some of the most frequently observed genetic alterations are found for *RB1, CDK12, NF1, BRCA1 and BRCA2 and MYC* (Yamulla *et al.*, 2020). The prevalence of these individual alterations in patients ranges from 10% to 30%, resulting in a variable mutational landscape that underscores the great patient-to-patient heterogeneity which poses particular challenges to the treatment of this disease. (Schwarz *et al.*, 2015; Kroeger and Drapkin, 2017; Serio *et al.*, 2021). The level of heterogeneity decreases at the level of aberrant signaling pathways. The RB1, PI3K/RAS/Akt1 and NOTCH signaling pathways were found to be deregulated in 67%, 45% and 22% of all cases, respectively (Bell *et al.*, 2011; Martins *et al.*, 2022). This allows subclassification of HGSOC patients with respect to altered signaling pathways, which in turn opens the possibility for more differentiated treatment strategies.

1.2.4 Current treatment strategies

Treatment strategies for HGSOC patients vary depending on their current state of disease progression. At the time of clinical diagnosis, disease progression is typically at stages III - IV, where HGSOC has already spread to both ovaries and the fallopian tubes, the abdominal cavity, the peritoneal cavity and in worst cases to liver, lungs, bones and lymph nodes (Prat, 2015). Dependent on the specific case, the first-line therapy is comprised of debulking surgery to reduce the total tumor burden, followed up by extensive chemotherapy to eliminate residual cancer cells. However, the treatment outcome and the patient’s prognosis are most dependent on the debulking surgery and thereby the surgeon’s skill to remove the primary and secondary tumors. The aim of the debulking surgery is to reduce the diameter of the tumors to less than 1 cm, which is only achieved in 25 - 40% of cases worldwide (Dauplat *et al.*, 2000).

As HGSOCs are very sensitive to the chemotherapeutic agents carboplatin and paclitaxel, combination of these two drugs is the current standard therapy (Luyckx *et al.*, 2022). After first disease recurrence or initial resistance to chemotherapy, carboplatin-gemcitabine in combination with targeted therapeutics is the standard of care (Mahmood *et al.*, 2020).

Targeted therapies in HGSOC are primarily considered for patients whose tumors exhibit homologous recombination (HR) deficiency (Gadducci *et al.*, 2019). HR-deficient tumors are characterized by mutations in *BRCA1/2* genes (or other HR-related genes) which make them susceptible to PARP inhibitors (e.g., Olaparib) (Cojocaru, Parkinson and Brenton, 2018). BRCA1/2 and PARP1/2 play a role in the DDR pathway, which promotes HR to repair DNA damage. When BRCA1/2 are mutated and therefore functionally impaired, inhibition of PARP1/2 results in synthetic lethality due to accumulation of DNA damage (Helleday, 2011).

Although first-line and targeted therapies can convert many HGSOCs into chronic diseases, 5-year survival rates have only been slowly increasing in recent decades, making the discovery of new and more effective therapies urgent (J.-Y. Lee *et al.*, 2018). One possibility as to why current treatment strategies have not had a significant impact on survival rates is that they have focused exclusively on the characteristics of cancer cells and have not taken into account the complex and diverse interactions and cell-cell communications of the human body with cancer cells (Klemm and Joyce, 2015). Therefore, recent studies have shifted their focus from exclusively treating cancer cells to treating and modifying the tumor microenvironment (TME) (Klemm and Joyce, 2015).

1.2.5 The tumor microenvironment

The heterogeneity of HGSOC is also reflected on the level of the TME, which can have anti- and pro-inflammatory properties within the same patient (Jiménez-Sánchez *et al.*, 2020). The cellular components of the TME comprise stromal cells including cancer cells, cancer-associated fibroblasts (CAFs), immune cells, endothelial cells, and many more cell types (Wei *et al.*, 2020; Li *et al.*, 2021). The humoral components of the TME consists of a variety of soluble factors secreted by the tumor and immune cells. They include chemokines and cytokines (e.g., CXCL-2, IL-6), proteases (e.g., MMPs) and metabolites (e.g., lactic acid, kynurenine) (Yang *et al.*, 2020). Depending on the cell types involved and the signaling molecules they release, this complex environment can have either tumor-inhibiting or tumor-promoting effects. Anti-tumor microenvironments are typically characterized by the detection of M1 tumor-associated macrophages (TAMs), Th1 cells, and CD8$^+$ cytotoxic T cells (Baghban *et al.*, 2020). Cancer cells may also contribute to the anti-tumor microenvironment as they activate immune cells through damage-associated molecular patterns (DAMPs). However, in most TMEs, cancer cells secrete anti-inflammatory molecules to reprogram fibroblasts into CAFs or inflammatory M1- into immunosuppressive M2-TAMs (Gordon, 2003; Yang *et al.*, 2020; Gómez-Valenzuela *et al.*, 2021; Simón *et al.*, 2022). In addition, the TME is able to exhaust T cells, promote differentiation into regulatory T cells and inhibit dendritic cell maturation, resulting in an overall suppression of the immune system and immune evasion of cancer cells (Jiang, Li and Zhu, 2015; Di Blasio *et al.*, 2020; Li *et al.*, 2020; Z. Zhang *et al.*, 2020).

Most therapeutic strategies designed to remodel the TME focus on its cellular components by directly interfering with the adverse functions CAFs, M2-TAMs, regulatory T cells, or cancer cells (Tang *et al.*, 2013; Chen and Song, 2019; Shan *et al.*, 2022). The most recent milestone was achieved through immune checkpoint therapy (Leach, Krummel and Allison, 1996; Robert, 2020). Immune checkpoints are receptors on T cells that suppress T cell function (e.g., through T cell exhaustion and apoptosis) after binding a ligand. Prominent examples for immune checkpoints are PD-1/PD-L1 and CTLA-4. PD-L1, for example, shows a wide range of expression on immune cells and, most importantly, on cancer cells (Wang *et al.*, 2016). Expression can be induced by many factors of the TME, including TGF-ß, IL-7/15/21 and IFN-α (Yi *et al.*, 2021). The current strategy to overcome PD-1 mediated immune suppression is to interfere with PD-1/PD-L1 interaction. This is achieved by using monoclonal antibodies directed against either PD-1 or PD-L1 (De Sousa Linhares *et al.*, 2019).

CTLA-4 is mainly expressed on activated T cells and inhibits T cell function by binding to members of the B7 family (Wu *et al.*, 1997; Chikuma, Abbas and Bluestone, 2005). This interaction triggers the secretion of IDO1, an enzyme which catabolizes tryptophan to kynurenine. Kynurenine is an immunosuppressive metabolite which was shown to inhibit CD8$^+$ T cell tumor-infiltration and T cell proliferation (González *et al.*, 2008). However, the main mechanism of CTLA-4-mediated T cell inhibition involves suppression of the co-stimulatory receptor CD28 (Rudd, Taylor and Schneider, 2009). Monoclonal antibodies against CTLA-4 suppress its signaling ability by interfering with the binding of B7 family members (Tarhini and Iqbal, 2010).

Interference with immune checkpoints was shown to remarkably affect the composition of the TME and, together with other adjuvant therapies, might be able to drastically increase the overall survival rate of patients in the future (Petitprez *et al.*, 2020).

1.3 The cellular energy metabolism

1.3.1 Overview

The core of cellular energy metabolism to be discussed here consists of glycolysis, the citric acid cycle, and oxidative phosphorylation. While the latter exclusively leads to the generation of adenosine triphosphate ATP, the other pathways also create building blocks to be used in other anabolic or catabolic pathways. Other important metabolic pathways are the pentose phosphate pathway (leading to the synthesis of pentoses), lactate fermentation (sustaining glycolysis in the absence of sufficient oxygen), glutaminolysis (for anaplerotic reactions) and fatty acid ß-oxidation (generating reducing equivalents) (Spinelli and Haigis, 2018).

1.3.2 Glycolysis and lactate fermentation

In glycolysis, one molecule of glucose is converted to two molecules of pyruvate through different enzymatic reactions, which produces 2 molecules of ATP and NADH. Glycolysis derived pyruvate can then enter lactate fermentation or the citric acid cycle after being converted to Acetyl-CoA. During lactate fermentation, pyruvate is converted into lactate by the enzyme family of lactate dehydrogenases (LDH). This reaction requires NADH as a cofactor for LDH, which recycles NADH to NAD^+, an important cofactor for glycolysis (Chaudhry and Varacallo, 2022). The LDH reaction is especially important under conditions of limited oxygen availability, as it serves the regeneration of reducible NAD and thus maintains glycolysis.

1.3.3 Citric acid cycle and oxidative phosphorylation

The citric acid cycle is a central hub of metabolism and therefore plays a central role as the starting or end point of many anabolic and catabolic pathways (Haddad and Mohiuddin, 2022). The breakdown byproducts of sugars, fatty acids, and amino acids join the citric acid cycle through various entry points. In addition to its important role as a hub for metabolites, the citric acid cycle produces 1 GTP as an energy carrier, 2 CO_2 as waste, and 3 NADH and 1 $FADH_2$, which are further used in oxidative phosphorylation.

Oxidative phosphorylation, the last step of cellular respiration, is the process that generates most of the cell's energy (Deshpande and Mohiuddin, 2022). Oxidative phosphorylation occurs in the electron transport chain (ETC) and is comprised of four multiprotein complexes located in the inner mitochondrial membrane. The electron transport chain is a series of redox-reactions that uses electrons donated from NADH and $FADH_2$ to build up a proton gradient in the mitochondrial intermembrane space. This proton gradient will further be used by the F_1F_0-ATP synthase. The ATP-synthase is located in the inner mitochondrial membrane with its F_1-domain protruding into the mitochondrial matrix. The protons, driven by the proton motive force, flow through the F_0-domain, causing the γ subunit of the F_1-domain to rotate. This rotation induces a conformational change of several subunits that lead to the binding of ADP to a phosphate group, forming ATP. ATP is then released into the mitochondrial matrix and further distributed.

1.4 Tryptophan metabolism

Tryptophan is an essential amino acid and serves as a precursor for many molecules in the human cell (Richard *et al.*, 2009). In general, tryptophan metabolism can be divided into the serotonin/melatonin pathway and the kynurenine pathway.

The serotonin/melatonin pathway is needed for the generation of its name given neurotransmitters, which can regulate sleep and cognitive function. The kynurenine pathway is a *de novo* biosynthetic pathway for NAD^+ (Savitz, 2020). The first and rate-limiting reaction, in which L-tryptophan is converted to N-formylkynurenine, is catalyzed by the enzymes tryptophan 2,3-dioxygnase (TDO) or indoleamine 2,3-dioxygenase (IDO). N-formylkynurenine is then hydrolyzed to L-kynurenine. L-kynurenine can be further converted to the end products of the kynurenine pathway by stepwise enzymatic cascades: Quinaldic acid, 8-hydroxyquinaldic acid, picolinic acid, glutaryl-CoA, or quinolinic acid. Quinolinic acid serves as a precursor for the formation of NAD^+ (Castro-Portuguez and Sutphin, 2020).

1.5 Cancer metabolism

Cancer cells must drastically adjust their metabolism to meet their increasing demands for energy and biomass production to support, for example, their increased proliferation rate. One such metabolic adaptation was described by Otto Warburg in the 1920s (Warburg, 1956). He discovered a significant upregulation of glycolysis in cancer cells. Although glycolysis produces less ATP when compared to oxidative phosphorylation, this metabolic reprogramming allows the generation of more building blocks for the synthesis of macromolecules. In addition, it allows the cancer cell to proliferate even in regions with limited oxygen supply (hypoxia), which is often found in solid tumors (Al Tameemi *et al.*, 2019). Finally enhanced glycolysis leads to the production of lactic acid, thus creating an acidic pH to promote tumor invasion and metastasis while inhibiting the immune response (Corbet and Feron, 2017). This metabolic reprogramming also involves the tumor-suppressor p53, which leads to downregulation of anaerobic glycolysis while maintaining oxidative phosphorylation (Maddocks and Vousden, 2011). As the function of p53 is frequently lost in many cancers, the metabolism may shift from oxidative phosphorylation to glycolysis as a consequence. However, cancer cells are highly variable and do not necessarily upregulate anaerobic glycolysis during development. Some cancer types even present with upregulation of oxidative phosphorylation (ZHENG, 2012; Kim and DeBerardinis, 2019).

In addition to the metabolic adjustments in energy metabolism described above, cancer cells must upregulate fatty acid synthesis and amino acid metabolism to meet their increasing demand for building blocks to enable rapid proliferation (Flavin *et al.*, 2010; Butler, Meer and Leeuwen, 2021). More specific metabolic adaptions are strongly dependent on the type of cancer and include: (I) Mutations of metabolic enzymes, for example mutant isocitrate-dehydrogenase (IDH1/2) in gliomas, leading to increased and/or novel metabolic activity (Dang *et al.*, 2009). (II) Oncogene induced metabolic reprogramming was also observed in mutant Ras tumors (Tarrado-Castellarnau, de Atauri and Cascante, 2016). Here, Ras activates the PI3K/Akt-mTOR signaling axis, by which mTOR stabilizes the transcription factor HIF to promote glycolysis and glutaminolysis. Another prominent example is the Myc oncogene. Expression of Myc increases the expression of glutamine transporters and glutaminase (glutaminolysis), as well as LDHA (anerobic glycolysis) (Doherty *et al.*, 2014; Bott *et al.*, 2015).

1.6 Targeting cancer metabolism

Tumor cells, which are dependent on rewired metabolic pathways, become vulnerable to drugs selectively targeting the tumor-specific metabolic pathways. Selective targeting of the cancer cell metabolism has been already pursued in the 1950s where 2-Deoxyglucose (2-DG) has been recognized as a potent inhibitor of glycolysis (Woodward and Hudson, 1954). 2-DG is a synthetic glucose analog which can be phosphorylated to glucose-6-phosphate, but is unable to isomerize to fructose-6-phosphate, leading to its intracellular accumulation and inhibition of glycolysis (Pajak *et al.*, 2020). Therefore 2-DG is a widely used tool to interfere with the proliferation of tumor cells with a pronounced Warburg effect.

More recent advances in the field of metabolic therapy are the clinically approved inhibitors of the mutant enzymes IDH1 and IDH2 for acute myeloid leukemia (AML) (Cerchione *et al.*, 2021). Selectivity for cancer cells is based on the ability of the drugs to specifically target the mutant enzymes, which are commonly found in AML but not in healthy cells.

The emergence of metabolic vulnerabilities concurrent with the development of chemotherapy resistance, represents another therapeutic window. For example, cisplatin-resistant non-small cell lung cancers (NSCLC) have shown to be dependent on glutamine (Obrist *et al.*, 2018). Cisplatin-resistant cell lines use glutamine primarily for the biosynthesis of nucleotides. This metabolic adaptation produced a metabolic vulnerability of cisplatin-resistant cells to antimetabolites targeting the nucleoside metabolism.

Furthermore, mTOR-mediated cancer drug resistance was shown to interfere with autophagy, which generated a novel metabolic vulnerability in NSCLC (Gremke *et al.*, 2020). The suppression of autophagy, a process that counteracts starvation induced stress by providing a variety of metabolites to maintain metabolic homeostasis, sensitized cisplatin-resistant cell lines to 2-deoxyglucose (2-DG) and dichloroacetic acid (DCA), highlighting the susceptibility of cisplatin-resistant cancers to additional metabolic perturbation.

A key problem of today's understanding of altered cancer cell metabolism is the lack of conclusive data regarding the association, dependence or compensation of distinct pathways. Therefore, many studies are based on large scale screening approaches to identify metabolic inhibitors or inhibitor combinations with the ability to efficiently kill cancer cells.

1.7 The concept of synthetic lethality

Conventionally, the dependence of cell viability on two genes is referred to as synthetic lethality (O'Neil, Bailey and Hieter, 2017). Disruption of either gene alone has no effect on cell viability, whereas simultaneous disruption of both genes results in cell death. This is a concept that can be translated from the genetic level to the metabolic level. In this case, perturbation of two different pathways leads to cell death, whereas perturbation of only one pathway has little or no effect.

1.8 Cellular senescence

1.8.1 Overview

When primary cells are cultured, they eventually reach a point where they cease to divide further, known as the "Hayflick limit" (Hayflick and Moorhead, 1961). This restricted ability for cell proliferation is caused by the induction of cellular senescence (Dodig, Čepelak and Pavić, 2019). Senescence can be induced by telomere shortening, DNA damage, oncogene activation and ROS (Kumari and Jat, 2021). Senescence can be considered as a backup mechanism that is activated when cells suffer excessive DNA damage (Baz-Martínez *et al.*, 2016; Kumari and Jat, 2021). Instead of going into apoptosis and being eliminated, cells stop proliferating to reduce stress, conserve energy and upregulate anti-apoptotic signaling pathways to increase their chances of survival (Childs *et al.*, 2014).

Senescence is an extremely versatile program that occurs on the level of the transcriptome, proteome and metabolome. Dependent on the cell type, the senescence triggers, the individual genetic- and epigenetic landscape or the nutritional status, different signaling pathways become important, resulting in a highly variable landscape of senescent phenotypes (Kirschner *et al.*, 2020; Cohn *et* *al.*, 2023). For example, DNA damage-induced senescence leads to cell cycle arrest, mediated by p53-dependent or -independent Rb1 activation and upregulation of the cell cycle inhibitors p16 and p21 (Kumari and Jat, 2021). ROS-induced senescence leads to the induction of the senescence-associated secretory phenotype (SASP), which refers to the unique and characteristic secretion of various molecules by senescent cells (Salminen, Kauppinen and Kaarniranta, 2012).

1.8.2 The role of ROS in senescence

ROS are highly reactive molecules produced by incomplete reduction of oxygen. The main source of ROS is generated in mitochondria through the leakage of electrons in the ETC with complex I and complex III being the main sources (Ray, Huang and Tsuji, 2012). These electrons, together with oxygen molecules produce radicals such as superoxide anions ($O_2 {\cdot}^-$), hydrogen peroxide (H_2O_2) and hydroxyl radicals ($OH{\cdot}$). Elevated ROS levels have been shown to be critical for the induction and maintenance of cellular senescence, however its specific role is not clear. For a long time, the contribution of ROS to senescence was believed to be a paradox (Davalli *et al.*, 2016). ROS is known to be beneficial for cellular proliferation, but at the same time can cause DNA damage, which stops proliferation. This paradoxical role of ROS was partly solved in 2014, where a study showed that ROS induced hyperproliferation led to error-prone DNA replication, DNA damage and consequently the induction of senescence (Ogrunc *et al.*, 2014). The ability of ROS to maintain senescence is believed to be achieved by inducing constant damage to mitochondrial DNA, which is sufficient for a terminal proliferative arrest (Davalli *et al.*, 2016). Senescent cells are also able to release ROS, thereby directly regulating immune cells and interfering with normal tissue homeostasis (Nelson *et al.*, 2018; Weinberg, Ramnath and Nagrath, 2019). However, ROS is only one factor constituting the SASP.

1.8.3 The NF-κB-driven senescence-associated secretory phenotype (SASP)

Although proliferation has stopped, senescent cells are by no means inactive. In addition to high metabolic activity and widespread gene and protein expression changes, senescent cells develop a unique secretion phenotype, the SASP (Coppé *et al.*, 2010; Van Deursen and M, 2014). The SASP is a proinflammatory program, mainly regulated by the NF-κB signaling pathway (Chien *et al.*, 2011; Rovillain *et al.*, 2011). The SASP develops over time in a highly dynamic manner and its constituents include growth factors, cytokines, chemokines, extracellular matrix remodelers. It usually takes up to five days after senescence induction for a full SASP to develop. Not all SASP-constituents begin to be secreted at the same time (Coppé *et al.*, 2010). While a wide variety of secreted factors show significant upregulation upon senescence, the SASP cannot be considered unspecific. The core of secreted factors includes IL-6, IL-8, GROα and GDF-15. Other frequently overrepresented constituents are ROS, nitric oxide, VEGF and matrix-metalloproteases, amongst many others (Basisty *et al.*, 2020). Despite a core set of common factors, the specific composition of SASP depends on the trigger of senescence and the cell type. The SASP is considered as a self-amplifying secretory network in which secreted factors can act in auto-, paracrine, and endocrine ways, resulting in the production of a robust and unique proinflammatory milieu (Ortiz-Montero, Londoño-Vallejo and Vernot, 2017). As this milieu is rich in radicals, senescent cells are consistently exposed to DNA damage, which reinforces the cell cycle arrest and senescence.

1.8.4 Tumor senescence, a two-edged sword

Inducing senescence in tumor cells can be a worthy achievement for tumor therapy as tumor cells do not proliferate any more (Fig.3). On the other hand, the SASP can promote the growth of new cancer cells (Coppé *et al.*, 2010). This dual role of senescence has to be considered when evaluating new senescence inducing treatment strategies. The SASP exerts its deleterious effects by promoting cellular proliferation, increasing cancer metastasis, reprogramming immune cells, reducing regenerative capacity and decrease tissue function. In order to overcome these deleterious effects of senescence, current strategies involve the application of senolytic drugs that are able to selectively eliminate senescent cells (Chaib, Tchkonia and Kirkland, 2022) or senomorphics, which suppress the adverse effects of the SASP (Zhang *et al.*, 2023).

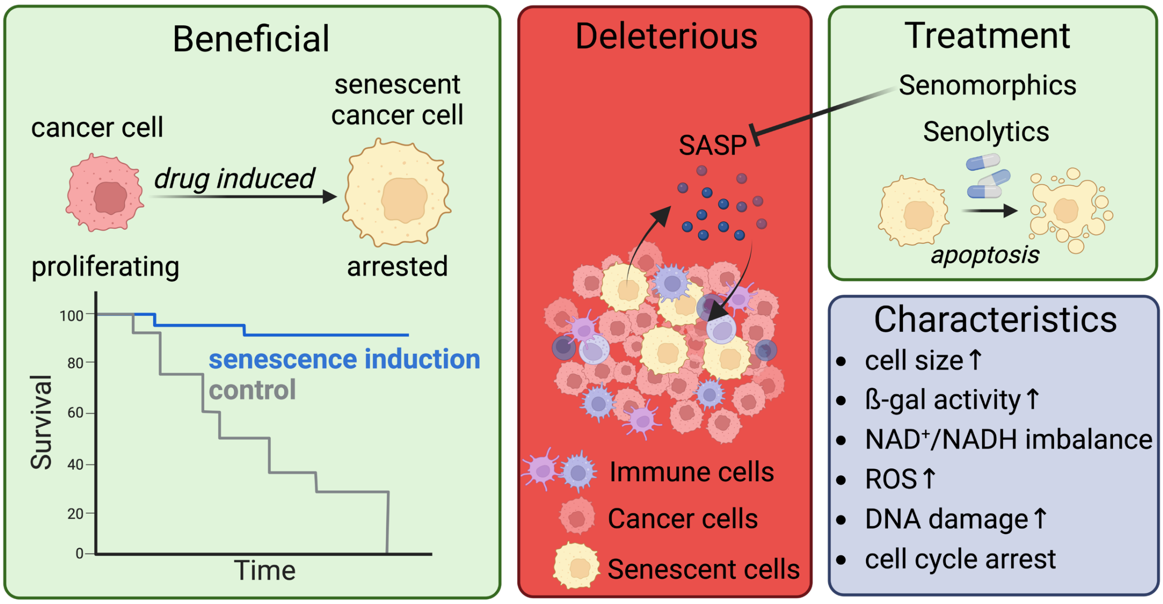

Fig. 3: Beneficial and deleterious effects of cellular senescence.
Inducing senescence in cancer cells reduces tumor burden and increases patient survival. On the contrary, senescent cells develop the deleterious senescence-associated secretory phenotype (SASP). This phenotype constitutes its stability by working in an autocrine self-reinforcing manner. In addition, the SASP deregulates immune-cell function and tissue integrity in a paracrine manner. Several strategies exist to alter the SASP composition through so-called senomorphics or directly eliminate senescent cells via senolytics. The characteristics of senescent cells are highly variable and dependent on the cell-type, tissue-environment, senescence trigger and further parameters. Created with BioRender.

1.9 Aim of this study

Cancer cells drastically reprogram their metabolism to adapt to higher energy and biomass production requirements. These metabolic adaptations distinguish cancer cells from healthy cells. The present study aims to identify novel metabolic vulnerabilities of ovarian cancer. The first objective was to create a suitable model system to compare ‘healthy’ non-cancerous cells with cancer cells. To this end, immortalized fallopian tube cells should be transformed to cancer cells using relevant and well characterized oncogenes. Following initial characterization of these cancer cells for the presence of typical cancer hallmarks, a combinatorial screening of metabolic drugs shall be performed. The aim is to identify a cancer selective drug combination. Further work will address the molecular mechanisms and physiological consequences of this drug combination underlying its inhibitory effect on tumor cell growth.

2 Materials and methods

2.1 Materials

2.1.1 Primary antibodies

Antibody (clone)	Species	Supplier	Dilution
4E-BP1 (52H11)	rabbit mAb	CST	1:1000
ACC (C83B10)	rabbit mAb	CST	1:1000
BrdU [(BU1/75 (ICR1)]	rat mAb	Abcam	1:1000
Cleaved Caspase 3 (9664)	rabbit mAb	CST	1:1000
GAPDH (2G7)	mouse mAb	DSHB	1:200
H2A.X Ser 139 (JBW301)	mouse mAb	Millipore	1:1000
HA-tag (6E2)	mouse mAb	CST	1:1000
IDO1 (D5J4E)	rabbit mAb	CST	1:1000
LDHA (C45B)	rabbit mAb	CST	1:1000
LDHB (14824-1-AP)	rabbit pAb	Proteintech	1:5000
mTOR (7C10)	rabbit mAb	CST	1:1000
MYC (A00704)	mouse mAb	GeneScript	1:500
p16 (G175-1239)	mouse mAb	BD Biosciences	1:500
p21WAF1 (EA10)	mouse mAb	Calbiochem	1:1000
p4E-BP1 Ser 65 (sc-293124)	mouse mAb	Santa Cruz	1:500
p4E-BP1 Thr 37/48 (236B4)	rabbit mAb	CST	1:1000
pACC Ser 79 (3661S)	rabbit mAb	CST	1:1000
pmTOR Ser 2448 (D9C2)	rabbit mAb	CST	1:1000
V5-tag (R960-25)	mouse mAb	Thermo	1:500
Vinculin (V9131.2ML)	mouse mAb	Sigma	1:1000
α-Tubulin (12G10)	mouse mAb	DSHB	1:1000

2.1.2 Secondary antibodies

Antibody	Conjugated to	Supplier	Dilution
goat-anti-mouse IgG	HRP	Dianova	1:5000
goat-anti-rabbit IgG	HRP	Dianova	1:5000
goat-anti-rat IgG	HRP	Dianova	1:5000

Antibody	Conjugated to	Supplier	Dilution
goat-anti-mouse IgG	Alexa Fluor 488	Dianova	1:1000
goat-anti-rabbit IgG	Alexa Fluor 488	Dianova	1:1000
goat-anti-rat IgG	Alexa Fluor 488	Dianova	1:1000
goat-anti-mouse IgG	Alexa Fluor 594	Dianova	1:1000
goat-anti-rabbit IgG	Alexa Fluor 594	Dianova	1:1000
goat-anti-rat IgG	Alexa Fluor 594	Dianova	1:1000

2.1.3 Antibiotics

Antibiotic	Working conc.	Selection	Source
Ampicillin	100 µg/ml	Bacteria	Sigma
Kanamycin	50 µg/ml	Bacteria	Sigma
Penicillin/streptomycin	1000 U/ml	Bacteria	Thermo
Blasticidin	7.5 µg/ml	Mammalian	Thermo

2.1.4 Cells

2.1.4.1 E.coli strains

Strain	Genotype	Source
TOP10	F– mcrA Δ(mrr-hsdRMS-mcrBC) Φ80lacZΔM15 ΔlacX74 recA1 araD139 Δ(ara eu) 7697 galU galK rpsL (StrR) endA1 nupG	Invitrogen
Stabl3	F-mcrB mrrhsdS20(rB-, mB-) recA13 supE44 ara-14 galK2 lacY1 proA2 rpsL20(StrR) xyl-5 λ-leumtl-1	Thermo

2.1.4.2 Eukaryotic cell lines

Name	Celltype	Source
HeLa	Human endocervical adenocarcinoma	M. L. Schmitz
HCT-116	Human colon carcinoma	M. L. Schmitz
HT-29	Human colon carcinoma	M. L. Schmitz
SW620	Human colon carcinoma	M. L. Schmitz
U20S	Human osteosarcoma	M. L. Schmitz

Name	Celltype	Source
OVCAR4	Human ovarian carcinoma	E. Strandmann
RPE-1	Immortalized human retinal epithelium	M. L. Schmitz
HCT-116	Human colorectal cancer	M. L. Schmitz
LN229	Human glioblastoma	M. L. Schmitz
MCF-7	Human breast cancer	M. L. Schmitz
HeLa	Human cervical carcinoma	M. L. Schmitz
HT-29	Human colorectal cancer	M. L. Schmitz
SW620	Human colorectal cancer	M. L. Schmitz
H1975	Human lung adonocarcinoma (NSCLC)	T. Stiewe
PC9	Human lung adonocarcinoma (NSCLC)	T. Stiewe
iFTSEC	Immortalized fallopian tube secretory epithelia cells (hTERT; shp53; CDK4^{R24C})	Abm(PMID: 21502498)
empty vector	iFTSEC transduced with pLenti CMV Blast empty (w263-1)	J. Dreute
KRAS^{G12V}/MYC	KRAS^{G12V}/MYC transduced iFTSEC	J. Dreute
KRAS^{G12V}/PI3K^{E545K}	KRAS^{G12V}/PI3K^{E545K} transduced iFTSEC	J. Dreute
KRAS^{G12V}/myrAkt1	KRAS^{G12V}/myrAkt1transduced iFTSEC	J. Dreute

2.1.5 Inhibitors

Name	Target	Working [C]	Source
(±)-3-Methyl-2-oxovalericacid	KGDHC	1 mM	Sigma
(R)-GNE-140	LDHA/B	7.5 µM	MedChemExpr
α-Cyano-4-hydroxycinnaminic acid	MCT1	1 mM	Sigma
Antimycin A	ETC, Complex III	1 µM	Agilent
AZD-3965	MCT1	5 µM	Selleckchem
BCH	LAT1	10 µM	Tocris
BMS-986205	IDO1	6 µM	MedChem
CB-839	Glutaminase	10 µM	Selleckchem
Cytochalasin B	GLUT	0.2 µM	Santa Cruz
Dichloracetate	PDK	1 mM	Sigma

Name	Target	Working [C]	Source
Eflornithin	ODC	60 µM	Tocris
Epacadostat	IDO1	40 µM	Hölzel Biotech
Etomoxir	CPT1	50 µM	Sigma
FCCP	mtMembrane	2 µM	Agilent
GSK-2839808A	LDHA/B	35 µM	Hölzel Biotech
H3B-120	CPS1	20 µM	Sigma
Indoximod	IDO-/TDO	2 µM	Selleckchem
Metformin	ETC complex I	10 mM	Invivogen
Oligomycin	ETC, Complex V	2 µM	Agilent
PFK15	PFKFB3	0.75 µM	Sigma
Rotenone	ETC, Complex I	1 µM	Agilent
TVB-2640	FASN	0.3 µM	Sigma
V-9302	ASCT2	3 µM	MedChemExpr

2.1.6 Chemicals

Name	Source
2-propanol (Isopropanol)	Roth
4-(2-Hydroxyethyl)-1-piperazineethansulfonic acid (HEPES)	Sigma
5-bromo-4-chloro-3-indoyl β-D-galactopyranoside (X-βGal)	Roth
Acrylamide	Roth
Ammonium persulfate (APS)	Sigma
Aprotinin	Sigma
Citric acid	Sigma
Dimethyl sulfoxide (DMSO)	Sigma
Ethanol	Sigma
Ethidium bromide	Sigma
EGTA	Sigma
Formaldehyde	Roth
Glucose	Sigma
Glutardialdehyde	Roth
Glycerin	Roth
Glycerol	Roth
Glycine	Roth

Name	**Source**
Hoechst 33342	Thermo
Hydrochloric acid	Sigma
Igepal CA-630	Sigma
Kynurenine	Santa Cruz
Lactate	Sigma
Leupeptin	Sigma
Magnesium chloride (MgCl2)	Sigma
Magnesiumchloride-hexahydrate ($MgCl_2$, $_6H_2O$)	Sigma
Methanol	Sigma
MitoSOX™	Thermo
mitoTempo	Santa Cruz
MitoTracker Deep Red	Thermo
Mowiol 4-88	Sigma
N-acetyl cysteine	Sigma
N,N,N’,N’-tetramethylethylendiamine (TEMED)	Roth
Nicotinamide adenine dinucleotide	Sigma
Nicotinamide riboside	Sigma
Nonidet P-40 (NP-40)	Roche
Phenylmethanesulfonylfluorid (PMSF)	Sigma
Potassium hydroxide (KOH)	Sigma
Potassium-hexaferrocyanide (II) Trihydrate ($K_4[Fe(CN)_6]3H_2O$)	ICN Biom.
Potassium-hexaferrocyanide (III) ($K_3[Fe(CN)_6]$)	Sigma
Propidiumiodide (PI)	Sigma
Sodium acide (NaN_3)	Sigma
Sodium chloride (NaCl)	Sigma
Sodium deoxycholate	Sigma
Sodium dodecyl sulfate (SDS)	Bio-Rad
Sodium fluoride (NaF)	Roth
Sodium hydrogen phosphate (Na_2HPO_4)	Roth
Sodium hydroxide (NaOH)	Roth
Sodium orthovanadate (Na_3VO_4)	Sigma
TMRE	Thermo

Name	**Source**
Tris(hydroxymethyl)aminomethane (Tris)	Roth
Triton X-100	Sigma
Trypan blue	Sigma
Tween-20	Gerbu
β-mercaptoethanol	Roth

2.1.7 Kits

Name	**Source**	**Cat no.**
BCA protein assay	Thermo	23225
GeneJET Plasmid Maxiprep	Thermo	K0491
GeneJET Plasmid Miniprep	Thermo	K0502
MinElute Gel Extraction	Qiagen	28604
MinElute PCR Purification	Qiagen	28004
NucleoSpin RNA isolation Kit	Macherey-Nagel	740955
PrimeScript RT Master Mix cDNA synthesis	Takara	RR036B
Seahorse XF Cell Mito Stress Test Kit	Agilent	103015

2.1.8 Enzymes

Name	**Source**
FastAP Thermo-sensitive Alkaline Phosphatase	Thermo
Phusion HF DNA polymerase	Thermo
rDNAse	Thermo
Restriction enzymes and buffers	Thermo
RNase A	Thermo
T4 DNA Ligase	Thermo
T4 Polynucleotide Kinase	Thermo
Taq DNA Polymerase	Thermo
Trypsin/0.05 % (v/v) EDTA	Thermo

2.1.9 Oligonucleotides

Name	**Sequence (5’ -> 3’)**	**Target**	**Purpose**
Blasti - for	TCGGAAATGAGAACAGGGGC	*BSD*	qPCR
Blasti - rev	GGGCAGCAATTCACGAATCC	*BSD*	qPCR

Name	**Sequence (5’ -> 3’)**	**Target**	**Purpose**
CXCL2_FW	AGCTTGTCTCAACCCCGCATC	*CXCL2*	qPCR
CXCL2_RV	GGGCAGGGCCTCCTTCAGG	*CXCL2*	qPCR
hCXCL1-f	AGGGAATTCACCCCAAGAAC	*CXCL1*	qPCR
hCXCL1-r	ACTATGGGGGATGCAGGATT	*CXCL1*	qPCR
hIcam1 qPCR for	AGCTTCGTGTCCTGTATGGC	*ICAM1*	qPCR
hIcam1 qPCR rev	TTTTCTGGCCACGTCCAGTT	*ICAM1*	qPCR
hIL1a fw	CATTGGCGTTTGAGTCAGCAA	*IL-1*	qPCR
hIL1a rev	CCTTCATGGAGTGGGCCATAG	*IL-1*	qPCR
hTNF qPCR FW	GGCGTGGAGCTGAGAGATAAC	*TNFα*	qPCR
hTNF qPCR RV	GGTGTGGGTGAGGAGCACAT	*TNFα*	qPCR
hTPI-for	GGACTCGGAGTAATCGCCTG	*TPI*	qPCR
hTPI-rev	TGTTGGGGTGTTGCAGTCTT	*TPI*	qPCR
huCcl2 qPCR for2	AGCAGCAAGTGTCCCAAAGA	*CCL2*	qPCR
huCcl2 qPCR rev2	TTGGGTTTGCTTGTCCAGGT	*CCL2*	qPCR
hVEGF-1α-For	CGCTATGTGACCTTTGGCATTT	*VEGFα*	qPCR
hVEGF-1α-Rev	GCTAAAGTCAGGGCCACTTACT	*VEGFα*	qPCR
IDO1 fw #3	TGCTTGGAGAAAGCCCTTCA	*IDO1*	qPCR
IDO1 rev #3	CGTCTGATAGCTGGGGGTTG	*IDO1*	qPCR
IL6_FW	AGACAGCCACTCACCTCTTCAG	*IL-6*	qPCR
IL6_RV	TTCTGCCAGTGCCTCTTTGCTG	*IL-6*	qPCR
KRAS - for	CGAGGGATTTCTGTGCGTGT	*KRAS*	qPCR
KRAS - rev	GAGATGGCAGGTCGCACTTA	*KRAS*	qPCR
LDH-A F	TTGACCTACGTGGCTTGGAAG	*LDHA*	qPCR
LDH-A R	GGTAACGGAATCGGGCTGAAT	*LDHA*	qPCR
LDHB fw	GCCTTCTCTCTCCTGTGCAA	*LDHB*	qPCR
LDHB rev	AGAGCAAGTTCATCAGCCAGA	*LDHB*	qPCR
MMP9-Fw 2	GAGACCGGTGAGCTGGATAG	*MMP9*	qPCR
MMP9-Rv 2	CGGCAAGTCTTCCGAGTAGT	*MMP9*	qPCR
MYC - for	CAGGAAAGACTACCCCGCTG	*c-Myc*	qPCR
MYC - rev	GAATCTGGTCTCTCAGGGCG	*c-Myc*	qPCR
VEGFC-qRT for	CACGAGCTACCTCAGCAAGA	*VEGFc*	qPCR
VEGFC-qRT rev	GCTGCCTGACACTGTGGTA	*VEGFc*	qPCR

2.1.10 siRNAs

Name	Sequence (5’ -> 3’)	Target
siIDO1-C	CGUAAGGUCUUGCCAAGAAAUAUTG	*IDO1*
siLDHA-A	CUCCUGAAGUUAGAAAUAAGAAUGG	*LDHA*
siLDHB-A	UUAUGAUGCAAUCAGGACUGUACUUGA	*LDHB*

2.1.11 Plasmids

Construct	Source
pCMV-VSV-G	Addgene
pMDLg pRRE	Addgene
pRSV-Rev	Addgene
pLenti CMV Blast empty	Addgene
pLenti-P2A-BSD	J. Dreute
pLenti-V5_KRAS4BV12-P2A-myr_Akt1_HA-BSD	J. Dreute
pLenti-V5_KRAS4BV12-P2A-PI3KE545K_HA-BSD	J. Dreute
pLenti-V5_KRAS4BV12-P2A-cMyc_HA-BSD	J. Dreute

2.1.12 Other reagents and materials

Name	Source
ABsolute qPCR SYBR green ROX Mix	Thermo
Agar	Applichem
Agarose	PeqLab
Bovine serum albumin (BSA)	Sigma
Cell culture consumables	Sarstedt
CellTrace™ Oregon Green™ 488	Invitrogen
Coverslips (round, 18 mm)	Sarstedt
Deoxynucleoside triphosphates (dNTPs)	Thermo
DMEM, GlutaMAX	Thermo
DMEM/F-12, high glucose + GlutaMAX	Thermo
DMEM/F-12, no glucose-glutamine-phenol red	Thermo
FACSFlow	BD Bioscience

Name	Source
FACSRinse	BD Bioscience
Fetal calf serum (FCS)	Thermo
GeneRuler 100bp & 1kb DNA ladders	Thermo
HTS Transwell®-96 Permeable Support with 8.0 µm Pore	Corning
Ibidi micorslides	Ibidi
Lipofectamine	Thermo
Noble agar	AppliChem
Nutragen® Type I Collagen Solution	Adv. Biomatrix
Polybrene	Sigma
Polyethyleenimine, linear (PEI)	PolyScience
RPMI1640, GlutaMAX	Thermo
Skimmed milk powder	Sigma
Western Lightning ECL solution	Perkin Elmer

2.2 Methods of molecular biology

2.2.1 Transformation of bacterial strains

Lysogeny broth (LB) medium:	1 % (w/v) tryptone; 0.5 % (w/v) yeast extract; 1 % (w/v) NaCl
Lysogeny broth (LB) agar:	LB medium with 1.5 % (w/v) agar with respective antibiotics

Complete ligation or 100 ng of Plasmid DNA were used for bacterial transformation. DNA was pipetted into 100 µl of Bacterial solution and incubated for 30 min on ice. Then, bacteria were heat shocked for 1 minutes at 42°C and subsequently chilled for 5 minutes on ice. Bacteria were supplemented with 500 µl of LB medium, and after incubation at 37°C for 1 hour while shaking, bacteria were streaked onto agar plates containing the appropriate selection antibiotics.

2.2.2 Isolation of plasmid DNA

For isolation of plasmid DNA, GeneJET Plasmid-Maxiprep-Kit (cat. no. K0491) was used. Isolation was performed according to manufacturer's instructions. Briefly, bacteria were pelleted, resuspension solution was added and then mixed with lysis solution for 3 minutes. After addition of neutralization solution and endotoxin binding reagent, debris was pelleted at 48,000 x g for 20 minutes. DNA was precipitated using 96% EtOH and loaded onto a spin column. After multiple washing steps, DNA was eluted in 300 µl ddH_2O.

2.2.3 Measurement of DNA concentration

DNA concentration was determined by measuring the optical density at a wavelength of 260 nm (OD260). The photometer uses the following formulas to determine the quantity and quality of the sample:

DNA-concentration:	1 OD260 nm = 50 µg/ml dsDNA
DNA-purity:	OD260 nm/OD280 nm ≈ 1.8

2.2.4 Restriction digest of DNA

For two DNA fragments to be joined together, they must be cut from their plasmids with the same restriction enzymes to allow complementary base pairing. Most restriction enzymes are operating at 37°C and cut a 6-8 bp long, highly specific restriction site in the DNA. For a double digest, the buffers recommended by ThermoFisher were used. The following components were used for each restriction digest:

Reaction mix	Volumes
DNA (5 µg)	X
10x Restriction-buffer	1.5 µl
Restriction enzyme (10 U/µl)	1 µl
H_2O	fill until 15 µl

Restriction digest of DNA samples were incubated for 2-3 hours followed by agarose gel electrophoresis. To counteract re-ligation, vector DNA was dephosphorylated by adding 1 µl of alkaline phosphatase to the reaction mix.

2.2.5 Ligation of DNA fragments

In order to join two fragments of DNA, we performed enzymatic ligation. The vector and insert DNA were mixed in a ratio of 1:1 and 1:3 (vector:insert). Sticky-end ligations were performed for 30 minutes at RT, whereas blunt-end ligations were incubated for approximately 16 hours at steadily decreasing temperature using a thermal beaker in a 4°C cold room.

Reaction mix	Volumes or mass
Vector-DNA	100 ng
Insert-DNA	1:1 and 1:3
10x T4-Ligase buffer	1 µl
T4-Ligase	1 µl
ddH_2O	fill until 10 µl

2.2.6 Polymerase chain reaction (PCR)

Polymerase chain reaction was performed to generate DNA fragments for cloning. The following reaction mixtures and cycling protocols were used:

Reaction mix	**Volumes or concentration**
Plasmid-DNA	10-200 ng
5x HF/GC-Buffer	6 µl
Phusion-Polymerase	1:1 and 1:3
Forward-Primer	10 µM
Reverse-Primer	10 µM
dNTP	10 mM
ddH$_2$O	fill until 30 µl

Following PCR cycling protocol was used:

Step	**Temperature**	**Time**	**Cycles**
Initial denaturation	98°C	5 minutes	
Denaturation	98°C	30 seconds	x40
Annealing	55-72°C	30 seconds	
Elongation	72°C	30 seconds	
Final elongation	72°C	5 minutes	

For overhang PCR reactions, following cycling protocol was used:

Step	**Temperature**	**Time**	**Cycles**
Initial denaturation	98°C	2 minutes	
Denaturation	98°C	45 seconds	x15
Annealing	55-72°C	45 seconds	
Elongation	72°C	30 seconds	
Denaturation	98°C	45 seconds	x40
Annealing	55-72°C	45 seconds	
Elongation	72°C	30 seconds	
Final elongation	72°C	7 minutes	

2.2.7 Agarose gel electrophoresis

50x TAE buffer: 4 mM Tris (pH 8.3); 50 mM acetic acid; 1 mM EDTA

The number and size of DNA fragments derived from a PCR reaction or restriction digest was analyzed by agarose gel electrophoresis. Gels were cast using 1x TAE buffer (4 mM Tris pH 8.3, 50 mM acetic acid, 1 mM EDTA) and 0.2 µg/ml ethidium bromide. Samples were loaded onto the gel with 6x loading buffer and separated using 100-130 V. DNA was visualized using an UV transilluminator at 365/312 nm.

2.2.8 RNA isolation

Cells were washed 2 times with ice-cold PBS and harvested into 1.5 ml tubes. Extraction of total RNA was performed using the NucleoSpin® kit (Macherey-Nagel, cat. no. 740955). Cells were resuspended in RA1 lysis buffer containing ß-mercaptoethanol and loaded onto NucleoSpin® filter tubes. The flowthrough was mixed 1:1 with 70% EtOH and loaded onto NucleoSpin®RNA columns. RNA bound to the column was then desalted with MDB buffer following digestion with rDNAse for 15 min. rDNAse was inactivated with RAW2 buffer and washed twice with RA3 buffer. The RNA was then eluted in 30-50 µl RNase-free H_2O. RNA concentration was determined by measuring optical density at 260 nm (OD260) on an Eppendorf photometer using a microliter cuvette.

2.2.9 Synthesis of complementary DNA (cDNA)

PrimeScript RT Reagent Kit (Takara, cat. no. RR037B) was used. The following reagents were combined:

Reaction mix	Volumes
RNA (0.5 µg)	X
5x cDNA-MasterMix	2 µl
H_2O	X
Total	10 µl

The sample was incubated for 15 min at 37°C followed by 5 minutes of inactivation at 85°C. For use in qPCR experiments, cDNA samples were diluted 1:10 in ddH_2O.

2.2.10 Quantitative PCR (qPCR)

Relative expression of genes was analyzed by qPCR. PCR reactions were performed on a StepOnePlus Real-Time PCR System (Applied Biosystems) using 96-well PCR plates (Sarstedt). Each 10 µl PCR reaction consisted of 10 ng cDNA, 1× SYBR Green ROX Master Mix, and 0.2 µM per reverse and forward primer. All reactions were run as technical duplicates. Melting curve analysis was performed for each primer pair to confirm the specificity of the reactions. The following cycling protocol was used:

Step	Temperature	Time	Cycles
Initial denaturation	98°C	5 minutes	
Denaturation	98°C	30 seconds	x40
Annealing	60°C	30 seconds	
Elongation	72°C	30 seconds	
Final elongation	72°C	5 minutes	
Melting curve	70-95°C		

Results were analyzed using the $\Delta\Delta C_T$-method (Livak and Schmittgen, 2001).

2.3 Methods of cellular biology

2.3.1 Eukaryotic cell culture

DMEM-F12 complete:	DMEM-F12 with 17.5 mM Glucose; 10 % (v/v) FCS; 2.5 mM L-Glutamine; 1 % (v/v) Penicillin/Streptomycin
PBS:	137 mM NaCl; 1.5 mM KH_2PO_4; 2.7 mM KCl; 8.0 mM Na_2HPO_4, pH 7.4

Eukaryotic cells were always incubated at 37°C and an atmospheric CO_2 concentration of 5%. Cells were passaged in fresh medium twice a week. For passaging, cells were washed with PBS and then trypsinized and split. For experiments, cells were automatically counted using LUNA-II^{TM} cell counting device which is based dye-exclusion to analyze the ratio between live and dead cells.

2.3.2 Freezing and thawing of eukaryotic cell lines

Freezing medium: 10 % (v/v) DMSO in FCS

For freezing eukaryotic cells, pelleted cells are resuspended in freezing medium, transferred to cryotubes and frozen at -150°C. For thawing, cells were reconstituted in a 37°C water bath and then mixed with DMEM-F12-complete and seeded into cell culture flasks.

2.3.3 Transfection of mammalian cells

Blank medium (-/-):	DMEM-F12
Transfection medium (-/+):	DMEM-F12; no penicillin/streptomycin; 10 % (v/v) FCS

Constituents	6 cm dish	10 cm dish
DNA	0.5-2.5 µg	1-5 µg
DNA-Mix (-/- Medium)	100 µl	200 µl
PEI-Mix (-/- Medium)	100 µl	200 µl
Transfection-Medium (-/+ Medium)	2 ml	4 ml

Introduction of plasmid DNA into mammalian cells was facilitated with the use of polyethylenimine (PEI). Briefly, DNA and PEI were individually mixed with -/- medium, vortexted and incubated for 5 min at RT. Subsequently, DNA and PEI solutions were mixed, vortexed and incubated for 20 min at RT. Cell medium was exchanged to transfection medium and DNA/PEI complexes were added dropwise to the cells. After 4 h of incubation, medium was exchanged to complete medium.

2.3.4 siRNA-mediated gene silencing

Expression of specific target genes was knocked down using small interfering RNAs (siRNA). Eukaryotic cells were transfected using Lipofectamine (ThermoFisher®) according to the manufacturer's instructions. For all experiments of this study, 5-10 nM of siRNA was used. To enhance gene silencing, cells were re-transfected with siRNA two days later.

2.3.5 Preparation of whole cell protein extracts

RIPA-lysis buffer: 20 mM Tris/HCl, pH 7.5; 150 mM NaCl; 1 % (v/v) NP-40
Freshly added: 10 mM NaF; 0.5 mM Na_3VO_4; 1 mM PMSF; 10 µg/ml Aprotinin; 10 µg/ml Leupeptin

Whole cell lysates were prepared by lysing the cells in a RIPA lysis buffer. For this purpose, cells were first washed 2 times with cold PBS, scraped and collected in a tube. After centrifugation (2000 × g, 2 min), the cell pellet was resuspended in 150 µl lysis buffer and incubated on ice for 20 min. The lysates were cleared by centrifugation (16 100 × g, 15 min, 4 °C) and subsequently subjected to sonication. For western-blot experiments, protein concentration of cell lysates was quantified using Pierce™ BCA Protein Assay Kit according to manufacturer’s instructions.

2.3.6 Lentiviral production

Lentiviral particles were generated using the 3rd generation lentiviral packaging system:

Plasmids	µg
pMDL g/p RRE	10
pRSV-rev	5
pHCMV-VSV-G	2
Transfer construct	10

Per construct, approximately 2x10^6 HEK293T cells were seeded in a 10 cm petri-dish and incubated for 24 hours. After 24 hours, plasmids (see table X.) were mixed with 2.5 µl linear PEI per µg of plasmid DNA in 1.5 ml cell culture medium w/o FCS or antibiotics. After 15 minutes of incubation, PEI/DNA mixture was added to HEK293T cells where complete medium was previously exchanged to medium with FCS but w/o antibiotics. After 4 hours of incubation in a cell culture incubator, medium was exchanged to complete media and incubated for further 24 hours for viral production. Viral particles were then harvested and centrifuged at 400 x g for 5 minutes, followed by sterile filtration with 0.45 µm. Filtrated supernatant was mixed with 6 µg/ml polybrene and used as a 1:5 dilution with complete medium for transduction of target cells. After transduction of 16 hours, medium was replaced by complete medium.

2.3.7 Cellular model system

For the establishment of the cellular model of this work, comprised of a noncancerous cell line and a cancer cell line, immortalized human fallopian tube secretory cells (iFTSEC, FT240) were used. FT240 (cat. #T0762) were purchased from abm®. After lentiviral of plasmid constructs, cells were phenotypically monitored for the next three months. After three months, cells were tested for cancerous transformation.

2.3.8 Characterization of cancerous transformation

2.3.8.1 Proliferation assay

Of each cell line, $0.5x10^5$ cells were seeded in a 6-well plate and counted every 2 days for the following 12 days.

2.3.8.2 Scratch assay

Of each cell line, $0.8x10^5$ cells were seeded in a 6-well plate. 16 hours prior to scratching, complete cell medium was exchanged to 1%FCS containing medium to reduce cell proliferation. A yellow tip was used to perform a vertical scratch. Medium was exchanged to remove floating cells and images of the same spot per individual well were acquired for the next 24 hours. Scratch area quantification was performed using "Woud_healing_size_tool-3" in FIJI (Suarez-Arnedo *et al.*, 2020).

2.3.8.3 Transwell-invasion assay

Approx. 0.1-0.2 $x10^6$ cells were seeded into 6-well plates and cultured overnight. Culture medium was exchanged to serum-free medium and cells were starved for 24 hours. After trypsinization cells were pelleted and resuspended in 1 ml serum-free medium containing CellTrace™ Oregon Green™ 488 (5 µM) and incubated for 30 minutes at 37°C. Meanwhile, 15 µl of type I Collagen Solution, bovine, 6 mg/ml were added onto the transwell-membrane, followed by 45 minutes of incubation at 37°C. Subsequently, coated surfaces were rinsed with PBS. After 30 minutes of staining, cells were washed twice with 1x PBS. Then, 50 µl containing 3000 cells was added into the upper compartment of the transwell chamber. The lower compartment was filled with 250 µl/well of serum-free media. Cell migration (-collagen) and invasion (+ collagen) was allowed for 24 hours at 37°C. After 24 hours, medium from upper and lower compartment was aspirated and the upper compartment was cleaned with a cotton swab to remove non-migrated/-invaded cells. Both chambers were rinsed once with 100 µl 1x PBS. The upper and lower compartments were then filled with 50 µl and 250 µl PBS, respectively. Images of the GFP+ migrated or invaded cells were obtained using a *Leica LAS X THUNDER* microscope.

2.3.8.4 Soft-agar colony formation assay

The soft-agar colony formation assay was carried out using 6-well plates. The agar was prepared with 2x complete medium (2xFCS; 2xL-Glutamine). 2 ml of 0.6% bottom “feeder-layer” was poured into the well and hardened for 15 min at 4°C. Subsequently, 1 ml of 0.3% “cell-layer” containing 2 x 10^4 cells was pipetted onto the bottom-layer. 500 µL of growth-medium was replenished 2 times a week. Colony growth was closely monitored and the experiment was quantified after approx. 14 days. Colonies were stained with 0.01% Crystal-Violet, 10% EtOH in ddH_2O. Quantification of colonies was performed using FIJI. The threshold for colony area was set to 0.02 mm^2 in order to only quantify colonies who are bigger than 0.02 mm^2.

2.3.9 Immunofluorescence

Immunofluorescence experiments were performed using 18 mm cover slips in 6-well plates. Cells were seeded at 50-70% confluency. Fixation was performed using 4% Formaldehyde, blocked with 3% BSA-0.3% Triton-X-100 in PBS for 30 min. 1 µL of primary antibody was diluted in 0.3% BSA-0.3% Triton-X-100 in PBS and incubated at 4°C overnight in a humidity chamber. 1 µL of secondary antibody was diluted in 0.3% BSA-0.3% Triton-X-100 in PBS and incubated at RT for 2 hours in dark. Secondary antibody solution was replaced with Hoechst33342 staining solution (1:10.000) in PBS for 10 minutes at RT. After this step, cover slips are ready for mounting and imaging. After each step until Hoechst33342 addition, cells were washed twice with 0.3%-Triton-X-100-PBS. Prior to adding Hochst33342, cells were washed with PBS.

2.3.10 Crystal violet cell-viability assay

Staining solution:	25% Methanol, 0.5% Crystal-violet in ddH_2O
De-staining solution:	2% SDS in ddH_2O

Cells were washed twice with ice-cold PBS, placed on ice and fixed with ice-cold 100% Methanol for 10 minutes. After fixation, methanol was aspirated and cells were dried for 10 minutes at RT. Cells were incubated with staining solution for 10 minutes. Excess staining solution was poured off and cells were washed three times with H_2O. Cells were then dried at 37°C in an incubator and subsequently de-stained for 30 - 60 minutes. Absorbance was measured at 600 nm using a GloMax plate reader.

2.3.11 ß-galactosidase activity assay

Fixation solution:	2% (v/v) formaldehyde; 0.2 % (v/v) glutaraldehyde in PBS
X-gal staining solution:	20 mM citric acid; 40 mM sodium hydrogen sulfate; 150 mM NaCl; 5 mM potassium ferrocyanide trihydrate; 5 mM Potassium ferricyanide; 2 mM $MgCl_2$; 1 mg/ml X-gal

Cells were washed with PBS and the fixation solution was applied for 5 minutes. Fixation solution was removed and cells were washed twice with PBS. Then, cell plate/dish was sealed using parafilm and incubated with X-gal staining solution at 37°C for 16 hours in a non-CO_2 incubator. The staining solution was removed by washing twice with PBS and once with 100% Methanol at RT. Images were taken after several hours of drying at RT in dark.

2.3.12 Analysis of cell cycle distribution

PI staining solution:	20 µg/ml propidium iodide; 200 µg RNase A; 0.1 % (v/v) Triton-X-100 in PBS

Cell cycle distribution was analyzed with a FACSCalibur (BD Biosciences) flow cytometer using propidium iodide (PI). Cells were harvested by trypsinization. Subsequently, cells were washed twice with PBS (300 x g; 4°C; 2 minutes), and the pellet was resuspended in 300 µl PBS. 1 ml of 70% (v/v) ethanol was added dropwise while vortexing to avoid formation of cell clumps. Cells were incubated at 4°C for 1 hour at -20°C. Cells were then washed twice with PBS (300 x g; 4°C; 2 minutes) and resuspended in 500 µl PI staining solution and incubation at 37°C for 15 minutes in a waterbath. Samples were placed on ice to stop the reaction. The

FL-2-A channel was used for detection the PI signal. Data were analyzed using BD CellQuest Pro software.

2.3.13 Molecular probes for staining mitochondria and reactive oxygen species

For molecular probe experiments, cells were seeded at 50% confluence in a 10 cm dish. One day post seeding, cells received (R)-GNE-140 (7.5 µM) and BMS-986205 (6 µM) for 48 hours. Then, cells were trypsinized and loaded with molecular probes at 37°C in the dark according to the following table:

Probe	Concentration	Loading time
MitoSox Red	5 µM	10 minutes
Mitotracker Deep Red FM	200 nM	15 minutes
TMRE	200 nM	20 minutes

After loading, cells were washed once with PBS and subjected to flow-cytometric analysis.

2.3.14 Seahorse metabolic flux analysis

XF base medium:	DMEM, no glucose/glutamine/pyruvate/phenol red, pH 7.4
XF complete medium:	DMEM, 17.5 mM Glucose, 2.5 mM Glutamine, 0.5 mM pyruvate
XF calibrant solution:	not specified
DMEM/F-12 complete:	DMEM/F-12, GultaMAX + 10 % (v/v) FCS + 1 % (v/v) Penicillin/Streptomycin

For metabolic flux analysis, Seahorse XF Cell Mito Stress Test Kit (Agilent, cat. no. 103015-100) was used. 2500 $KRAS^{G12V}$/MYC cells and 3500 empty vector cells were seeded in 100 µl DMEM/F-12 complete medium in 96XF cell culture plates. Cells were allowed to settle at RT for 1 hour and incubated overnight at 37°C in a humidified atmosphere, containing 5 % CO_2. XF Cartridges were hydrated with 200 µl of distilled H_2O overnight. XF calibrant was prepared by incubation in a 37°C non-humidified, non-CO_2 incubator overnight. The next day, cells were stimulated with (R)-GNE-140 (7.5 µM) and/or BMS-986205 (6 µM) for 3 hours. Then, medium was replaced by 180 µl XF complete medium containing the indicated concentrations of (R)-GNE-140 and/or BMS-986205 and placed in a 37°C non-humidified incubator for 1 hour. Total drug incubation time at the start of Seahorse analysis was therefore 4 hours. Meanwhile, drugs were prepared and injection ports were loaded:

Drugs	Stock concentration	Loading volume	Final concentration
Oligomycin	100 µM	20 µl – Port A	2 µM
FCCP	100 µM	22 µl – Port B	2 µM
AntA/Rot	50 µM	25 µl – Port C	0.5 µM

Next, the cartridge was calibrated using 200 µl of XF calibrant per well and the Seahorse calibration run was started. After the cells experienced a total of 4 hours of (R)-GNE-140 and/or BMS-986205 treatment, the calibrated cartridge was placed onto the 96XF cell culture plate. Seahorse measurements were obtained by using the recommended Seahorse XF Cell Mito Stress Test analysis run. For in-well normalization of cell-numbers, a second plate of cells was seeded and treated exactly the same way as the cells that were subjected to Seahorse analysis, with the exception that this normalization plate did not receive the Mito Stress Test drugs (Oligomycin, FCCP, AntA/Rot). During the Seahorse analysis run, the normalization plate was subjected to crystal-violet cell viability quantification.

2.3.15 Treatment of empty vector and KRAS^{G12V}/MYC cells with (R)-GNE-140 and BMS-986205

Empty vector and KRAS^{G12V}/MYC cells received 7.5 µM (R)-GNE-140 and 6 µM BMS-986205 in all experiments. Due to the increased proliferation rate of KRAS^{G12V}/MYC cells, empty vector cells were generally seeded at ~40% higher confluency (day 0). This allows treatment of equally confluent culture dishes on the day of stimulation (day 1). In experiments where cells were incubated for 4 days or longer, cells receiving mono-treatment with DMSO, (R)-GNE-140, or BMS-986205 were seeded at 1:10 ratio compared to the (R)-GNE-140 and BMS-986205 combination treatment. This experimental adjustment could not be avoided, as cells which did not receive the combination treatment would die due to overgrowth and/or acidification of the medium after prolonged cell culture.

2.3.16 Experimental parameters for cell lines tested in this study

	Cells seeded per			Concentration (µM)	
Cell lines	well of a 96-WP	well of a 6-WP	10 cm dish	(R)-GNE-140	BMS-986205
U20S	3000	54.000	400.000	30	10
OVCAR4	1500	60.000	500.000	7.5	6
RPE-1	1000	19.000	300.000	8	15
HCT-116	3000	54.000	400.000	20	8
MCF-7	3000	54.000	400.000	15	6
HeLa	1500	27.000	200.000	15	10
HT-29	4500	81.000	500.000	20	6
SW620	4500	81.000	500.000	10	6
H1975	4500			30	2.5
PC9	4500			15	8
LN229	4500			20	20

If cells were treated for 96 hours total, seeding cell numbers for DMSO/control and mono treatments were adjusted to 1/3 of the above depicted seeding cell numbers, due to cellular overgrowth. Treatment times are experiment specific and can be found in the respective figure legends.

2.4 Biochemical methods

2.4.1 SDS polyacrylamide gel electrophoresis

10 x SDS running buffer:	250 mM Tris; 2 M glycine; 1 % (w/v) SDS
4 x lower buffer:	1.5 M Tris/HCl, pH 8.8; 0.4 % (w/v) SDS
4 x upper buffer:	0.5 M Tris/HCl, pH 6.8; 0.4 % (w/v) SDS

Sodium dodecyl sulfate-polyacrylamide gel electrophoresis (SDS-PAGE) was used to separate proteins according to their molecular weight on a discontinuous gel following standard laboratory procedures. Samples were boiled for 5 min at 95°C prior to SDS-PAGE loading and electrophoresis was performed at constant 85 V for 2:30 hours in SDS running buffer.

2.4.2 Western blotting

Transfer-Buffer:	50 mM Tris; 40 mM Glycine; 20 % (v/v) Methanol; 0.04 % (w/v) SDS
TBS-T:	25 mM Tris (pH 7.4); 137 mM NaCl; 5 mM KCl; 0.7 mM CaCl2; 0.1 mM MgCl2; 0.1 % (v/v) Tween 20
Block-Buffer:	5 % (w/v) nonfat dry milk or BSA in 1xTBS-T
1. Antibody solution:	1 % (w/v) nonfat dry milk or BSA in 1xTBS-T; 0.05 % (v/v) NaN_3
2. Antibody solution:	1 % (w/v) nonfat dry milk or BSA in 1xTBS-T

Directly after SDS-PAGE, Western blotting was performed. For immunodetection, proteins were transferred from SDS gels to polyvinylidene fluoride (PVDF) membranes in a semi-dry blotting device. Electrophoretic transfer was conducted at 24 V for 2:30 hours. Membranes were then incubated in blocking buffer at room temperature for 1 hour while shaking. After 1 hour of blocking, the membranes were incubated with the primary antibody solution at 4 °C for 16 hours. Membranes were washed 4 times for 5 minutes in TBS-T at room temperature and incubated with the secondary antibody solution for 2 hours at RT. After washing 4 times for 5 minutes in TBS-T at RT, proteins were detected on a ChemiDoc Touch Imaging System (Bio-Rad) with enhanced chemiluminescence (ECL).

2.4.3 Transmission electron microscopy

Fixative solution: 1.5 % glutaraldehyde; 2 % formaldehyde; 0.15 M HEPES/KOH (pH 7.4)

$0.5x10^6$ cells were seeded in 10 cm dishes and incubated for 24 hours. Then, respective treatments were performed for 48 hours. Cells were washed twice with PBS, collected by scraping and pelleted for 3 minutes at 800 x g, followed by aspiration of the supernatant. Cell pellet were then resuspended in fixative solution and stored at 4°C. Specimen preparation was performed by Tamara Papadakis (Institute for Anatomy and Cell Biology at the Justus Liebig University Giessen). Briefly, cells were fixed with 1% osmium tetroxide and subjected to contrasting using half saturated uranyl-acetate-solution overnight. Then, cells were dehydrated using a titration of 30 – 100 % EtOH and embedded in Epon overnight. Following degasification, cells were dried in fresh Epon at 60°C for 48 hours. Ultrathin slices were cut using (UltraCuzt S, Leica) and examined in a (EM Zeiss 902). Images and image analysis was performed in cooperation with Dr. Ulrich Gärtner (Institute for Anatomy and Cell Biology at the Justus Liebig University Giessen).

2.4.4 Metabolomics

Starting with the metabolite extraction, the targeted metabolic profiling was performed by Dr. Stephan Klatt and his team from the University Hospital Frankfurt/Goethe University, Institute for Vascular Signaling.

Methanol Extraction buffer: 1 mM TCEP, 1mM ascorbic acid, 0.1% formic acid in 85:15 Methanol:H_2O containing the internal standards of Homotaurine and Serotonin-d4, both at a final concentration of 0.001 mM

Boric acid buffer: 200 mM boric acid in MilliQ water

AQC reagent:	6-aminoquinolyl-N-hydroxysuccinimidyl carbamate (AQC) is a chemical reagent. It is stored as powder at - 80 °C and solubilized in 100% acetonitrile once needed. At 55 °C, it reacts with amine groups to form a stable derivative. Each formed amine-derivative is later quantified in the mass spectrometer.

2.4.4.1 Sample preparation

1x10^6 cells were seeded in 10 cm dishes and incubated for 24 hours. Then, respective treatments were performed for 4 hours. Cells were washed twice with PBS, collected by scraping and pelleted for 3 minutes at 800 x g, followed by aspiration of the supernatant and snap freezing in liquid nitrogen.

2.4.4.2 Amine extraction

Metabolites were extracted by adding methanol extraction buffer at a volume to cell pellet weight ratio of 10:1. The mixture was shortly vortexed, followed by 4 rounds of sonication (in an ice bath, 30 seconds for each round) and vortexing. Next, samples were incubated for 10 minutes on ice, followed by short vortexing. To remove the protein fraction, samples were centrifuged at 14000 rpm for 10 minutes at 4°C. Supernatants were transferred to a new tube and diluted with 2x volume of MilliQ water and frozen at -80°C. After freezing, the samples were freeze-dried overnight. Dried samples were reconstituted in 80 µl boric acid buffer followed by addition of 4 µl of 1N NaOH and 20 µl AQC reagent. Samples were vortexed shortly, incubated on ice for 1 minute and shortly centrifuged at 5000 rpm. Amine derivatization was allowed in a Thermocycler for 10 min at 55°C. The reaction was stopped by placing the samples back on ice and subsequent centrifugation at 14000 rpm for 10 minutes at 4°C. Next, supernatants were carefully transferred to MS glass vials and 5 µl per sample were injected into the mass spectrometer. Blank samples, quality controls and standard curve samples were injected.

2.4.4.3 Central carbon metabolites, nucleotide and nucleoside extraction

Metabolites were extracted by addition of 100 µl Trifluorethanol:H_2O (1:1) and 10 minute incubation, followed by addition of 200 µl MeOH:EtOH (1:1) for 10 minutes. After addition of H_2O and incubation for 10 minutes, the samples were loaded onto Captiva EMR-Lipid Plates and pushed through. Captiva plates were washed with 200 µl H_2O:MeOH:EtOH (2:1:1) containing the internal standards citrate-1,5,13C2 and succinate-1,4-13C2. The combined filtrate was dried under nitrogen flow until solvents evaporated and subsequently shock frozen with liquid nitrogen and freeze-dried overnight. Dried samples were reconstituted with 37,5 µl AcN and sonicated on ice for 45 seconds, followed by addition of 12,5 µl H_2O and sonication for 45 seconds on ice. Samples were centrifuged at 14000 rpm for 10 minutes at 4°C and the supernatants were transferred to MS glass vials where 4 µl were injected into the mass spectrometer. Blank samples, quality controls and standard curve samples were injected.

2.4.4.4 Mass spectrometry

Mass spectrometer: Agilent Technologies 6495C QQQ

HPLC: 1290 Infinity II BIO	**Amines**	**Central carbon, Nucleosides & nucleotides**
HPLC column	Zorbax Extend C18 RRHD (2.1x150mm, 1.8µ), Agilent Technologies	InfinityLab Poroshell 120 HLIC-Z (RRHD 2.1x150mm, 2.7-Micron) PEEK Lined, Agilent
Solvent A	0.1% formic acid in water	20 mM Ammonium acetate, 5 µM Medronic Acid in water
Solvent B	0.1% formic acid in Acetonitrile	Acetonitrile

2.4.4.5 HPLC-Gradient

Polarity: Positive Mode

Mode: AJS ESI, Dynamic MRM

Amines		**Central carbon metabolites, Nucleosides & Nucleotides**	
Time (min)	**Solvent B**	**Time (min)**	**Solvent B**
0	1%	0	85%
2	1%	1	85%
9	15%	8	75%
14	30%	12	60%
16	60%	15	10%
17	60%	18	10%
18	1%	19	85%
Flow: 0.3 ml/min		19.10	85%
		22	85%
		22.1	85%
		23	85%
		Flow: 0.4 ml/min	

2.4.4.6 Mass spectrometry parameters

	Amines	**Central carbon metabolites, Nucleosides & Nucleotides**
Gas Temp	290°C	200°C
Gas Flow	20L/min	14L/min
Nebulizer	45 psi	40 psi
Sheath Gas Temp	400°C	375°C
Sheath Gas Flow	11L/min	12L/min
Capillary Voltage	3800V (Pos) and 3800V (Neg)	4000V (Pos) and 2500V (Neg)
Nozzle Voltage	500V (Pos) and 1500V (Neg)	500V (Pos) and 0V (Neg)
High Pressure RF	140V (Pos) and 90V (Neg)	150V (Pos) and 90V (Neg)
Low Pressure RF	60V (Pos and Neg)	60V (Pos and Neg)

Metabolite peaks were annotated with the software Skyline-daily (version 22.2.1.278) and concentrations were calculated using GraphPadPrism9.

2.5 Synergy calculation

Synergy calculation was performed using the synergy score and coefficient of drug interaction (CDI) (Chen *et al.*, 2014).

Example:

Drug A achieves reduction of cell viability to 0.9 as compared to the control.
Drug B achieves reduction of cell viability to 0.7 as compared to the control.
Drug AB (combination treatment) achieves reduction of cell viability to 0.3 as compared to the control.

2.5.1 Synergy score

The synergy score describes the %-point decrease of cell-viability achieved of a drug combination, when compared to the calculated additive effect.

Additive effect: Drug A * Drug B; 0.9 * 0.7 = 0.63
Therefore, the calculated additive effect of the drug combination AB is a reduction of cell viability to 0.63.

Synergistic effect: Additive effect – Drug AB; 0.63 – 0.3 = 0.33
Therefore, the effect of the combination treatment is 0.33 or 33 %-points higher as the calculated additive effect. Or the combination treatment achieves 33% synergy.

2.5.2 Coefficient of drug interaction (CDI)

The CDI describes the synergistic effect of a drug combination compared to the calculated additive effect and differentiates between significant synergy and non-significant synergy.
Formula: Drug AB/(Drug A * Drug B); 0.33/(0.9*0.7) = ~0.52
> 0.7, non-significant synergy
≦ 0.7, significant synergy
The smaller the number, the higher the synergy.

3 Results

3.1 The cancer research model: Healthy vs Cancer

3.1.1 Generation of HGSOC-like model system

As this study focuses on high-grade serous ovarian cancer (HGSOC), immortalized fallopian tube secretory epithelial cells (iFTSEC), which is generally accepted as the origin of HGSOC (Labidi-Galy *et al.*, 2017b), were used. This cell line was derived from the fallopian tubes of a 55-year old female who had undergone prophylactic bilateral oophorectomy (Karst, Levanon and Drapkin, 2011). These isolated tumor cells were immortalized via introduction of human telomerase (hTERT) a dominant-negative mutant CDK4^{R24C} and an shRNA against *TP53* (Karst and Drapkin, 2012).

These immortalized iFTSECs were used as a starting point for the generation of an oncogenic transformed cell line. As Myc, Akt1, PI3K and KRAS mediated signaling is frequently deregulated in HGSOC (Bell *et al.*, 2011), pairwise combinations of these oncogenes were cloned into appropriate lentiviral vectors, as schematically shown in Fig. 4A. These constructs contained V5-tagged KRAS^{G12V} (hyperactive) and either HA-tagged myristoylated Akt1 (hyperactive), HA-tagged PI3K^{E545K} (hyperactive) or c-Myc. The two ORFs were separated by the porcine teschovirus-1 2A (P2A) sequence to allow for polycistronic gene expression (Kim *et al.*, 2011; Liu *et al.*, 2017). Cells were lentivirally transduced, selected and cancerous outgrowth was closely monitored for 3 months (Fig. 4B). Expression levels of respective oncogenes were analyzed by Western blotting (Fig. 4C). Here, the expression of Akt1, MYC and PI3K was confirmed, although differences in expression levels were evident. Interestingly, KRAS expression was only detected in KRAS^{G12V}/myrAkt1 and KRAS^{G12V}/MYC cell lines.

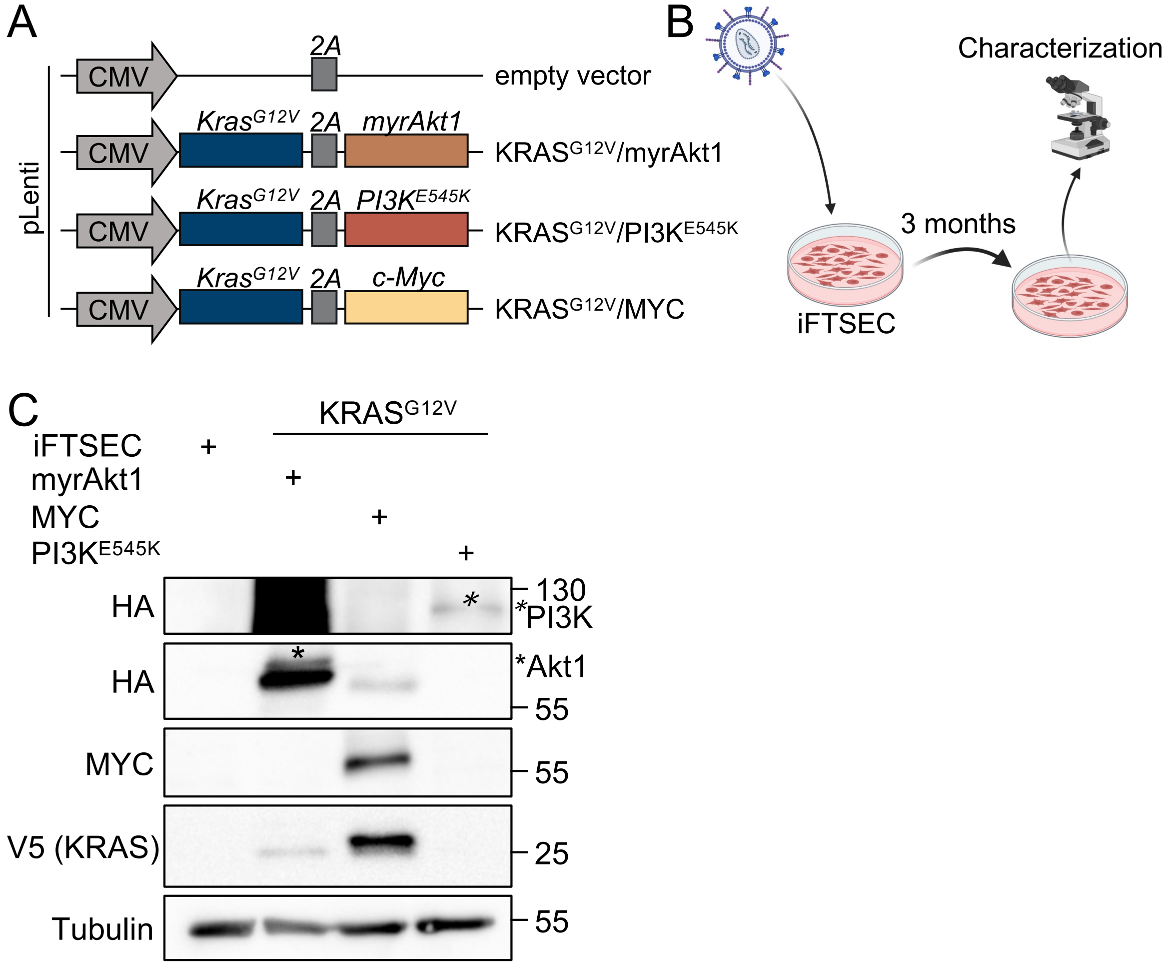

Fig. 4: Lentiviral strategy for transforming iFTSEC into cancer cells.
(A) Schematic representation of lentiviral vectors constructed in this work. **(B)** Transduced iFTSEC were selected for 3 months using 7.5 µg/ml Blasticidin and subsequently analyzed for cancerous transformation. **(C)** Protein expression of transduced iFTSEC after 3 months of selection was detected using Western-blotting, the position of molecular weight markers is indicated.

3.1.2 Lentiviral transduction using KRAS^{G12V} and MYC oncogenes induces cancerous transformation of iFTSEC

The next question was whether the expression of these oncogenes transformed the immortalized cells into tumor cells, as defined by the acquisition of characteristic cancer features. (Hanahan and Weinberg, 2011; Hanahan, 2022). The proliferation assay showed a significant increase in the proliferation rate of the KRAS^{G12V}/MYC cell line compared to the other cell lines shown (Fig. 5A). Furthermore, phenotypic analysis via actin/tubulin immunofluorescence revealed a significant cell size decrease of KRAS^{G12V}/PI3K^{E545K} and KRAS^{G12V}/MYC cell lines (Fig. 5B, top panel, C). To test the ability to grow independently of anchorage, a three-dimensional soft agar colony formation assay was performed (Borowicz *et al.*, 2014). Single cells were seeded and incubated for 14 days. Only KRAS^{G12V}/MYC-transformed cells showed colony formation (Fig. 5B lower panel).

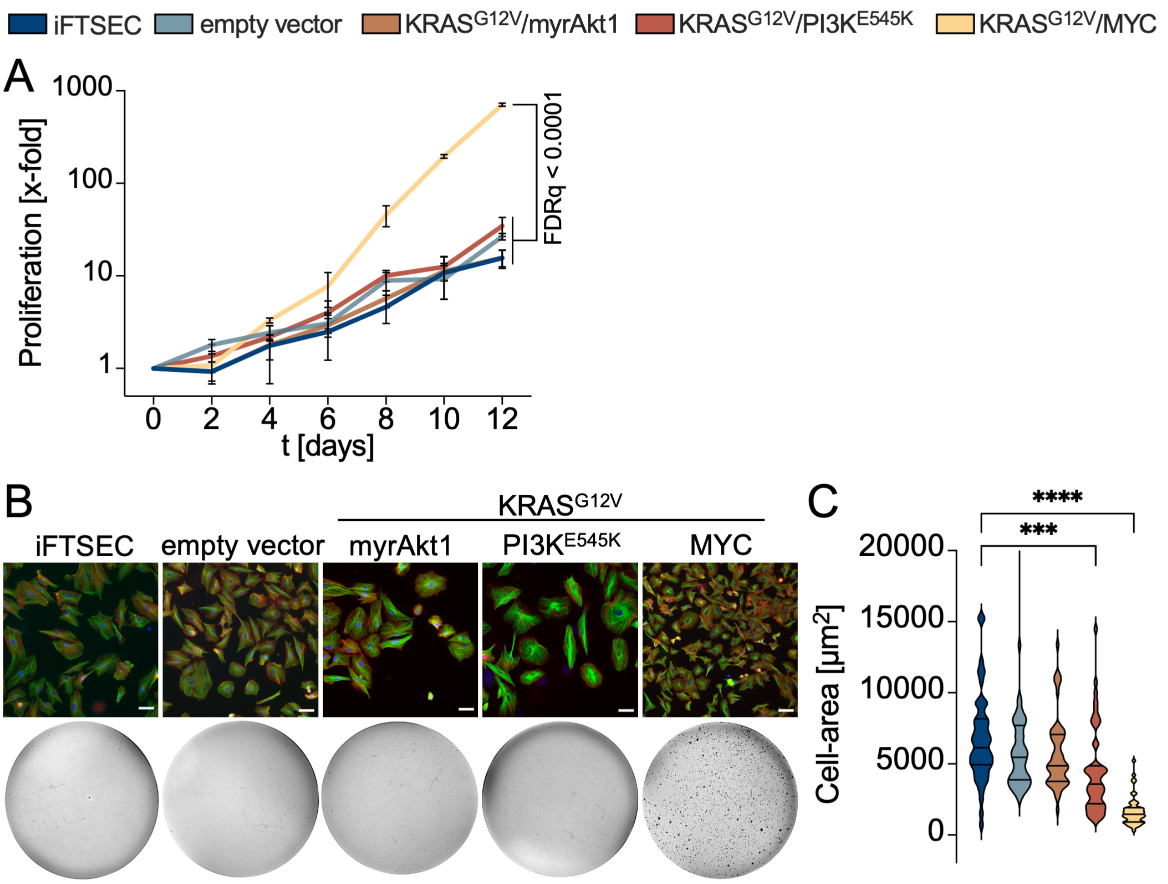

Fig. 5: KRAS^{G12V}/MYC transduced iFTSEC show morphologic changes, increased proliferation and anchorage independent growth.
(A) 5 x 10^4 cells per cell line were seeded in 6-well plates and cell number was analyzed every two days for a total of 12 days. Shown are mean ± SD, n = 3, FDR q values. **(B, upper panel)** Phalloidin (red) and tubulin (green) immunofluorescence analysis of cell morphology. Scale bar, 100 µm. **(B, lower panel)** 2 x 10^4 cells were seeded in soft-agar and medium was refreshed twice weekly. After 12 days of growth, colonies were stained using crystal violet. **(C)** The size of 50 cells per cell line was quantified using FIJI. ***P ≤ 0.001, ****P ≤ 0.0001, one-way ANOVA after Dunnett's multiple comparisons test.

In addition to increased proliferation and anchorage-independent growth, cancer cells may develop mechanisms that increase their migration and invasion rates. The ability of cells to migrate can be tested by scratch assays, which revealed increased migration only for the KRAS^{G12V}/MYC cells (Fig. 6A, B). The trans-well invasion assay (Fig. 6C) is a more sophisticated method for studying the ability of cells to migrate (- collagen) or invade (+ collagen). KRAS^{G12V}/MYC cells showed significantly higher number of migrated and invaded cells, as compared to iFTSEC and empty vector cell lines (Fig. 6D).

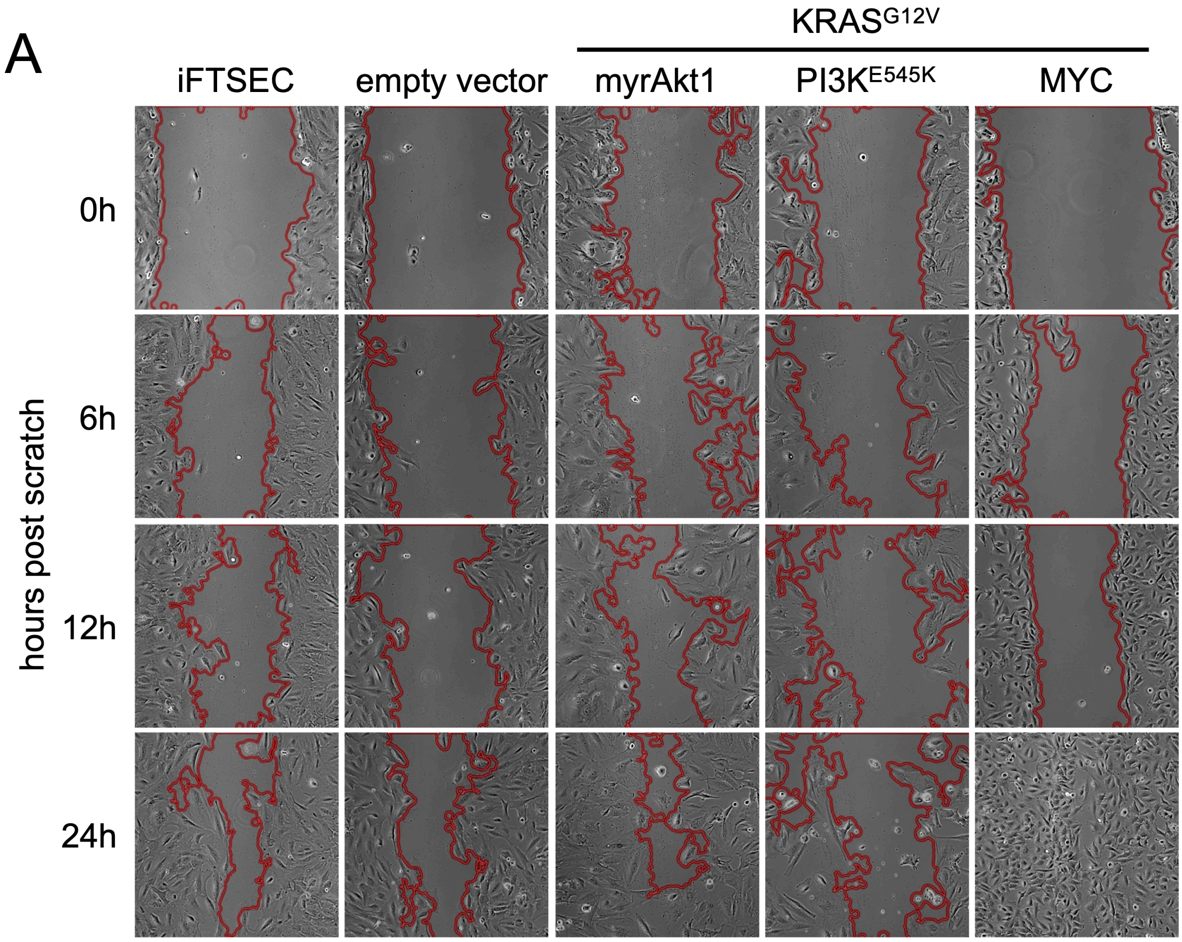

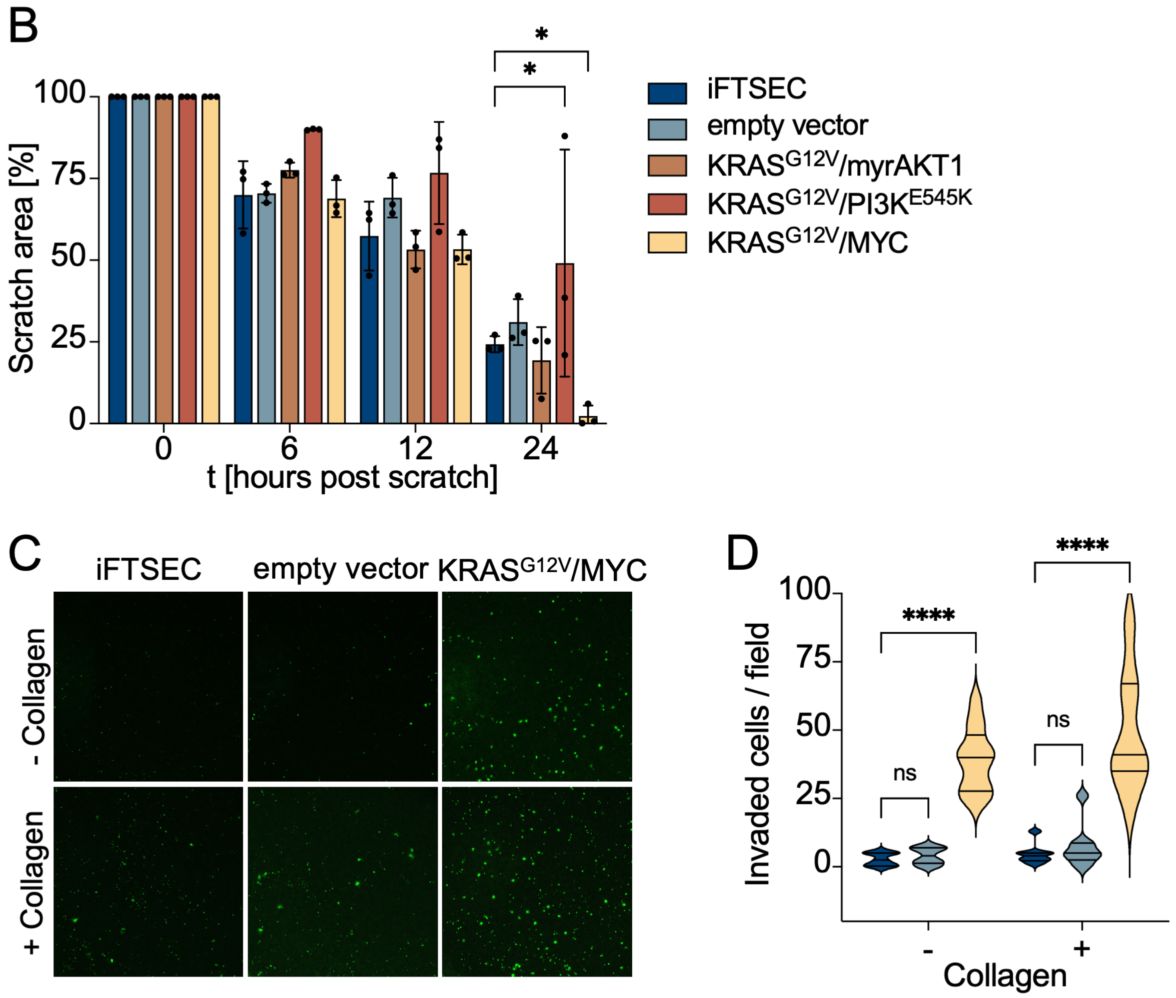

Fig. 6: KRAS^{G12V}/MYC transduced iFTSEC show increased migratory and invasive capacity.
(A) 0.8 x 10^5 cells per cell line were seeded in 6-well plates and cultured in 1% FCS for 16 hours before scratching to stop proliferation. Images of the same position were taken at the indicated time points after scratching. **(B)** Quantification of scratch area using FIJI. The scratched area in the control iFTSEC cells was set to 100%. **(C)** 0.1 x 10^6 cells were exposed to 24 hours of serum starvation, followed by plating in transwell chambers with and without collagen coating. Migration (- collagen) or invasion (+ collagen) was allowed for 24 hours. Images of the GFP$^+$ - migrated cells were obtained and image analysis was performed using ImageJ software. Quantification is expressed as the percentage of invaded cells. **(D)** Quantification of invaded cells using FIJI. Shown are mean ± SD, n = 3, *P ≤ 0.05, ****P ≤ 0.0001, two-way ANOVA after Dunnett's multiple comparisons test.

In summary, KRAS^{G12V}/MYC was the only cell line that tested positive in all assays assessing cancer transformation. The empty vector cell line showed no significant differences compared to iFTSECs.

3.1.3 Validation of cell lines after 6 months of cell culture

To ensure cell line integrity, expression of the integrated constructs (depicted in Fig. 4) was analyzed via qPCR after 6 months of continuous cell culture. The KRAS^{G12V}/MYC cell line showed high level gene expression of *KRAS, MYC* and the selection marker blasticidin S deaminase (*BSD*) (Fig. 7A). Furthermore, Western blotting confirmed protein expression of MYC and KRAS^{G12V} (Fig. 7B).

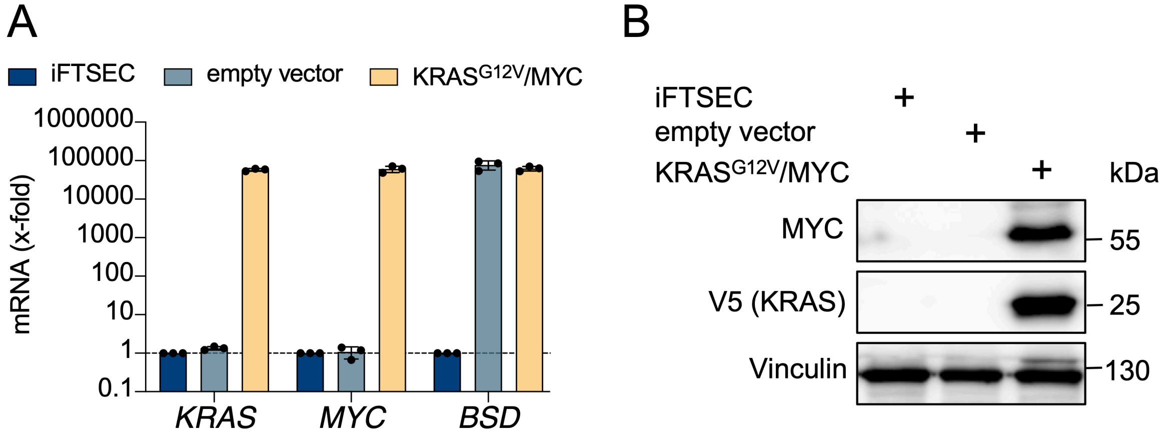

Fig. 7: Stable integration and expression of KRAS^{G12V} and MYC mRNA and protein.
(A) The indicated cell lines were analyzed for their mRNA expression of *KRAS, MYC* and blasticidin S deaminase (BSD). Expression levels of empty vector and KRAS^{G12V}/MYC cell lines were compared to iFTSECs. **(B)** The indicated cells were analyzed for expression of the indicated proteins by immunoblotting.

For the remainder of this study, KRAS^{G12V}/MYC-transduced iFTSEC cells are used as a cancer model, whereas empty vector-transduced iFTSEC cells represent an adequate non-cancerous immortalized control cell line.

3.1.4 KRAS and MYC signaling is upregulated in KRAS^{G12V}/MYC transformed cancer cells

Empty vector and KRAS^{G12V}/MYC cells were subjected to transcriptomic analysis to investigate their gene expression signatures after cancer transformation. RNA was extracted and three biological replicates were analyzed by RNA-seq for differential expression of genes. The analysis detected the differential regulation of 3815 RNAs (P <0.05; $\log_2$FC >1, <-1). Due to codon optimization this analysis did not detect *MYC* and *KRAS,* but rather their downstream targets *MYCT1* (MYC target 1) and *ESX1* (ESX1 Homeobox 1), respectively (Fu *et al.*, 2018) (Nakajima *et al.*, 2008) (Fig. 8A). In addition, gene set enrichment analysis verified the up-regulation of

KRAS and MYC signaling in KRAS^{G12V}/MYC cancer cells (Fig. 8B). Furthermore, bioinformatic analysis using the ShinyGOv0.75 tool underscored the significant enrichment of genes involved in KRAS and MYC signaling pathways (Fig. 8C).

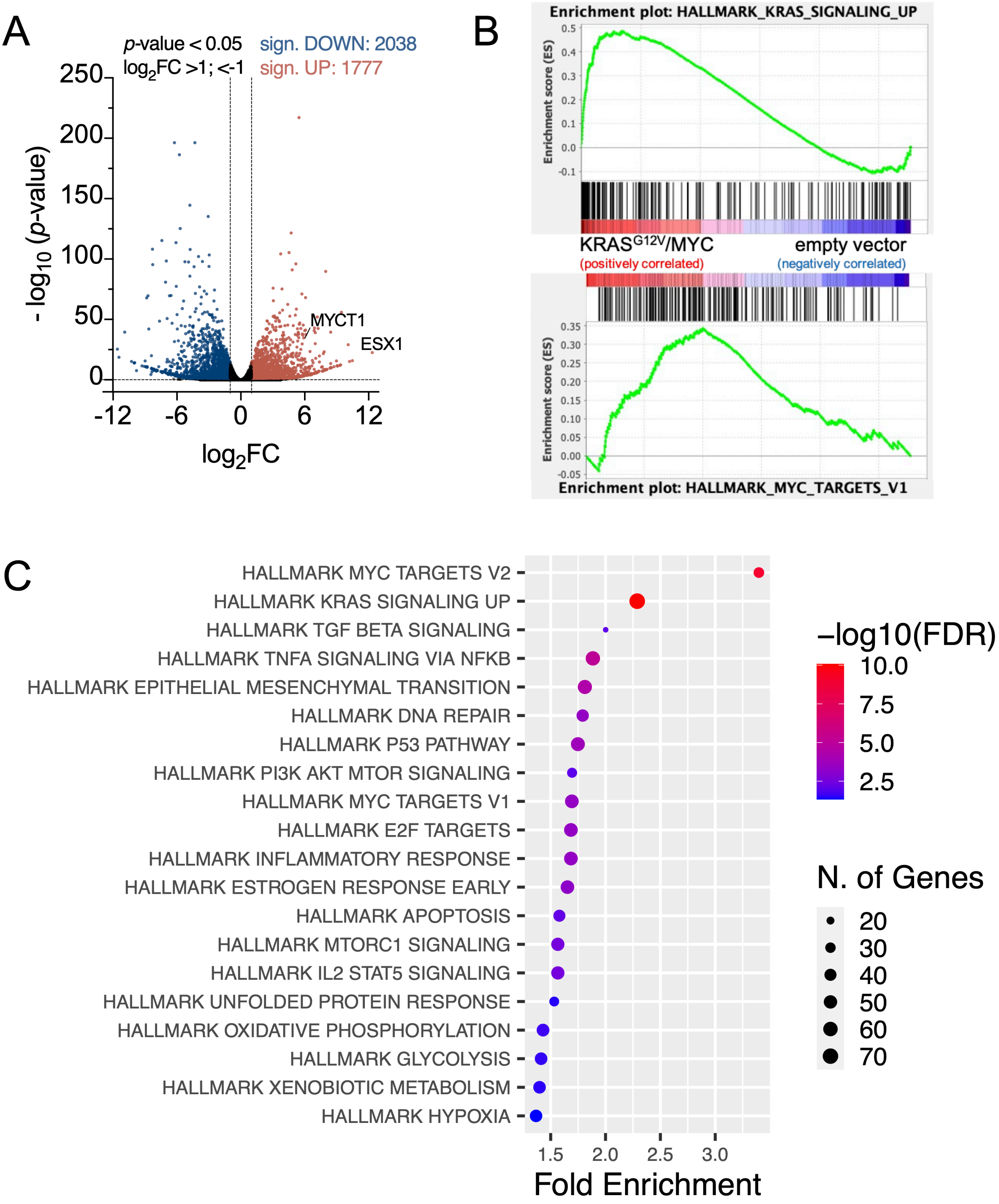

Fig. 8: Transcriptome analysis reveals upregulated KRAS and MYC signaling. 0.5 x 10^6 cells per cell line were seeded in 10 cm dishes and cultured for 1 day followed by RNA isolation and RNA sequencing, n = 3. **(A)** Volcano plot of differential expressed genes. Cutoff: P<0.05, log$_2$-fold change >1; <-1. **(B)** Gene set enrichment analysis of KRAS^{G12V}/MYC cells versus empty vector controls,

differential expression of the KRAS- and MYC-regulated genes is shown **(C)** All significantly upregulated genes were analyzed with ShinyGOv0.75 and enrichment analysis was performed using the HALLMARK database.

3.1.5 Glycolysis is upregulated in KRAS^{G12V}/MYC cancer cells

As most cancer cells adapt to their increased energy requirements by up-regulating glycolysis (Warburg, 1956), Seahorse metabolic flux analyses were performed. This system allows for sensitive measurement of oxygen consumption rate (OCR) as a direct indicator for the rate of oxidative phosphorylation. Simultaneous measurement of extracellular acidification rate serves as a readout for the rate of glycolysis. Addition of Oligomycin, FCCP and Rotenone/Antimycin A interferes with the electron transport chain on different levels, allowing differential analysis of specific steps during OXPHOS (Fig.9C). Empty vector and KRAS^{G12V}/MYC cells showed a similar OCR (Fig. 9A, C), whereas KRAS^{G12V}/MYC cells presented with a significant increase in basal and maximal glycolysis (Fig. 9B, D).

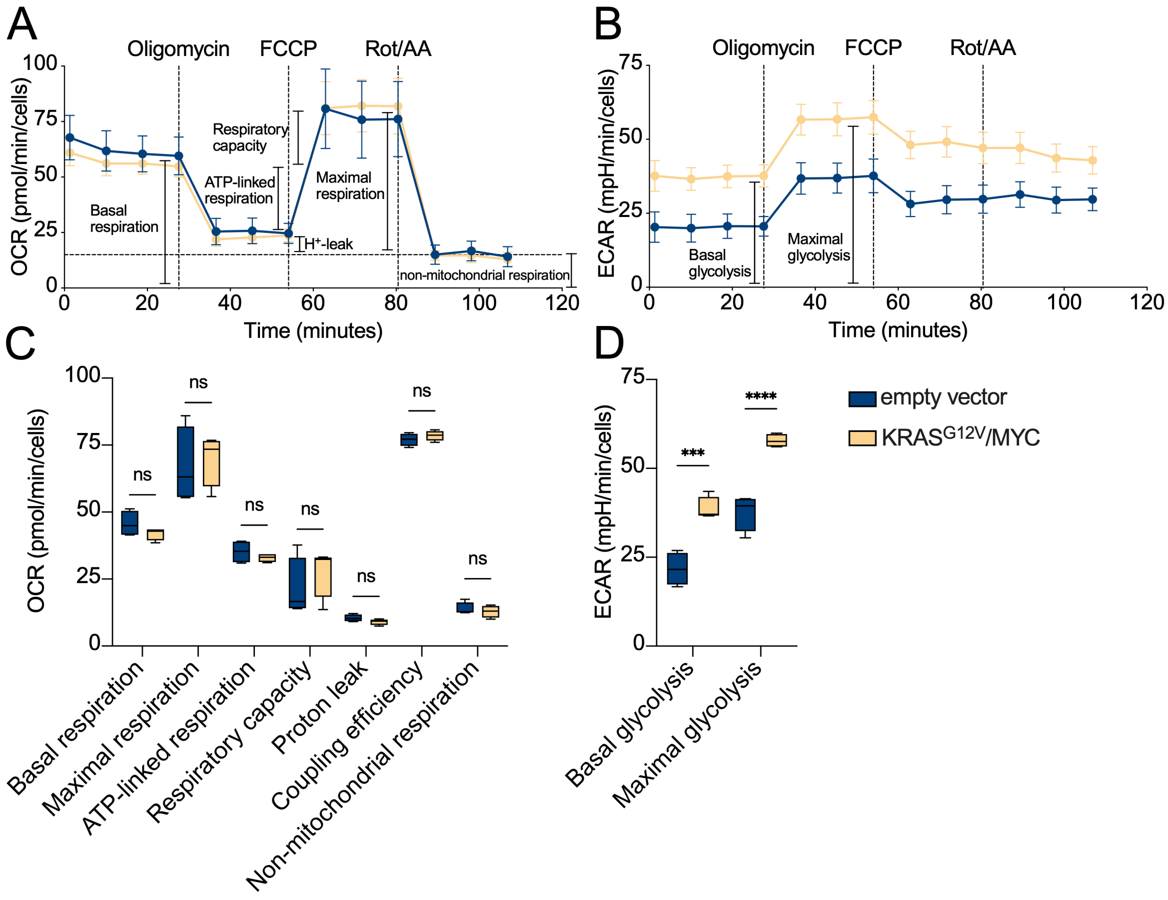

Fig. 9: Glycolysis is upregulated in KRAS^{G12V}/MYC cancer cells.
To be continued on next page.

Seahorse metabolic flux analysis was performed using the MitoStress kit from Agilent. Cells received 0.135% DMSO for 4 hours followed by Seahorse analysis. Oligomycin (2 µM), FCCP (2 µM) and Rotenone/Antimycin A (1 µM) were injected into the wells at the indicated time points. **(A, C)** Quantification of the oxygen consumption rate (OCR). **(B, D)** Quantification of the extracellular acidification rate (ECAR). Shown are mean ± SD, n = 4, ***P ≤ 0.001, ****P ≤ 0.0001, two-way ANOVA after Šídák's multiple comparisons test.

3.2 Identification of a novel synergistic drug combination

3.2.1 Screening of synthetic lethal metabolic inhibitor combination

Since initial Seahorse experiments showed metabolic changes between the control and KRAS^{G12V}/MYC cells, I aimed to exploit these metabolic differences as an entry point for selective targeting of cancer cells. Based on intensive literature research, 17 metabolic inhibitors were selected with regard to their target selectivity, potency, pharmacokinetics and dynamics, *in vivo* use, clinical use, widespread use in the life sciences, citations, and availability. Sublethal concentrations of each inhibitor were determined using dose-response assays in KRAS^{G12V}/MYC cells. Subsequently, a combination of sublethal concentrations of all inhibitors was performed (Fig. 10A). Out of 136 inhibitor combinations, only two achieved a strong cytotoxic effect:

1. (R)-GNE-140 + Metformin
2. (R)-GNE-140 + BMS-986205

These combinations were then tested on empty vector cells to assess their cancer cell selectivity (Fig. 10B). The combination of (R)-GNE-140 and Metformin induced similar levels of cytotoxicity between empty vector and KRAS^{G12V}/MYC cell lines. In contrast, the combination of (R)-GNE-140 and BMS-986205 exerted significantly higher cytotoxicity against KRAS^{G12V}/MYC cancer cells as compared to non-cancerous empty vector cells.

To address if the combination of (R)-GNE-140 and BMS-986205 achieves synergistic cytotoxicity, iFTSEC, empty vector and KRAS^{G12V}/MYC cell lines were subjected to mono and combination treatments (Fig. 10C). These experiments showed that the combination of (R)-GNE-140 and BMS-986205 significantly decreased cell-viability of all cell lines, resulting in similar synergy, while the coefficient of drug interaction demonstrates increased drug synergy for KRAS^{G12V}/MYC cancer cells (Fig. 10D). However, a significantly stronger decrease of cell-viability after (R)-GNE-140 and BMS-986205 combination treatment was observed for KRAS^{G12V}/MYC cancer cells (Fig. 10C). No differences were observed between iFTSEC and empty vector cells. The known enzymatic targets of (R)-GNE-140 and BMS-986205 are LDHA/B (lactate fermentation) and IDO1 (tryptophan catabolism), respectively (Fig. 10E).

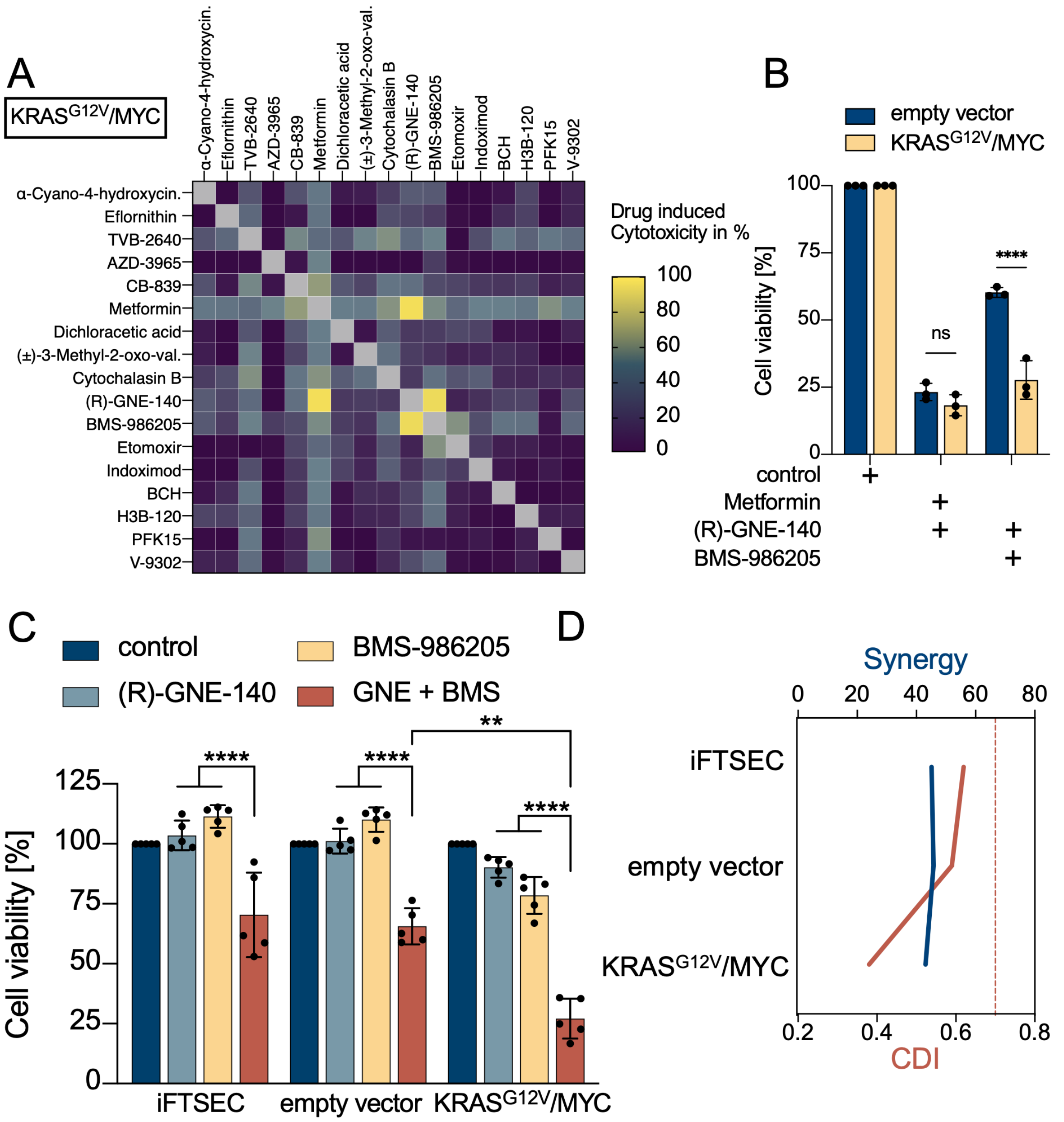

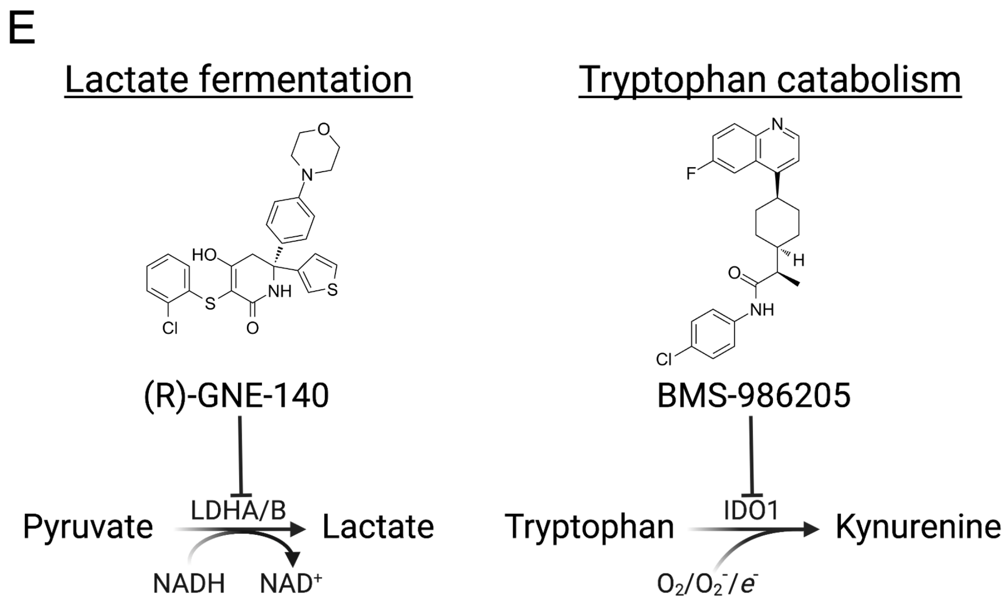

Fig. 10: The combination of (R)-GNE-140 and BMS-986205 exerts synergistic cytotoxicity.

(A) Drug-combination screening using sublethal concentrations (2.4.5) on KRAS^{G12V}/MYC cells in 96-well plates for 3 days followed by crystal-violet cell-viability assay. **(B)** Validation of the depicted drug combinations effects on cell viability of empty vector and KRAS^{G12V}/MYC cells for 3 days followed by crystal-violet cell-viability assay. Shown are mean ± SD, n = 3, two-way ANOVA after Šídák's multiple comparisons test. **(C)** Validation of (R)-GNE-140 (7.5 µM) and BMS-986205 (6 µM) mono and combination treatments on iFTSEC, empty vector and KRAS^{G12V}/MYC cells for 3 days followed by crystal-violet cell-viability assay. Shown are mean ± SD, n = 4, $^{**}P \leq 0.01$, $^{***}P \leq 0.001$, $^{****}P \leq 0.0001$, two-way ANOVA after two-stage linear step-up procedure of Benjamini, Krieger and Yekutieli. **(D)** Synergy is shown in %-points and coefficient of drug interaction (CDI), as previously described (2.5). The red line marks the significance threshold of $\leqq 0.7$. **(E)** Schematic representation of the known enzymes and pathways targeted by (R)-GNE-140 and BMS-98605.

3.2.2 (R)-GNE-140 and BMS-986205 achieve synergistic cytotoxicity in a 3D environment

The soft agar colony formation assay allows for a robust study of drug effects, as the 3D environment of the cells is more closely resembles the *in vivo* situation as compared to growth in a 2D cell culture (Anderson *et al.*, 2007). Once cells were seeded and robust colony formation was observed, KRAS^{G12V}/MYC cells were subjected to mono- or combination treatment (Fig. 11A). After 12 days of constant drug exposure, colonies were stained and quantified using FIJI image analysis software (Fig. 11B). Treatment with (R)-GNE-140 had no impact on colony formation, although slight changes in colony morphology were observed. BMS-

986205-treated cells showed significantly reduced colony formation with non-delineated margins. The combination of (R)-GNE-140 and BMS-986205 strongly impaired colony formation and resulted in significantly smaller colonies surrounded by cell debris.

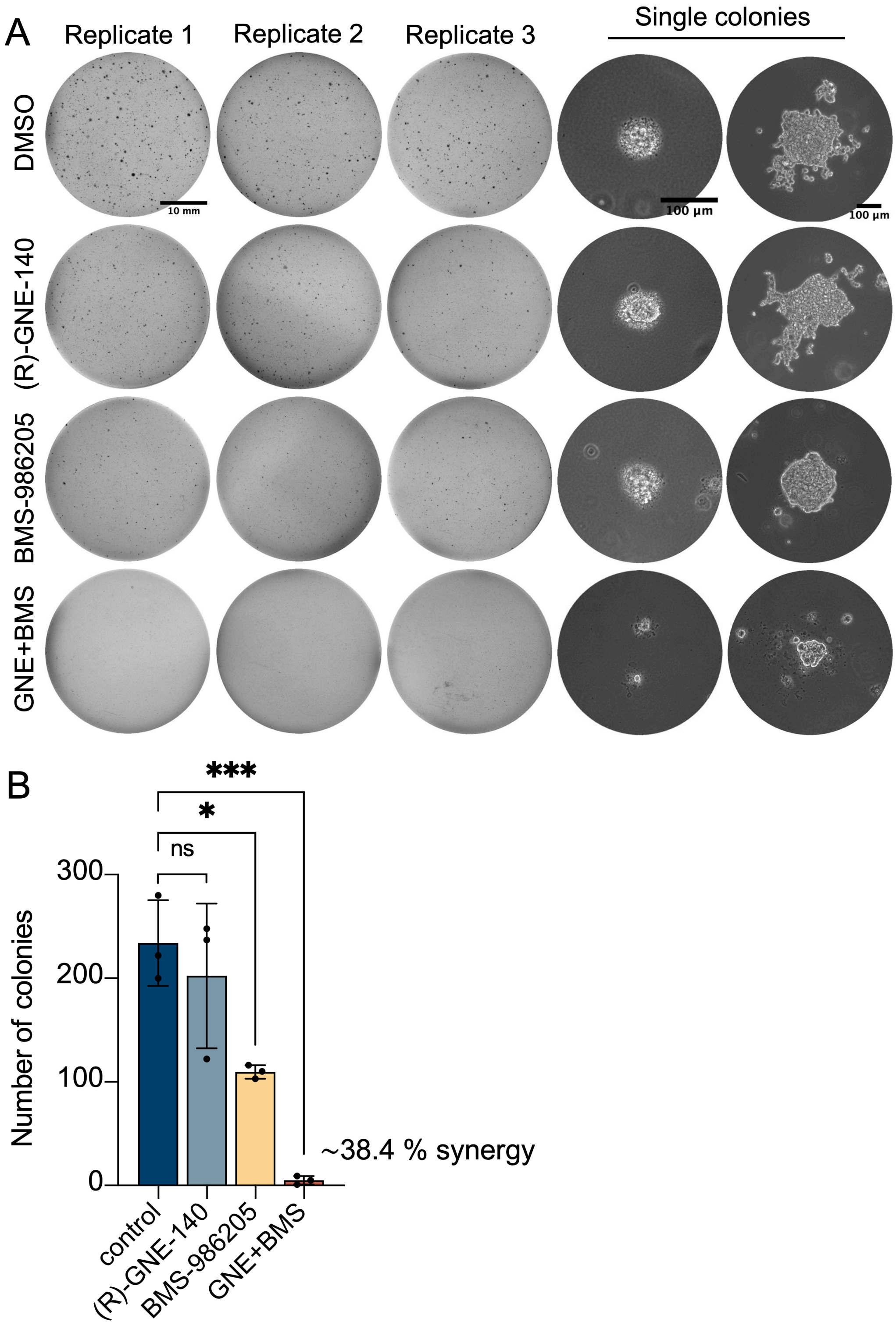

Fig. 11: Synergy of (R)-GNE-140 and BMS-986205 combination in soft agar.

(A) 2 x 10^4 KRAS^{G12V}/MYC cells were seeded in soft agar and incubated for 5 days to allow colony formation. Then, cells received DMSO (0.135%), (R)-GNE-140 (7.5 µM) and BMS-986205 (6 µM) mono or combination treatment for 12 days total. Cells were restimulated 7 days after receiving initial treatment. Colonies were stained with crystal violet. **(B)** Number of colonies was quantified using FIJI. Synergy is shown in %-points and calculated as previously described. Shown are mean ± SD, n = 3, *P ≤ 0.05, **P ≤ 0.01, one-way ANOVA after Tukey's multiple comparisons test.

3.3 Phenotypic and molecular characterization of combination treatment effects

3.3.1 Increased cell size after (R)-GNE-140 and BMS-986205 combination treatment

Using brightfield microscopy, phenotypic changes were noticed after combination therapy. To facilitate visualization and image quantification, the actin/tubulin cytoskeleton was stained and analyzed by immunofluorescence (Fig.12A). These images further revealed morphologic changes, specifically in KRAS^{G12V}/MYC cancer cells. Quantification of 200 cells per condition showed a significant cell size increase of empty vector and KRAS^{G12V}/MYC cells after combination treatment (Fig.12B).

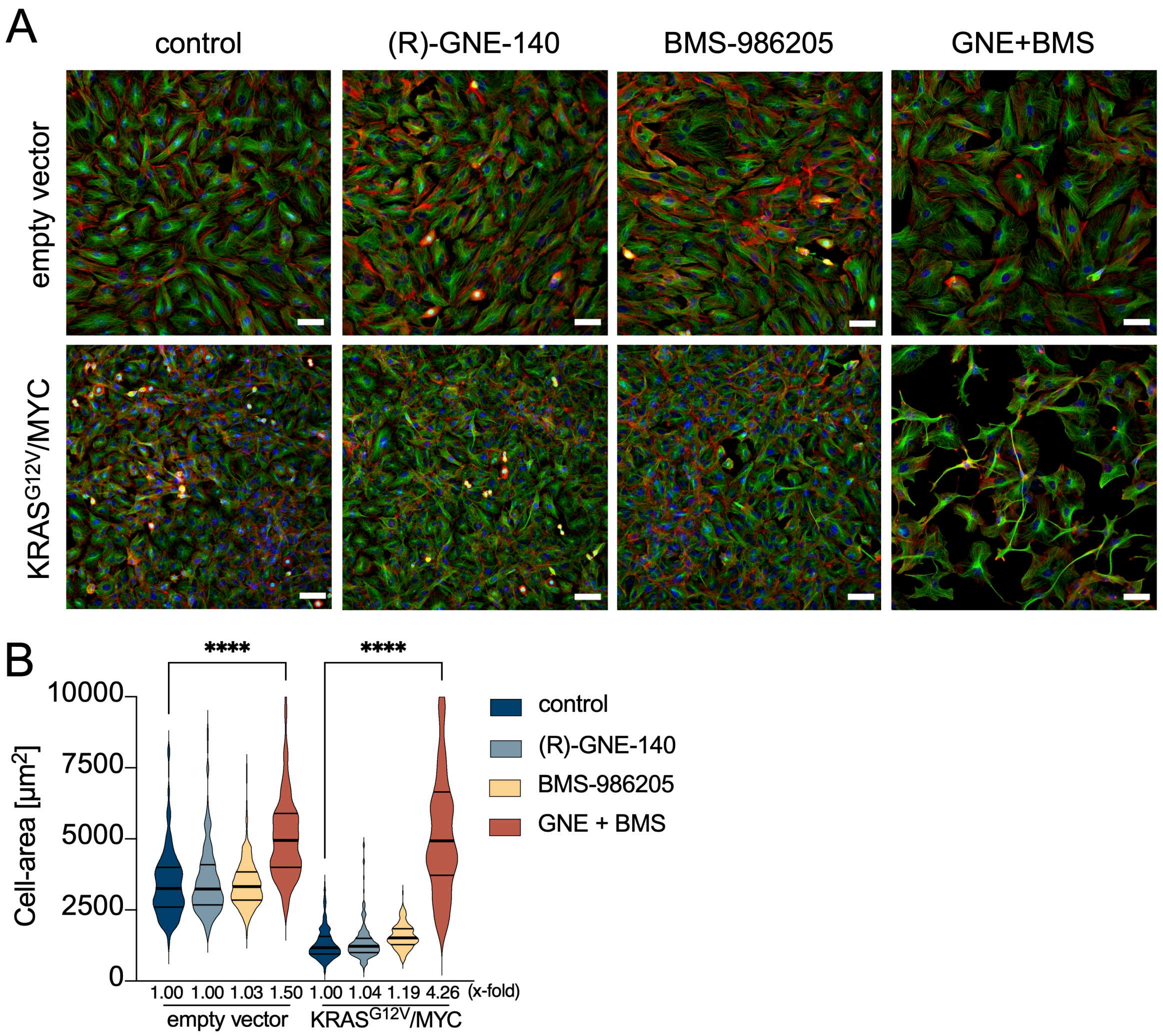

Fig. 12: (R)-GNE-140 and BMS-986205 combination treatment increases cell size.
0.75 x 10^5 empty vector and 0.5 x 10^5 KRAS^{G12V}/MYC cells were seeded in 6-well plates and incubated for 1 day, followed by 3 days of incubation with the indicated treatments. **(A)** Phalloidin/actin (red), tubulin (green) and nuclei (blue) immunofluorescence staining of empty vector and KRAS^{G12V}/MYC cells. Scale bar, 100 µm. **(B)** Cell size quantification of 200 cells per cell line. Shown are violin plot quartiles, n = 3, ****$P \leq 0.0001$, one-way ANOVA after Tukey's multiple comparisons test.

3.3.2 (R)-GNE-140 and BMS-986205 induces senescence in KRAS^{G12V}/MYC cells

One of the hallmarks of senescent cells is their enlarged and flattened morphology, which has been previously identified in this study (Fig.12) (Dodig, Čepelak and Pavić, 2019). To test whether the combination treatment induced senescence in empty vector and KRAS^{G12V}/MYC cells, the activity of ß-galactosidase, a commonly used senescence marker (Dimri *et al.*, 1995), was determined. Senescence-associated ß-galactosidase (SA-ß-gal) activity was significantly increased in KRAS^{G12V}/MYC cells (Fig. 13A) as compared to empty vector cells after 3 days of combination treatment (Fig. 13B). Furthermore, quantification of cells presenting with increased SA-ß-gal activity was performed over the course of seven days following combination treatment (Fig. 13C). Empty vector cells showed a maximum of ~20% SA-ß-gal positive cells 6 days post combination treatment, whereas KRAS^{G12V}/MYC cells reached their maximum of ~75-80% 4 days post combination treatment. Brightfield images revealed an intensification of the perinuclear SA-ß-gal activity signal over time in KRAS^{G12V}/MYC cells (data not shown).

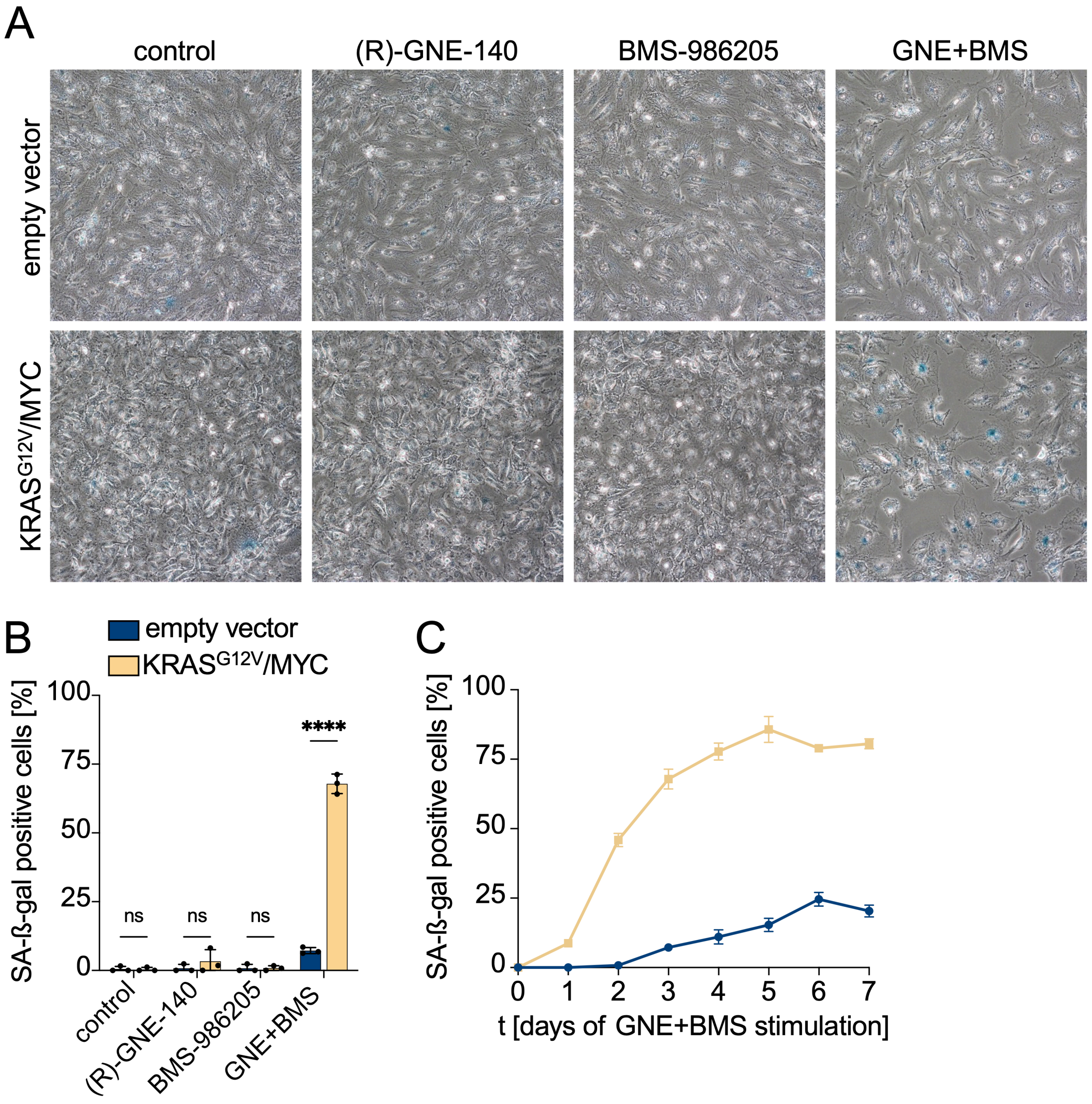

Fig. 13: (R)-GNE-140 and BMS-986205 selectively induces senescence in KRAS^{G12V}/MYC cells.
To be continued on next page.

(A) ß-galactosidase activity staining of 0.75 x 10^5 empty vector and 0.5 x 10^5 KRAS^{G12V}/MYC cells, which were seeded in 6-well plates and incubated for 1 day, followed by 3 days of treatment with DMSO (0.135%), (R)-GNE-140 (7.5 µM) and BMS-986205 (6 µM) mono or combination treatment. **(B)** Image quantification of ß-galactosidase positive cells in one image. Shown are mean ± SD, n = 3, ****P ≤ 0.0001, two-way ANOVA after Šídák's multiple comparisons test. **(C)** Empty vector and KRAS^{G12V}/MYC cells were seeded as described in A, and were treated with (R)-GNE-140 (7.5 µM) and BMS-986205 (6 µM) combination treatment for 1 to 7 days, followed by ß-galactosidase activity staining. Shown are mean ± SD, n = 3.

3.3.3 Senescence induction is p16/p21 independent

Excessive cellular stress is transmitted through the p16-CDK4/6-Rb1 or p53-p21 axes and ultimately leads to cell cycle arrest and induction of senescence or apoptosis (Stein *et al.*, 1999; Kumari and Jat, 2021). p16 and p21 are widely accepted molecular markers whose increased expression indicates the induction of senescence. To test the contribution of the aforementioned senescence-inducing signaling pathways, the expression levels of p16 and p21 were detected by Western blotting (Fig. 14A, B). KRAS^{G12V}/MYC cells did not show increased p16 levels after exposure to the combination treatment for 24 and 48 hours. Expression of p21 was reduced upon combination treatment.

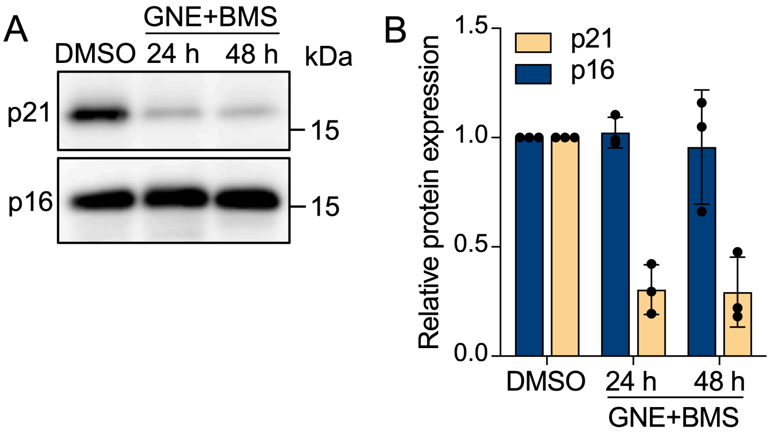

Fig. 14: Senescence induction is p16/p21 independent.
(A) 0.5 x 10^6 KRAS^{G12V}/MYC cells were seeded in 10 cm dishes and treated with (R)-GNE-140 (7.5 µM) and BMS-986205 (6 µM) combination treatment for 24 and 48 hours, followed by analysis for p16 and p21 expression using Western blotting. **(B)** Quantification of p16 and p21 expression levels using FIJI image analysis software. Shown are mean ± SD, n = 3.

3.3.4 (R)-GNE-140 and BMS-986205 combination treatment induces pro-inflammatory gene expression

During the induction of senescence, cells develop a unique secretory program, the senescence-associated secretory phenotype (SASP) which is typically driven by NF-κB (Coppé *et al.*, 2010; Chien *et al.*, 2011; Salminen, Kauppinen and Kaarniranta, 2012). To investigate the putative development of a SASP, the expression of pro-inflammatory genes was assessed by qPCR (Fig. 15). Empty vector and KRAS^{G12V}/MYC cells showed upregulation of a number of key pro-inflammatory NF-κB target genes after 96 hours of (R)-GNE-140 and BMS-986205 combination treatment. Empty vector cells already showed increased pro-inflammatory gene expression in response to BMS-986205 mono treatment, whereas KRAS^{G12V}/MYC cells responded exclusively to the combination treatment. *MMP9* expression was not detected in empty vector cells.

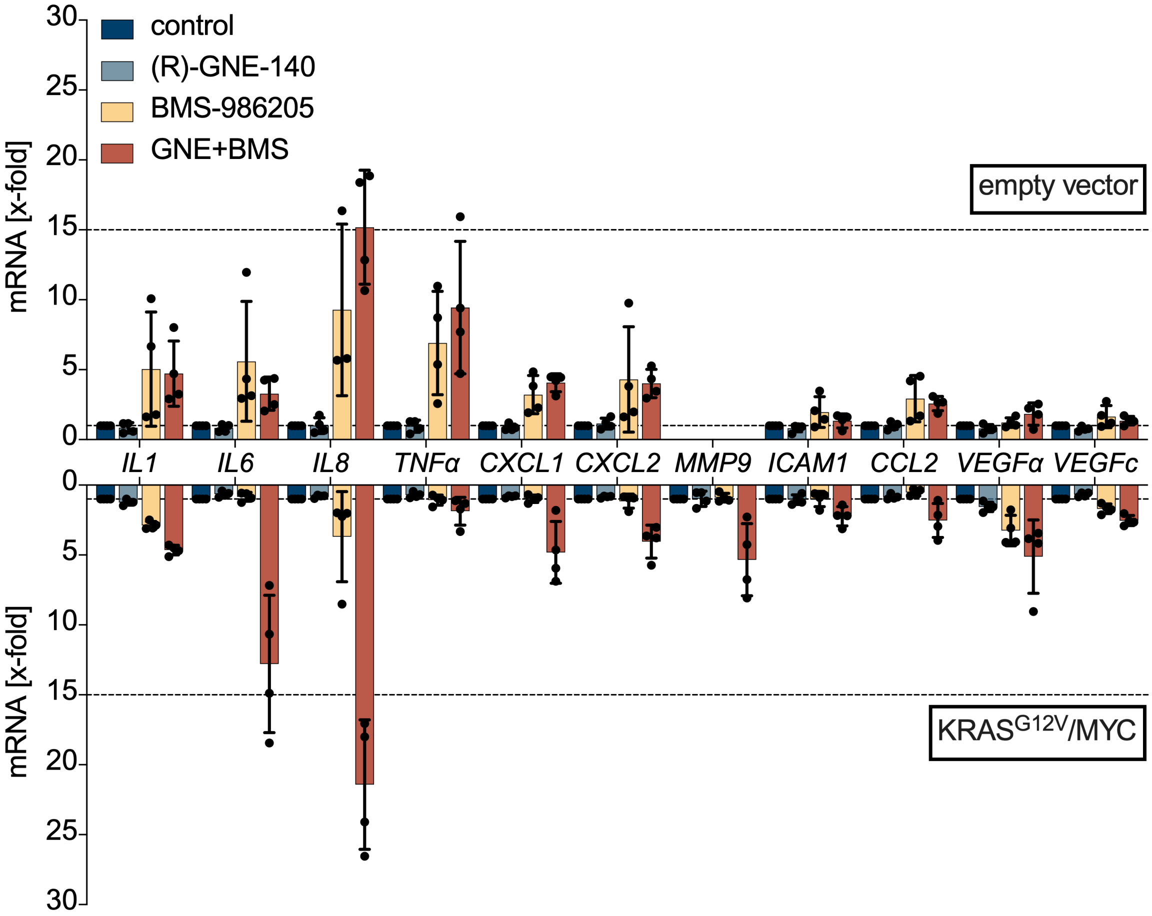

Fig. 15: Combination of (R)-GNE-140 and BMS-986205 induces pro-inflammatory gene expression after prolonged treatment.
To be continued on next page.

0.06 x 10^6 empty vector and 0.02 x 10^6 KRAS^{G12V}/MYC cells were seeded in 10 cm dishes and treated with DMSO (0.135%), (R)-GNE-140 (7.5 µM) and BMS-986205 (6 µM) mono treatment for 96 hours. 0.3 x 10^6 empty vector and 0.2 x 10^6 KRAS^{G12V}/MYC cells were seeded in 10 cm dishes and treated with the combination treatment for 96 hours, followed by gene expression analysis via qPCR. Shown are mean ± SD, n = 4.

3.3.5 (R)-GNE-140 and BMS-986205 combination treatment results in SASP development in KRAS^{G12V}/MYC cells

To test whether (R)-GNE-140 and BMS-986205 treatment resulted in the secretion of pro-inflammatory molecules, supernatants were collected after 96 hours of treatment. Subsequently, naïve cells were treated with these collected supernatants for the indicated time points and the expression of a selection of pro-inflammatory genes was assessed by qPCR (Fig. 16A). Results showed increased pro-inflammatory gene expression in KRAS^{G12V}/MYC cells which were stimulated for 3 hours with supernatants derived from (R)-GNE-140 and BMS-986205 combination treatment (Fig. 16B). Pro-inflammatory gene expression was significantly higher in KRAS^{G12V}/MYC cells compared to empty vector cells, highlighting the exclusive SASP development in KRAS^{G12V}/MYC cells.

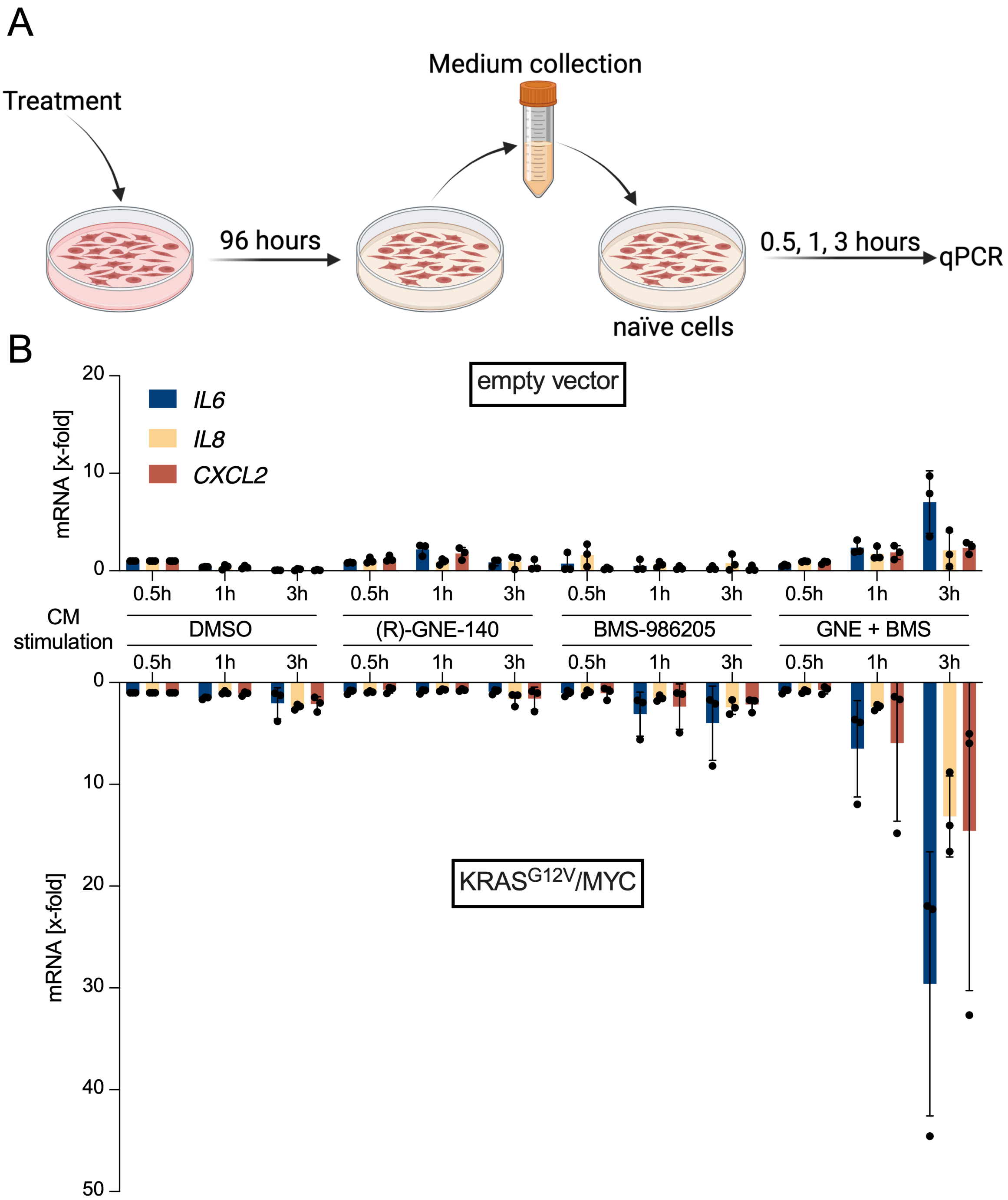

Fig. 16: Combination of (R)-GNE-140 and BMS-986205 leads to the secretion of pro-inflammatory molecules in KRAS^{G12V}/MYC cells.
0.06 x 10^6 empty vector and 0.02 x 10^6 KRAS^{G12V}/MYC cells were seeded in 10 cm dishes and treated with DMSO (0.135%), (R)-GNE-140 (7.5 µM) and BMS-986205 (6 µM) mono treatment for 96 hours. 0.3 x 10^6 empty vector and 0.2 x 10^6 KRAS^{G12V}/MYC cells were seeded in 10 cm dishes and treated with the combination treatment for 96 hours. **(A)** Scheme of the experimental design. **(B)** After treatment supernatants were collected and centrifuged to avoid the possible transfer of cells. Then, 0.1 x 10^6 naïve cells, which were seeded the prior day, were stimulated with the supernatants for 0.5, 1 and 3 hours, followed by analysis of mRNA expression levels via qPCR. Shown are mean ± SD, n = 3. CM = conditioned medium.

3.3.6 Senescent KRAS^{G12V}/MYC cancer cells can be eliminated using senolytics

Induction of senescence in tumor cells reduces the patient’s tumor burden and increases 5-year survival rates (Wang, Lankhorst and Bernards, 2022). However, senescent cells develop the SASP, a deleterious program that can eventually give rise to new cancer cells or lead to chronic inflammation (Coppé *et al.*, 2010). Therefore, selective elimination of senescent cells using senolytic drugs has been proposed as a promising adjuvant therapy to existing cancer therapies (Short *et al.*, 2019). To test whether the (R)-GNE-140 and BMS-986205 combination therapy induced senescent phenotype can be targeted by senolytic drugs, I made use of the well-established senolytic drug Dasatinib (Chaib, Tchkonia and Kirkland, 2022).

Empty vector and KRAS^{G12V}/MYC cells were stimulated with (R)-GNE-140 and BMS-986205 mono- and combination treatment for 48 hours to allow for senescence development. Subsequently, Dasatinib was added to the culture medium for another 24 or 48 hours (Fig. 17A). Cell-viability measurements revealed a significantly higher cytotoxic effect of Dasatinib on KRAS^{G12V}/MYC cells, which received the (R)-GNE-140 and BMS-986205 combination treatment (Fig. 17B), as compared to mono treatments and to the response of the empty vector cell line. Using brightfield microscopy, increased numbers of floating cells were noticed for KRAS^{G12V}/MYC cells following combination treatment and Dasatinib exposure (Fig. 17C). At the molecular level, increased caspase 3 cleavage was detected in empty vector and KRAS^{G12V}/MYC cells following combination treatment and Dasatinib exposure (Fig. 17D). Taken together, Dasatinib selectively eliminates senescent KRAS^{G12V}/MYC cells, presumably via caspase-dependent apoptosis.

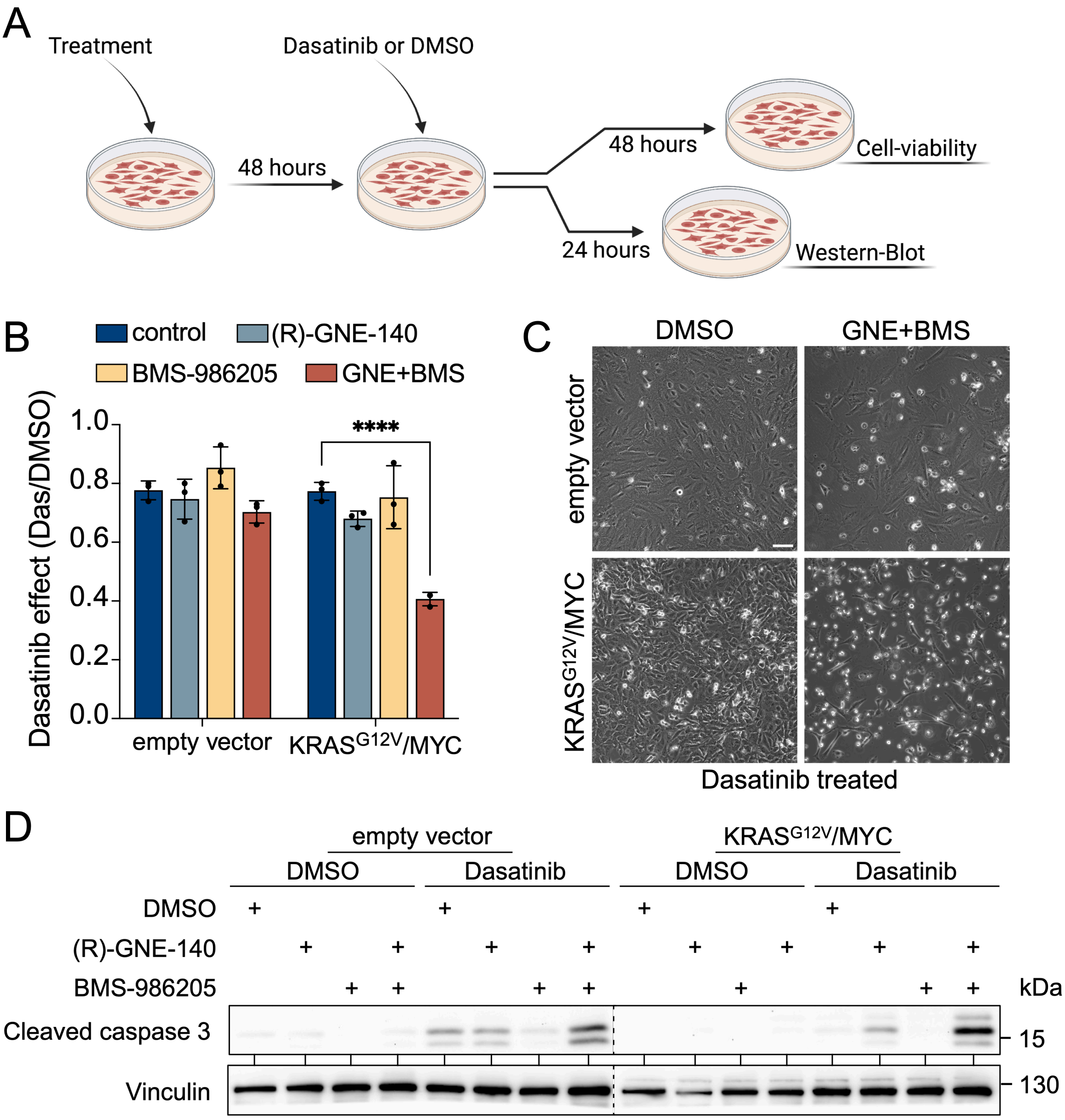

Fig. 17: Induction of apoptosis in senescent cells using the senolytic Dasatinib.
(A) Scheme of the experimental design. Empty vector and $KRAS^{G12V}$/MYC cells received DMSO (0.135%), (R)-GNE-140 (7.5 µM) and BMS-986205 (6 µM) mono or combination treatment for 48 hours, followed by 48 hours Dasatinib (0.05 µM) or DMSO (0.135%) treatment. **(B)** Cell-viability assay reported as Dasatinib effect. Shown are mean ± SD, n = 3, ****P ≤ 0.0001, two-way ANOVA after Dunnett's multiple comparisons test. **(C)** Brightfield images of empty vector and $KRAS^{G12V}$/MYC cells of indicated conditions as previously described. Scale bar, 100 µm. **(D)** Cells were treated as previously described, except that Dasatinib treatment was performed for 24 hours. Protein levels of cleaved caspase 3 were detected using Western blotting.

3.3.7 (R)-GNE-140 and BMS-986205 combination treatment induces cell cycle arrest, DNA-damage and ROS production

In addition to increased cell size, ß-galactosidase activity and SASP, senescent cells undergo a definitive cell cycle arrest (Dodig, Čepelak and Pavić, 2019). To test the cell cycle distribution, empty vector and KRAS^{G12V}/MYC cells were subjected to PI staining followed by flowcytometric analysis (Fig. 18A). Upon combination treatment, accumulation of KRAS^{G12V}/MYC cells in the G2/M cell cycle phase was observed.

Various external and internal stresses such as DNA damage can induce cell cycle arrest. Exposure of cells to (R)-GNE-140 and BMS-986205 resulted in an increase of the DNA double-strand break marker γH2AX, as shown by immunofluorescence imaging (Fig. 18B). The number of γH2AX-positive cells was significantly higher for KRAS^{G12V}/MYC cells as compared to empty vector cells (Fig. 18C).

Since (R)-GNE-140 and BMS-986205 are inhibitors of metabolic enzymes, it was speculated that the source of DNA damage may be of endogenous origin. The most relevant endogenous DNA damaging class of molecules are ROS, including mitochondria-derived superoxide anions (mtROS) (Ray, Huang and Tsuji, 2012; Xu *et al.*, 2020). Empty vector and KRAS^{G12V}/MYC cells were exposed to (R)-GNE-140 and/or BMS-986205 for 2 days and loaded with MitoSox^{TM} to detect mtROS. Mono treatment with BMS-986205 and combination treatment resulted in increased mtROS levels (Fig. 18D). The combination treatment had the stronges effect on KRAS^{G12V}/MYC cells, resulting in an 8-fold increase of mtROS. Additionally, the increase of mtROS was higher in KRAS^{G12V}/MYC cells as compared to empty vector cells.

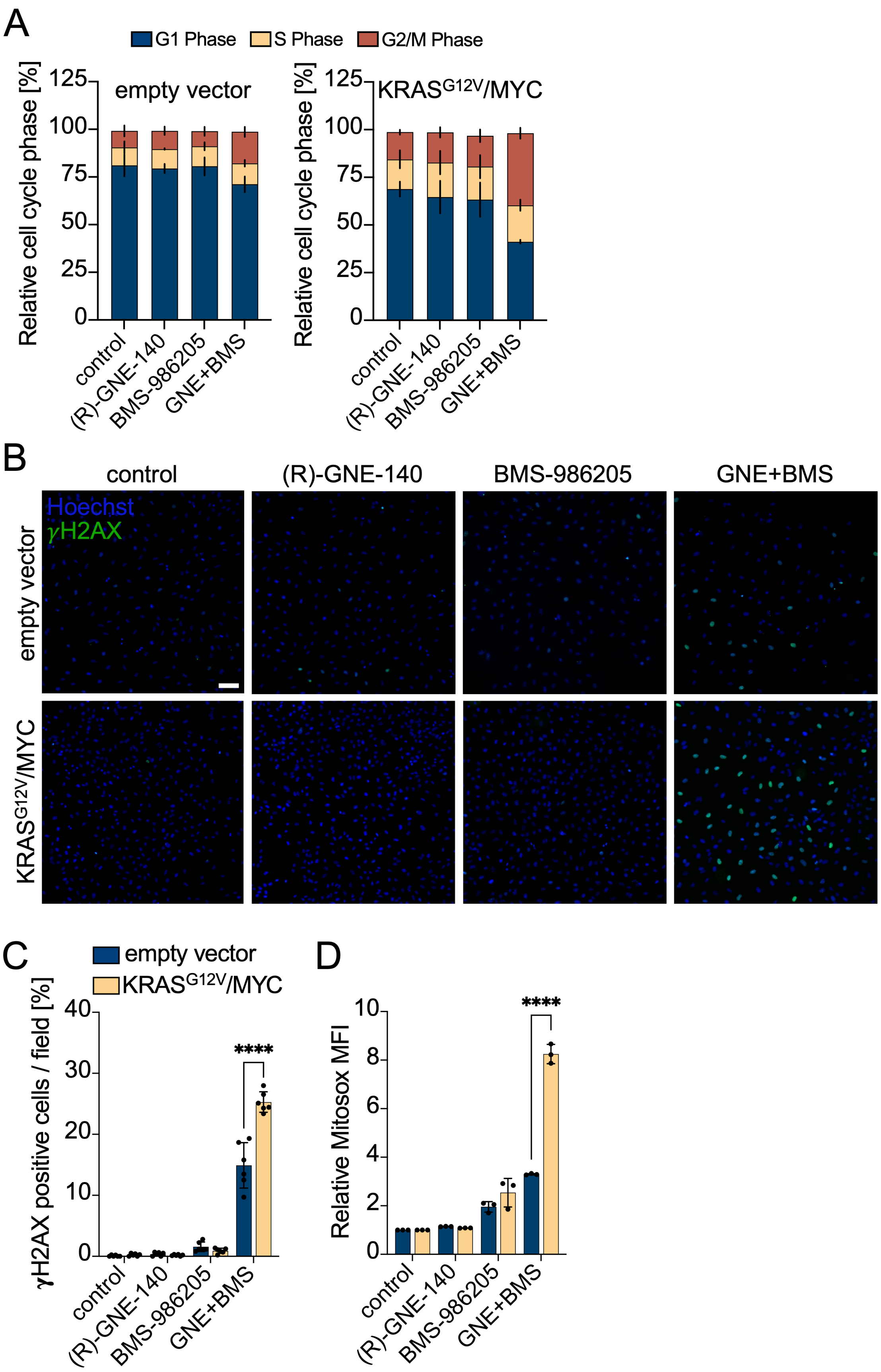

Fig. 18: Cell cycle arrest, DNA damage and increased ROS levels after (R)-GNE-140 and BMS-986205 combination treatment.
To be continued on next slide.

(A) 0.6 x 10^6 empty vector and 0.4 x 10^6 KRAS^{G12V}/MYC cells were seeded in 10 cm dishes and incubated for 1 day and treated with DMSO (0.135%), (R)-GNE-140 (7.5 µM) and BMS-986205 (6 µM) mono or combination treatment for 48 hours, followed by analysis of cell cycle distribution using propidium iodide staining. Quantification of FACS histograms, shown are ± SD, n = 3. **(B)** 0.75 x 10^5 empty vector and 0.5 x 10^5 KRAS^{G12V}/MYC cells were seeded in 6-well plates, incubated for 1 day and then treated with the indicated conditions for 48 hours, followed by immunofluorescence staining of nuclei (blue) and γH2AX (green). Scale bar, 50 µm. **(C)** Quantification of γH2AX positive cells using FIJI image analysis software. Shown are mean ± SD, n = 6. **(D)** 0.6 x 10^6 empty vector and 0.4 x 10^6 KRAS^{G12V}/MYC cells were treated with the indicated conditions for 48 hours. Cells were loaded with 5 µM MitoSox for 10 minutes and subsequently analyzed via flowcytometry for their median fluorescence intensity (MFI). Shown are mean ± SD, n = 3, ****P ≤ 0.0001, two-way ANOVA after Šídák's multiple comparisons test.

3.3.8 Use of different strategies to rescue the effects of (R)-GNE-140 and BMS-986205 combination treatment

According to the literature, (R)-GNE-140 and BMS-986205 treatment reduces intracellular levels of lactate and kynurenine (Purkey *et al.*, 2016; Balog *et al.*, 2021). To test whether addition of these metabolites can rescue cells undergoing (R)-GNE-140/BMS-986205 combination treatment, medium-supplementation experiments were performed. However, the reduction in cell viability mediated by the combination treatment was not rescued by addition of lactate and kynurenine (Fig. 19A).

The combination treatment inhibits lactate fermentation and tryptophan catabolism, two pathways responsible for nicotinamide adenine dinucleotide (NAD) production (Covarrubias *et al.*, 2021). Supplementation of medium with NAD or its precursor nicotinamide riboside (NR) failed to protect KRAS^{G12V}/MYC cells from the effects of (R)-GNE-140 and BMS-986205 combination (Fig. 19B, C).

To understand the role of the previously demonstrated high mtROS levels after combination treatment, KRAS^{G12V}/MYC cells were treated with N-acetylcysteine (NAC) or mitoTempo, two well-known molecules with ROS scavenging properties (Sun, 2010; Ni *et al.*, 2016). Neither of these agents prevented the effects of the combination treatment (Fig. 19D, E). Therefore, the cell damage caused by (R)-GNE-140 and BMS-986205 is not due to individual compounds, but caused by misregulation of a larger and complex metabolic network.

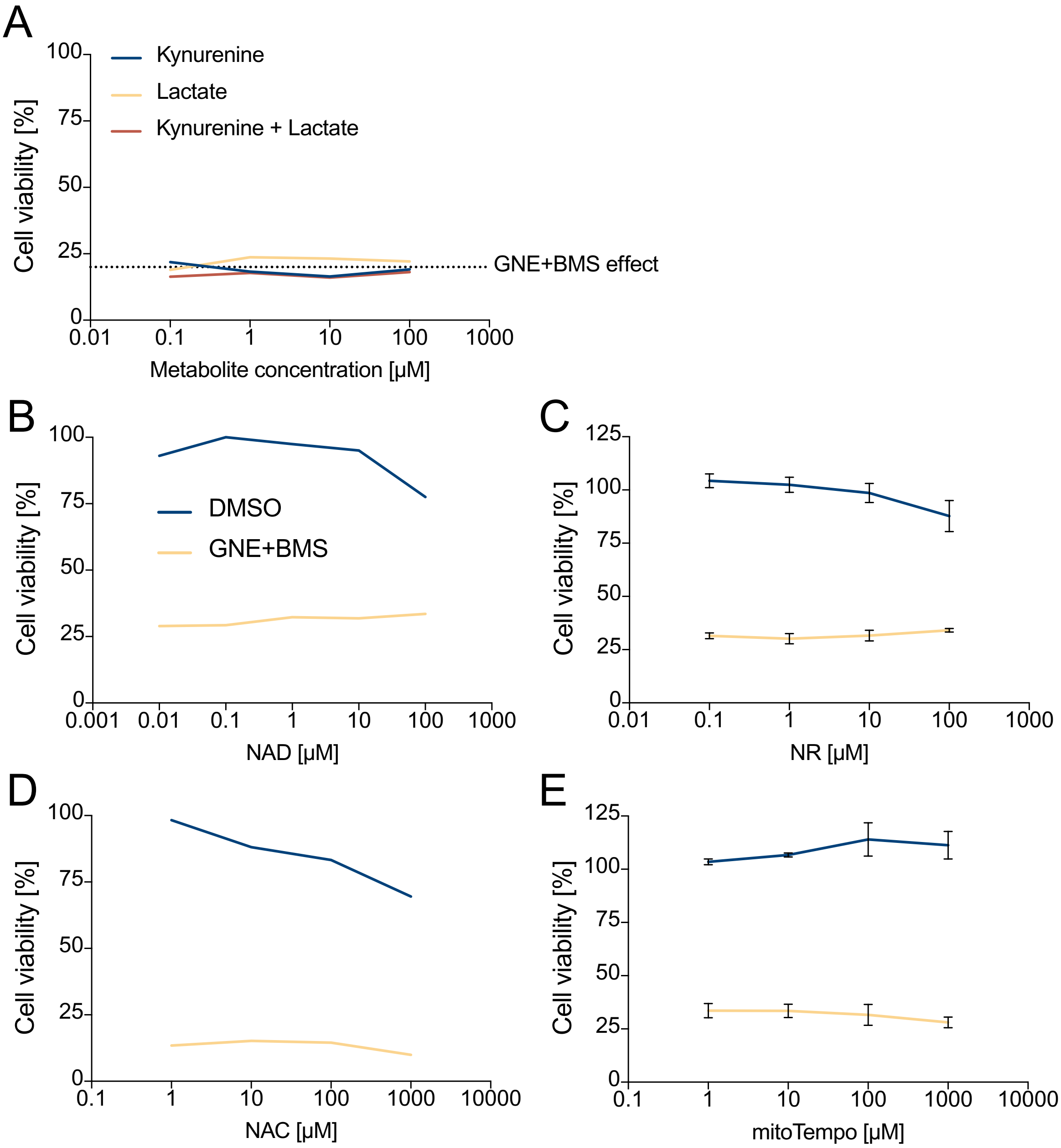

Fig. 19: Different supplementation strategies failed to rescue the effects of (R)-GNE-140 and BMS-986205 combination treatment.

1500 KRAS^{G12V}/MYC cells were seeded in 96-well plates, incubated for 1 day and treated with DMSO (0.135%) or (R)-GNE-140 (7.5 µM) and BMS-986205 (6 µM) combination treatment for 48 hours. One hour pre-treatment with indicated concentrations of **(A)** kynurenine and/or lactate, **(B)** nicotinamide adenine dinucleotide (NAD), **(C)** nicotinamide riboside (NR), **(D)** N-acetylcysteine (NAC) or **(E)** mitoTempo. **(C, E)** Shown are mean ± SD, n = 3.

3.3.9 (R)-GNE-140 and BMS-986205 combination treatment leads to mitochondrial changes

Based on the phenotypic changes induced by the combination treatment (Fig. 12), further experiments were performed to analyze the cellular anatomy by transmission electron microscopy (TEM) (Fig. 20). Empty vector and KRAS^{G12V}/MYC cells were exposed to the indicated inhibitors for 48 hours, followed by analysis of cell anatomy, which revealed changes in the number and architecture of mitochondria (Fig. 20A). The combination treatment showed a significant increase of mitochondrial abundance in KRAS^{G12V}/MYC cells after manual counting of all mitochondria per cell for 10 cells (Fig. 20B). As manual counting is error prone, further quantification was performed using Mitotracker and TMRE, molecules that accumulate in mitochondria and emit fluorescence (Chazotte, 2011; Perry *et al.*, 2011). Flowcytometric analysis of mitochondria confirmed that combination treatment increases mitochondrial abundance by ~50% and ~300% in empty vector and KRAS^{G12V}/MYC cells, respectively (Fig. 20C, D). Manual quantification of mitochondrial areas from TEM images yielded variable results. While empty vector cells showed an increase of mitochondrial area after drug treatment, KRAS^{G12V}/MYC cells displayed reduced mitochondrial area (Fig. 20E).

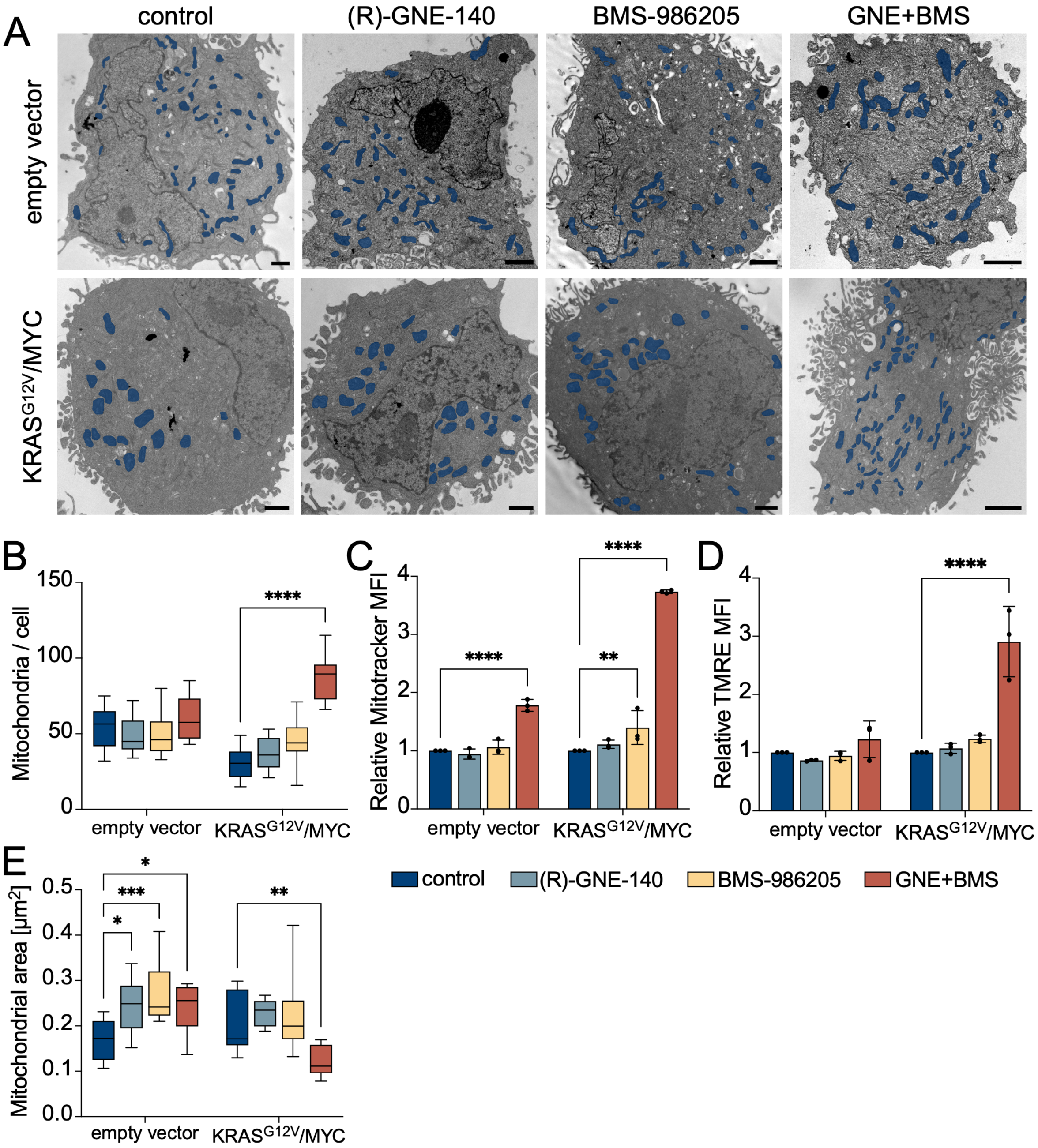

Fig. 20: Deregulation of mitochondrial abundance and area after (R)-GNE-140 and BMS-986205 combination treatment.
(A) 0.6 x 10^6 empty vector and 0.4 x 10^6 KRAS^{G12V}/MYC were seeded in 10 cm dishes and incubated for 1 day, followed by 48 hours of DMSO (0.135%), (R)-GNE-140 (7.5 µM) and BMS-986205 (6 µM) mono or combination treatment and transmission electron microscopic analysis. Mitochondria are highlighted (blue). Scale bar, 2 µm. **(C, F)** Image quantification of mitochondrial number and area per cell using FIJI image analysis software. Shown are boxplots, n = 10 cells. **(D, E)** Cells were treated as indicated for 48 hours, subsequently loaded with Mitotracker (200 nM) for 15 minutes or TMRE (200 nM) for 20 minutes followed by flowcytometric analysis for their median fluorescence intensity (MFI). Shown are mean ± SD, n = 3, $^*P \leq 0.05$, $^{**}P \leq 0.01$, $^{***}P \leq 0.001$, $^{****}P \leq 0.0001$, two-way ANOVA after Dunnett’s multiple comparisons test.

Closer examination of individual mitochondria revealed structural differences of cristae upon BMS-986205 treatment (Fig. 21). In addition, control and (R)-GNE-140 treated empty vector mitochondria appeared darker.

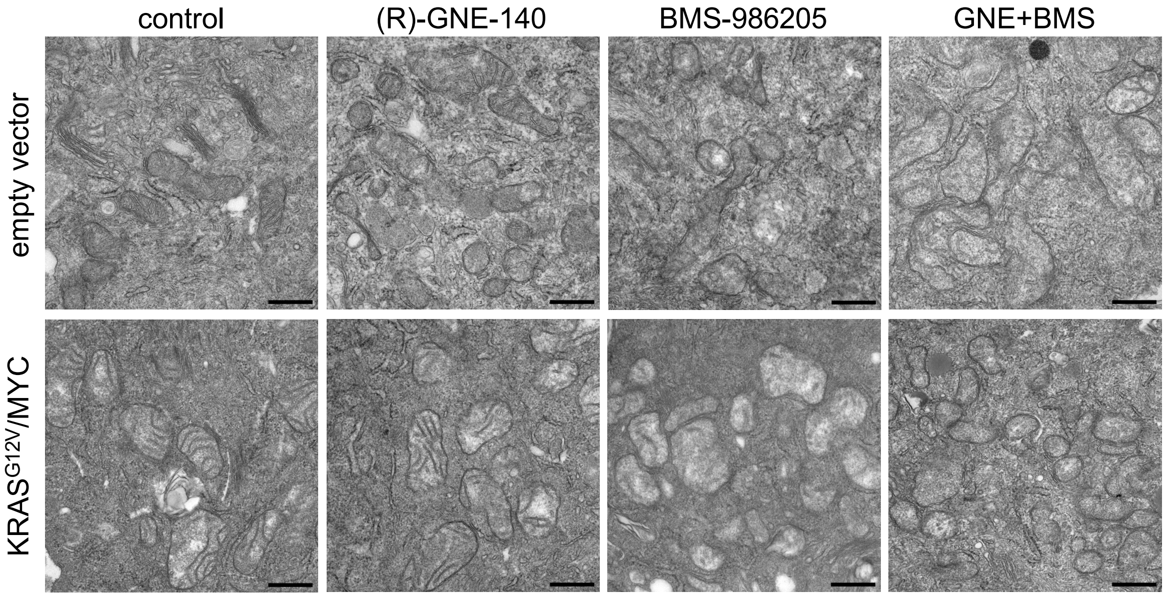

Fig. 21: Impaired folding of the inner mitochondrial membrane after BMS-986205 treatment.
0.6 x 10^6 empty vector and 0.4 x 10^6 KRAS^{G12V}/MYC were seeded in 10 cm dishes and incubated for 1 day, followed by 48 hours of DMSO (0.135%), (R)-GNE-140 (7.5 µM) and BMS-986205 (6 µM) mono or combination treatment and transmission electron microscopic analysis. Scale bar, 500 nm.

Taken together, these results show that BMS-986205 treatment results in defective folding of the inner mitochondrial membrane. In addition, the combination increased mitochondrial abundance, and a deregulation of mitochondrial area.

3.3.10 (R)-GNE-140 and BMS-986205 combination treatment simultaneously inhibits glycolysis and oxidative phosphorylation

As mitochondria are the key organelles of cellular energy metabolism, Seahorse metabolic flux analysis was used to obtain a comprehensive overview of the cellular energy metabolism. KRAS^{G12V}/MYC and empty vector cells were seeded in Seahorse 96-well plates and treated as described in section 2.3.14.

(R)-GNE-140 treatment significantly decreased the extracellular acidification rate (ECAR) (Fig. 22B, E, F) and increased the oxygen consumption rate (OCR) (Fig. 22A, C, D). BMS-986205 significantly decreased the OCR and increased the ECAR. Combination treatment significantly decreased the OCR and ECAR (Fig. 22A, B, C, D, E, F). As lactate excretion leads to an acidification of the cell-culture medium, we measured the effect of (R)-GNE-140 and BMS-986205 on the pH of supernatants from KRAS^{G12V}/MYC and control cells. While BMS-986205 led to an acidification of the medium, the addition of (R)-GNE-140 resulted in basification of the medium (Fig. 22G), which is in line with its known function as an LDH inhibitor (Pathria *et al.*, 2018; Serganova *et al.*, 2018). The energy map summarizes the previously described results (Fig. 22H). (R)-GNE-140 shifts the cells into an aerobic state of energy production, while BMS-986205 induces a shift to glycolytic energy production. The combination treatment shifts the cells into an energy quiescent state. In principle, both drugs had similar effects on empty vector and KRAS^{G12V}/MYC cells.

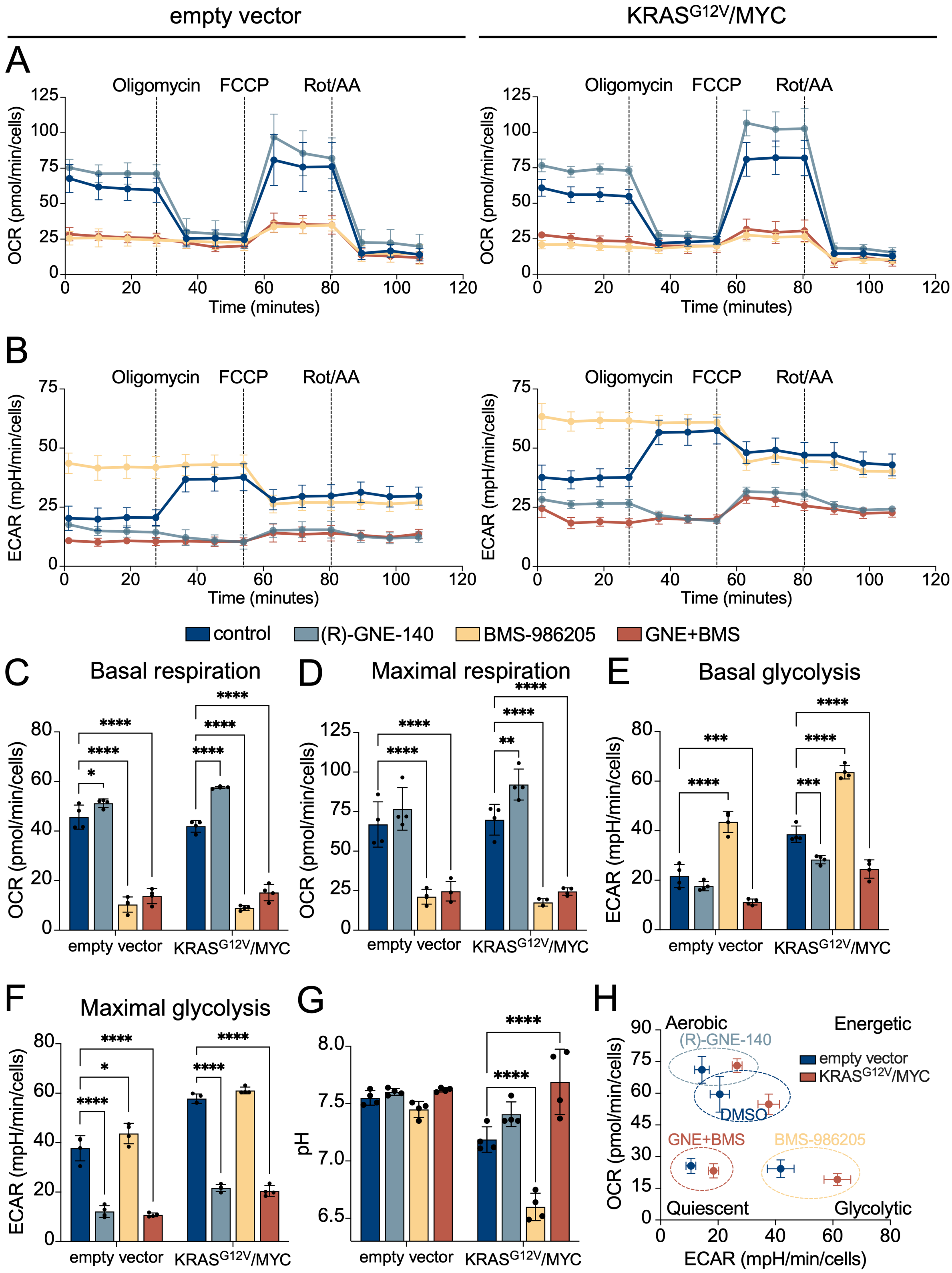

Fig. 22: Simultaneous inhibition of glycolysis and oxidative phosphorylation upon (R)-GNE-140 and BMS-986205 combination treatment.
To be continued on next slide.

(A) Seahorse metabolic flux analysis was performed using the MitoStress kit. Cells received DMSO (0.135%), (R)-GNE-140 (7.5 µM) and BMS-986205 (6 µM) mono or combination treatment for 4 hours followed by Seahorse analysis. Oligomycin (2 µM), FCCP (2 µM) and Rotenone/Antimycin A (1 µM) were injected into the wells at indicated timepoints. **(A)** Quantification of the oxygen consumption rate (OCR). **(B)** Quantification of the extracellular acidification rate (ECAR). **(C, D)** Quantification of basal and maximal respiration. **(E, F)** Quantification of basal and maximal glycolysis. **(H)** Energy map summarizing the Seahorse experiments and annotating the different treatments to metabolic states (Aerobic, Glycolytic, Energetic or Quiescent). Shown are mean ± SD, n = 4, *P ≤ 0.05, **P ≤ 0.01, ***P ≤ 0.001, ****P ≤ 0.0001, two-way ANOVA after Dunnett’s multiple comparisons test.

3.3.11 Targeted metabolomics reveals deregulation upon (R)-GNE-140 and BMS-986205 combination treatment

Targeted metabolomic analysis was performed for metabolites of central-carbon metabolism (glycolysis, pentose phosphate pathway and citric acid cycle), amines and nucleosides/tides. KRAS^{G12V}/MYC cells were exposed to (R)-GNE-140 and/or BMS-986205 and 4 hours later cell extracts were prepared and subjected to metabolomic analysis (Fig. 23A, B, C). The combination treatment induced significant and strong deregulation of 37 metabolites, while cells treated with (R)-GNE-140 or BMS-986205 showed deregulation of 8 and 17 metabolites, respectively. Cells treated with BMS-986205 (mono and in combination with (R)-GNE-140) showed a reduction of the important TCA molecules FAD and succinate. The combination treatment resulted in decreased levels of most of the investigated amines (Fig. 23D). In addition, a plethora of metabolites contributing to energy and redox homeostasis are decreased after (R)-GNE-140 and BMS-986205 combination treatment (Fig. 23E). The previously hypothesized energy stress upon combination treatment was verified by the observation of a ~40% reduction in ATP (Fig. 23F). Furthermore, pathway enrichment analysis of significant and strong decreased metabolites upon combination treatment showed the annotation of pathways related to energy production (TCA), nucleotide biosynthesis (pyrimidine and purine metabolism) as well as pathways contributing to redox homeostasis (glutathione metabolism, NAD metabolism).

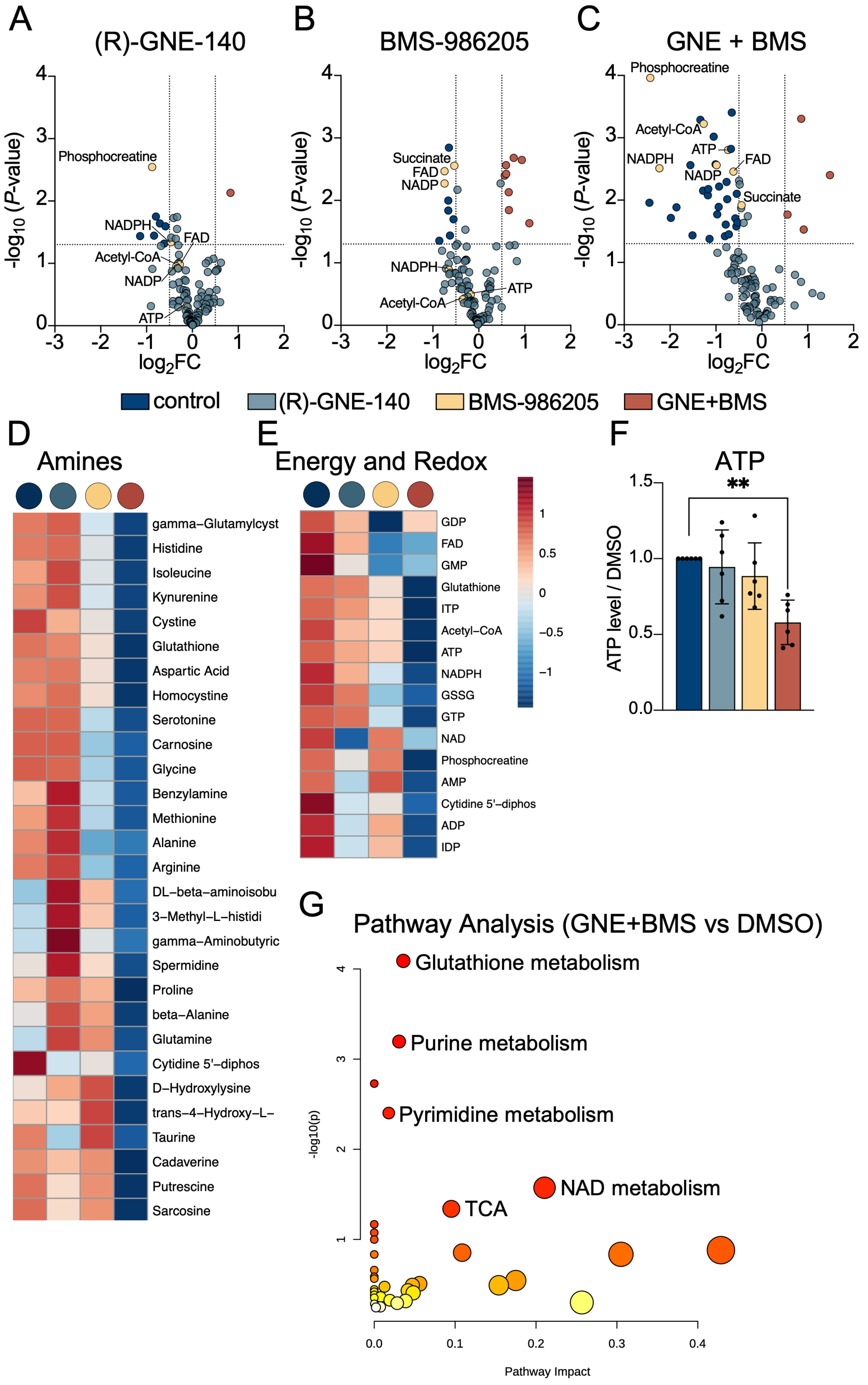
A
(R)-GNE-140
B
BMS-986205
C
GNE + BMS
-log10 (P-value)
log2FC
Phosphocreatine
NADPH
FAD
Acetyl-CoA
NADP
ATP
Succinate
control
(R)-GNE-140
BMS-986205
GNE+BMS
D
Amines
gamma–Glutamylcyst
Histidine
Isoleucine
Kynurenine
Cystine
Glutathione
Aspartic Acid
Homocystine
Serotonine
Carnosine
Glycine
Benzylamine
Methionine
Alanine
Arginine
DL–beta–aminoisobu
3–Methyl–L–histidi
gamma–Aminobutyric
Spermidine
Proline
beta–Alanine
Glutamine
Cytidine 5'–diphos
D–Hydroxylysine
trans–4–Hydroxy–L–
Taurine
Cadaverine
Putrescine
Sarcosine
E
Energy and Redox
GDP
FAD
GMP
Glutathione
ITP
Acetyl–CoA
ATP
NADPH
GSSG
GTP
NAD
Phosphocreatine
AMP
Cytidine 5'–diphos
ADP
IDP
1
0.5
0
−0.5
−1
F
ATP
**
ATP level / DMSO
1.5
1.0
0.5
0.0
G
Pathway Analysis (GNE+BMS vs DMSO)
Glutathione metabolism
Purine metabolism
Pyrimidine metabolism
NAD metabolism
TCA
-log10(p)
Pathway Impact
0.0
0.1
0.2
0.3
0.4

Fig. 23: Effects of (R)-GNE-140 and BMS-986205 on metabolic pathways.
1 x 10^6 KRAS^{G12V}/MYC cells were seeded in 10 cm dishes and incubated for 1 day, followed by DMSO (0.135%), (R)-GNE-140 (7.5 µM) and BMS-986205 (6 µM) mono and combination treatment for 4 hours and subjected to metabolomic analysis. Peak-intensities were normalized to internal standards and the protein concentration of each sample. Volcano plots of the drug induced metabolic changes after **(A)** (R)-GNE-140, **(B)** BMS-986205 and **(C)** (R)-GNE-140 and BMS-986205 treatment, n = 6. Statistical analysis was performed using two-sided, paired t-test. Relative changes of metabolite abundance were compared to DMSO treated cells. Cut-offs: $P \leq 0.05$; $\log_2$ fold-change < -0.5, > 0.5. **(D, E)** Heatmaps depicting the average metabolite peak-intensities of 6 replicates. Abundance of metabolites is shown as a red to blue color spectrum (high abundance - low abundance). **(F)** Relative ATP levels were calculated by normalizing the peak-intensities of each replicate to its respective DMSO replicate. Shown are mean ± SD, n = 6, $^{**}P \leq 0.01$, one-way ANOVA after Dunnett's multiple comparisons test. **(G)** Pathway enrichment analysis of downregulated metabolites comparing (R)-GNE-140 and BMS-986205 combination to DMSO treated cells, Cut-offs: $P \leq 0.05$; $\log_2$ fold-change < -0.5, > 0.5. (D, E, G) Figures were created using Metaboanalyst 5.0.

3.3.12 (R)-GNE-140 and BMS-986205 induced energy stress is sensed on a molecular level

Cellular energy depletion is sensed and counteracted by the AMPK-mTOR axis through mechanisms involving the dephosphorylation of eukaryotic translation initiation factor 4E-binding protein 1 (4E-BP1) and phosphorylation of acetyl-CoA carboxylase (ACC) (Fig. 24A) (Garcia and Shaw, 2017; Wu and Storey, 2021). Detection of AMPK-mTOR signaling pathway proteins and their phosphorylation status was facilitated by Western blotting four hours after drug treatment (Fig. 24B). No significant changes of mTOR and its phosphorylation site S2448 were detected, while phosphorylation of 4E-BP1 at S37/46 was highly variable (Fig. 24C, D). Overall, the combination treatment led to a pronounced decrease of 4E-BP1 Thr-37/46 and Ser-65 in empty vector and KRAS^{G12V}/MYC cells (Fig. 24B, D, E). In addition, increased phosphorylation of ACC at Ser-79 was detected in in empty vector and KRAS^{G12V}/MYC cells upon combination treatment (Fig. 24F).

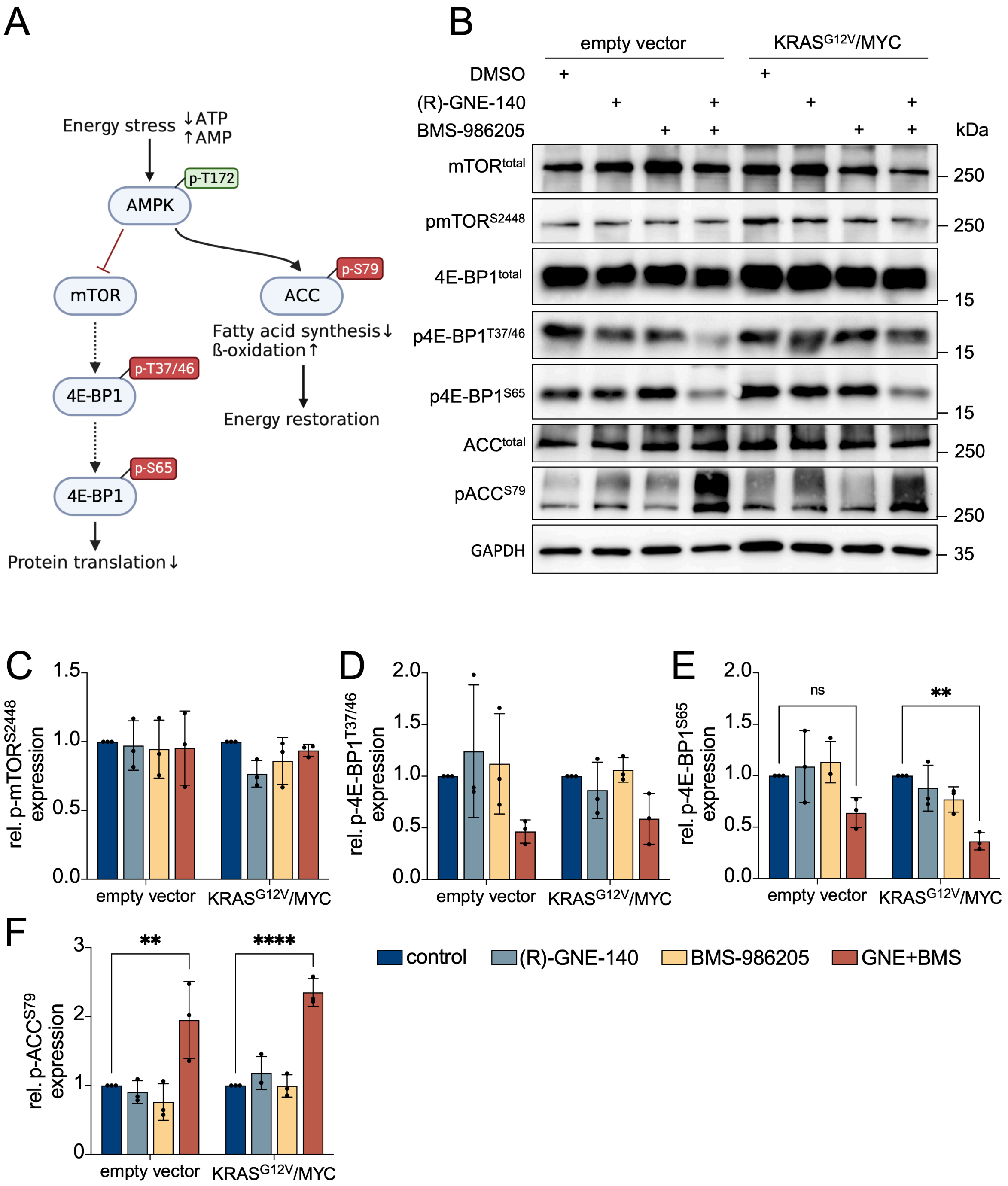

Fig. 24: Activation of AMPK signaling after (R)-GNE-140 and BMS-986205 combination treatment.

(A) Schematic depiction of signaling pathways altered by the metabolic status. **(B)** Empty vector and KRAS^{G12V}/MYC cells were treated with DMSO (0.135%) or (R)-GNE-140 (7.5 µM) and BMS-986205 (6 µM) combination treatment for 4 hours followed by protein detection using Western blotting. **(C, D, E, F)** Western blot quantification of indicated proteins using FIJI. Shown are mean ± SD, n = 4, *P ≤ 0.05, **P ≤ 0.01, ***P ≤ 0.001, ****P ≤ 0.0001, two-way ANOVA after Dunnett's multiple comparisons test.

3.3.13 Target specificity of (R)-GNE-140 and BMS-986205

3.3.13.1 Other inhibitors for LDHA/B and IDO1

(R)-GNE-140 and BMS-986205 inhibit LDHA/B and IDO1, respectively. If the previously described effects of the combination treatment are based on simultaneous inhibition of LDHA/B and IDO1, the use of other inhibitors targeting LDHA/B and IDO1 should be able to recapitulate the effects observed after (R)-GNE-140 and BMS-986205 combination treatment. GSK-2837808A and Epacadostat are potent inhibitors of LDHA/B and IDO1, respectively. After exposure of KRAS^{G12V}/MYC cells to different drug combinations (Fig. 25A) significant synergistic cytotoxicity was only observed for (R)-GNE-140 and BMS-986205 combination treatment (Fig. 25B, C).

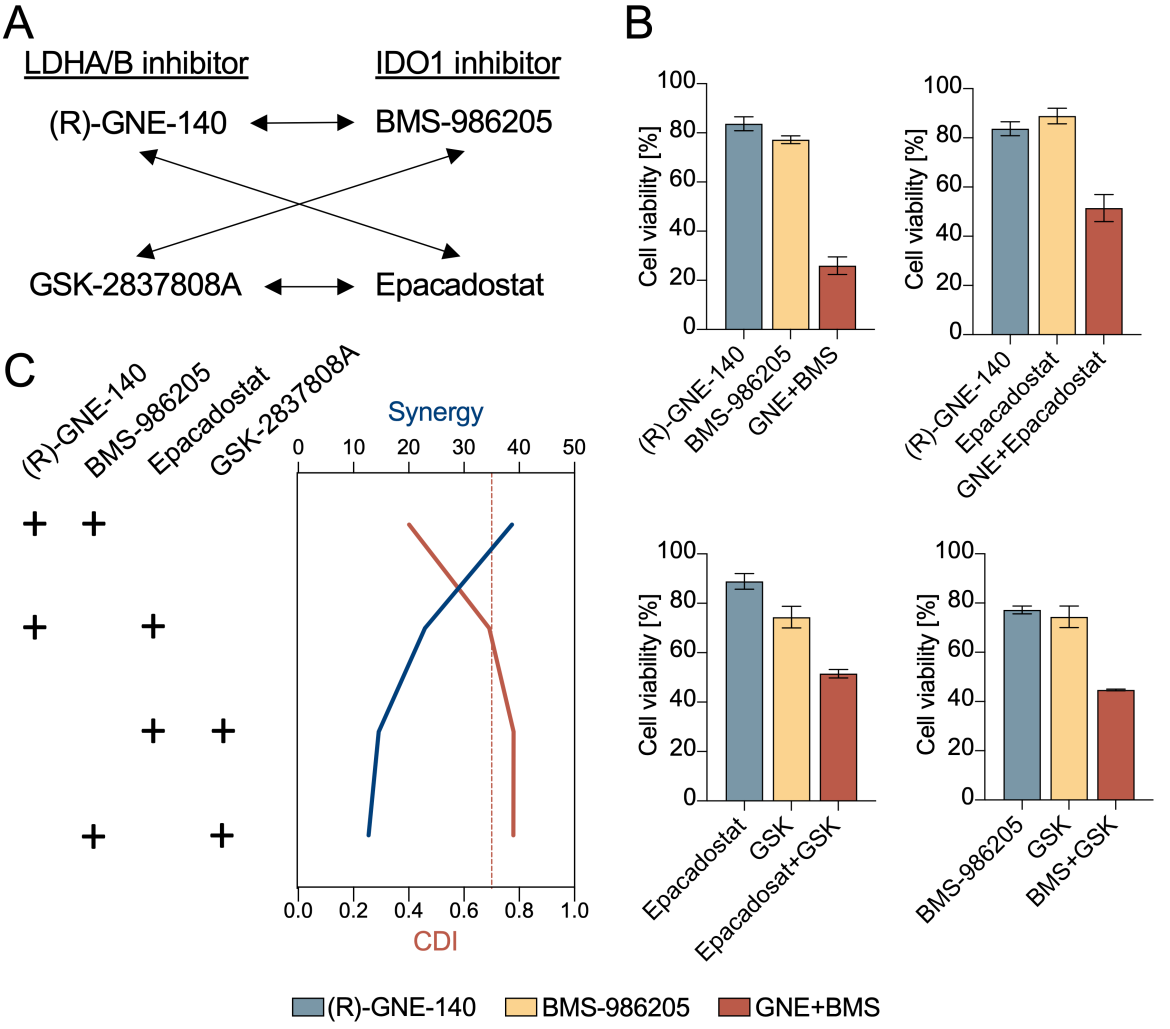

Fig. 25: Other inhibitors targeting LDHA/B and IDO1 cannot recapitulate the effects of (R)-GNE-140 and BMS-986205 combination treatment.
To be continued on next page.

(A) Schematic representation of the inhibitor combinations tested. **(B)** 1500 KRAS^{G12V}/MYC cells were seeded in 96-well plates and incubated for 1 day, followed by treatment the depicted combinations of (R)-GNE-140 (7.5 µM), BMS-986205 (6 µM), GSK-2837808A (35 µM) and Epacadostat (40 µM). Shown are mean ± SD, n = 3. **(C)** Synergy levels are depicted in %-points and coefficient of drug interaction (CDI), as previously described (2.5). The red line marks the significance threshold of ≤ 0.7 CDI.

3.3.13.2 siRNA mediated knockdown of LDHA/B and IDO1

If the synergistic response to the (R)-GNE-140 and BMS-986205 combination treatment in KRAS^{G12V}/MYC cells is due to interference with LDHA/B and IDO1 protein function, simultaneous siRNA-mediated knockdown of LDHA/B and IDO1 should recapitulate the effects of the combination treatment. Knockdown of LDHA/B and IDO1 was confirmed by qPCR (Fig. 26A) and Western blotting (Fig. 26B). However, residual LDHA/B protein was detected. After triple siRNA combination, LDHA protein levels increased. Simultaneous LDHA/B and IDO1 knockdown could not recapitulate the effects of (R)-GNE-140 and BMS-986205 combination treatment on the level of cell viability (Fig. 26C).

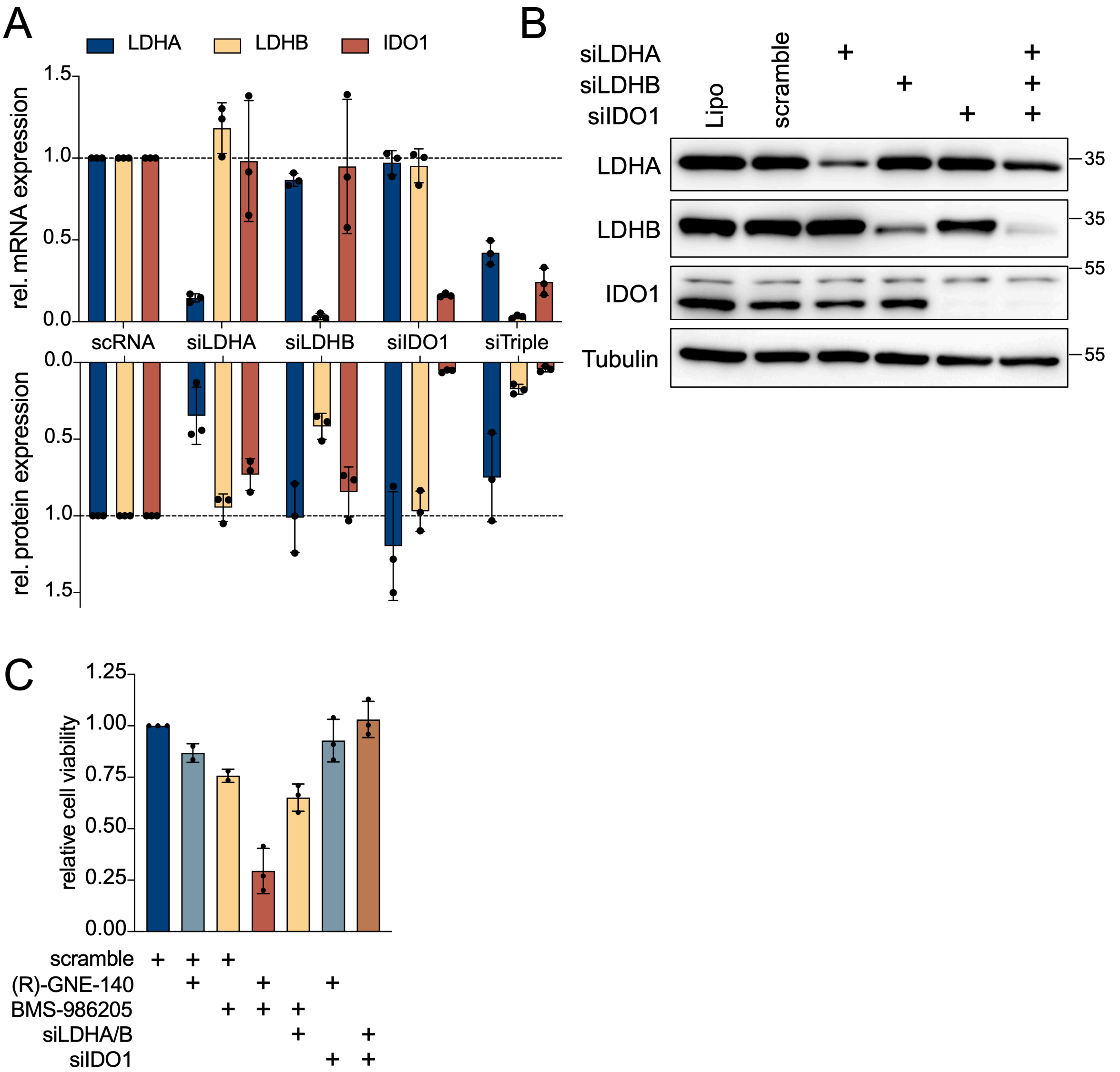

Fig. 26: siRNA-mediated knockdown of (R)-GNE-140 and BMS-986205 targets cannot recapitulate the drug effects.
0.5 x 10^5 KRAS^{G12V}/MYC were seeded in 5 cm dishes and incubated for 1 day, followed by double siRNA transfection (5 nM/siRNA) for 48 hours each. **(A)** mRNA and protein expression levels relative to a scramble siRNA control. **(B)** Protein expression analysis via Western blotting. **(C)** Cell-viability analysis of cells which received simultaneous double siRNA transfection and/or (R)-GNE-140 (7.5 µM) and BMS-986205 (6 µM) mono treatment for 48 hours after each transfection.

To summarize, other inhibitors targeting LDHA/B and IDO1 or the use of siRNAs were not able to recapitulate the effects of (R)-GNE-140 and BMS-986205.

3.4 Translation of (R)-GNE-140 and BMS-986205 combination treatment to other well-established cancer cell lines

3.4.1 (R)-GNE-140 and BMS-986205 combination treatment exerts synergistic cytotoxicity against a variety of established cell lines

Are other genetically different cell lines affected by (R)-GNE-140 and BMS-986205? To answer this question, eleven cell lines were subjected to (R)-GNE-140 and BMS-986205 combination treatment and drug cytotoxicity was analyzed. According to their response to the combination treatment, the cell lines were divided into 3 groups (Fig. 27A). 8 cell lines showed a significant synergistic response (high/medium), while 3 cell lines showed no significant synergistic response (low) towards the combination treatment. The overall type of response was highly heterogeneous (Fig. 27B). Changes in the pH levels following mono or combination treatments were similar to KRAS^{G12V}/MYC cells (highlighted with a star) (Fig. 27C)

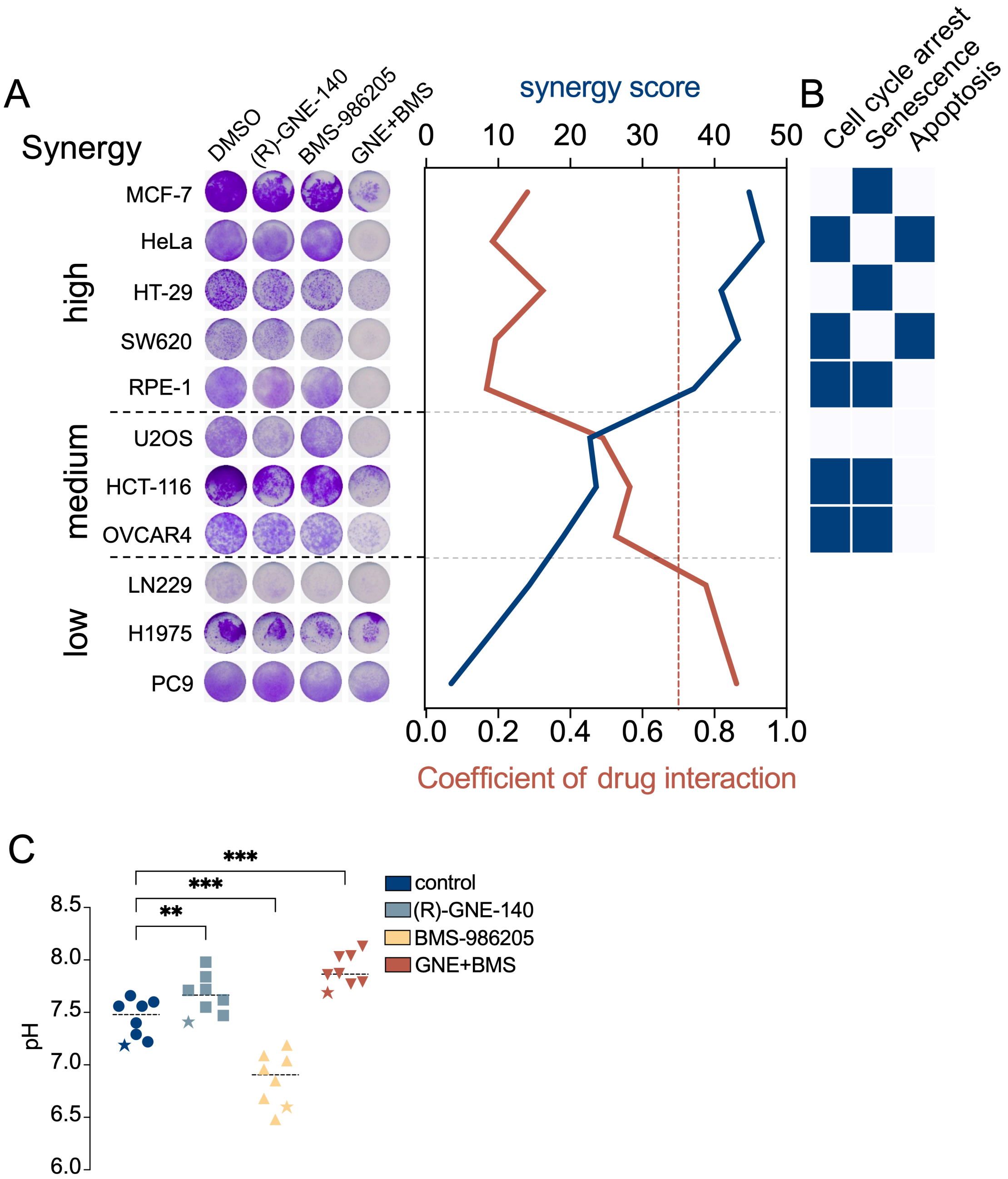

Fig. 27: (R)-GNE-140 and BMS-986205 achieve synergy in a variety of cell lines.
(A) Representative crystal violet images of indicated cell lines treated with DMSO or (R)-GNE-140 and BMS-986205 combination treatment. Treatment specifications can be found in section 2.3.16. Synergy levels are depicted as synergy score in %-points and coefficient of drug interaction (CDI), as previously described. The red line marks the significance threshold of ≦ 0.7. Cell lines were grouped into low, medium and high according to their level of synergistic response. Shown are mean, n = 3 **(B)** Overview of the cellular responses analyzed in the following experiments (Fig. 27, 28, 29). **(C)** pH measurements of cell lines of medium and high synergy groups. pH measurements of KRAS^{G12V}/MYC cells are highlighted with a star. Shown is the mean pH of all cell after indicated conditions lines, **P ≤ 0.01, ***P ≤ 0.001, two-way ANOVA after Dunnett’s multiple comparisons test.

3.4.2 (R)-GNE-140 and BMS-986205 combination treatment induces senescence in multiple well-established cell lines

To investigate the induction of senescence in the medium and high synergy groups of (Fig. 27A), cells were treated with (R)-GNE-140 and BMS-986205 mono- or combination treatment for 4 and 6 days, followed by SA-ß-gal activity analysis (Fig. 28). Brightfield images revealed increased SA-ß-gal activity for MCF-7, HT-29, RPE-1, HCT-116 and OVCAR-4 cell lines after 6 days of combination treatment.

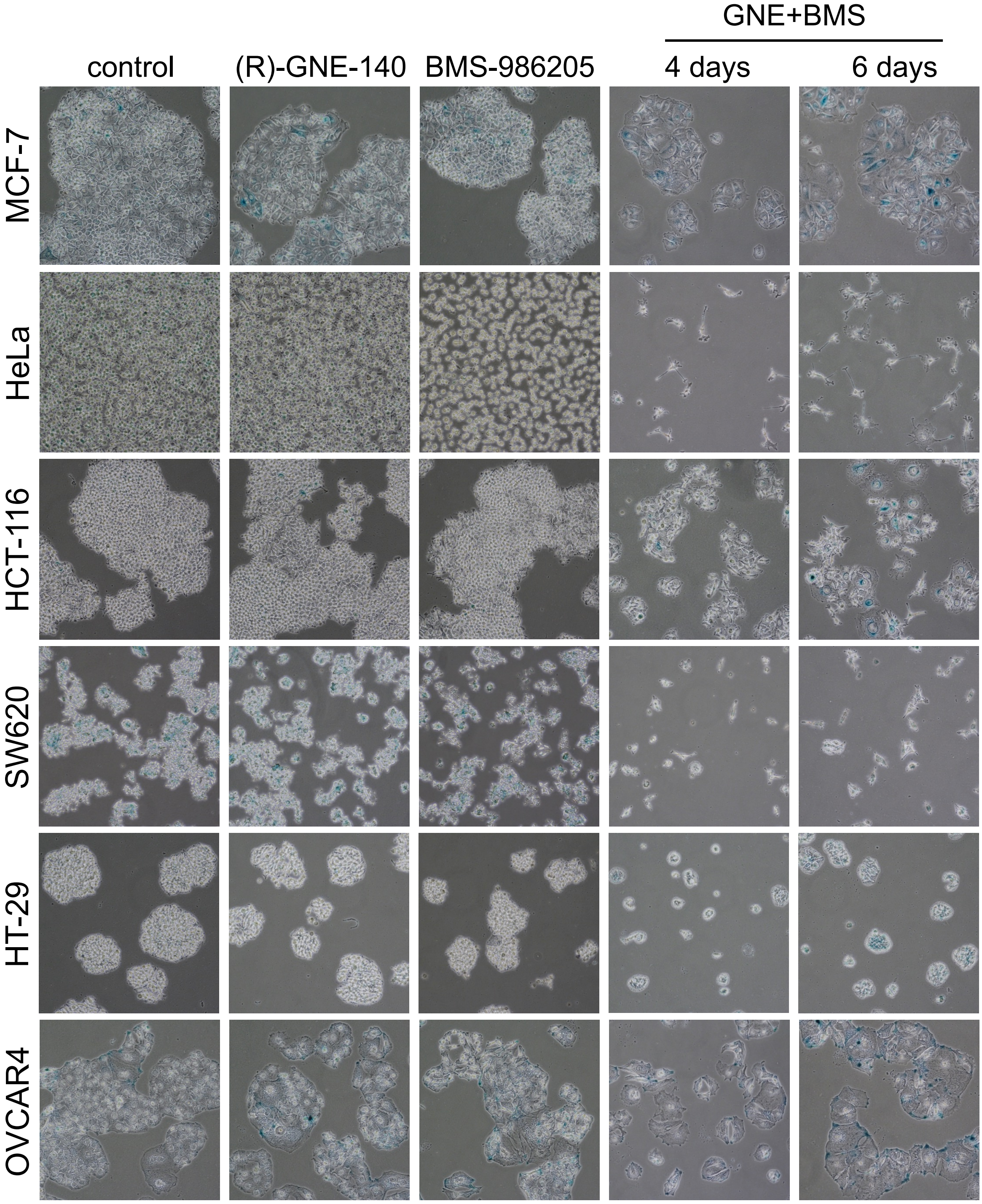

Fig. 28: Increased ß-galactosidase activity in multiple cell lines.
Indicated cell lines received DMSO, (R)-GNE-140 and BMS-986205 mono or combination treatment for 96 hours followed by ß-galactosidase activity assay. Treatment specifications can be found in section 2.3.16, n = 3.

3.4.3 (R)-GNE-140 and BMS-986205 combination treatment induces cell cycle arrest in several cell lines

For analysis cell cycle distribution, cells were treated with (R)-GNE-140 and BMS-986205 mono- or combination treatment, stained with propidium iodide and subsequently analyzed using flowcytometry (Fig. 29). Flowcytometric analysis revealed G2/M phase accumulation of HeLa, HCT-116, SW620, RPE-1 and OVCAR-4 cell lines upon combination treatment.

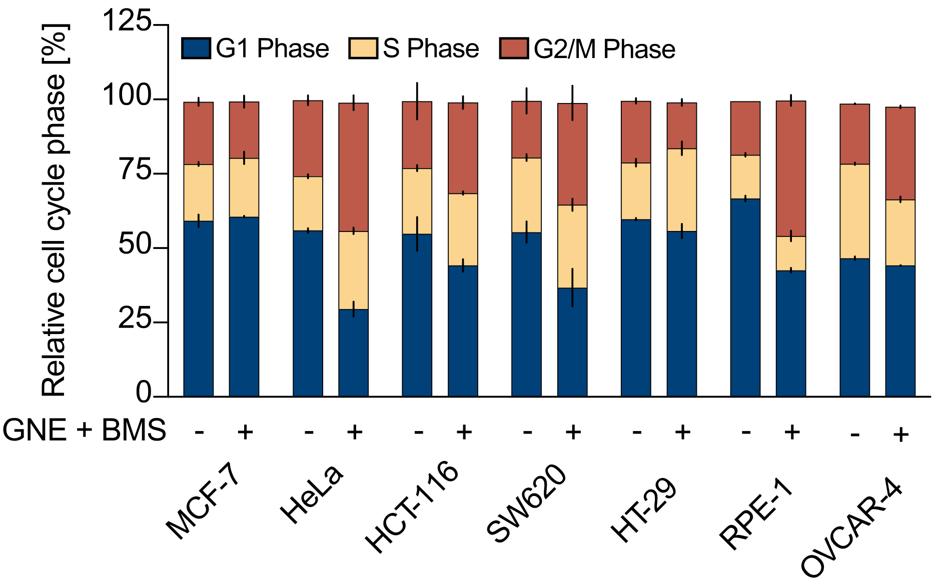

Fig. 29: Cell cycle arrest after (R)-GNE-140 and BMS-986205 combination treatment in multiple cell lines.
Indicated cell lines received DMSO or (R)-GNE-140 and BMS-986205 combination treatment for 96 hours. Treatment specifications can be found in section 2.3.16. Cell cycle distribution was analyzed using flowcytometry after propidium iodide staining, n = 3.

3.4.4 (R)-GNE-140 and BMS-986205 combination treatment induces apoptosis in HeLa and SW620 cell lines

HeLa and SW620 cell lines responded with increased numbers of floating cells after combination treatment, which may indicate the induction of apoptosis. To test for the induction of apoptosis, the different tumor cells were treated with (R)-GNE-140 and/or BMS-986205, followed by detection of cleaved caspase 3 levels by Western blotting (Fig. 30A, B). Among the panel of tested cell lines, only HeLa and SW620 showed significantly increased levels of cleaved caspase 3, which was specific to the (R)-GNE-140 and BMS-986205 combination treatment (Fig. 30C).

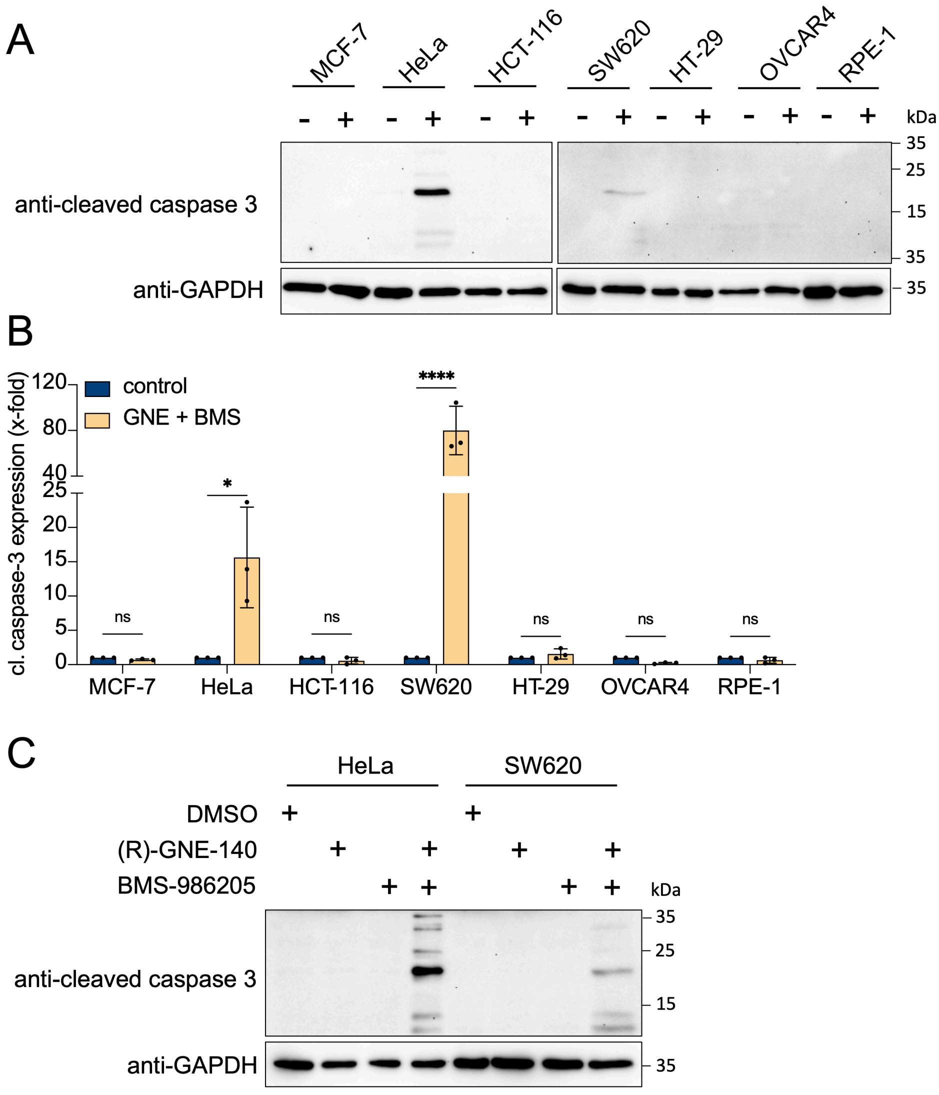

Fig. 30: (R)-GNE-140 and BMS-986205 treatment induces apoptosis in specific cell lines.
Indicated cell lines received DMSO or (R)-GNE-140 and BMS-986205 combination treatment for 96 hours. Treatment specifications can be found in section 2.3.16. Extracts were generated and analyzed for cleaved caspase 3 protein levels. **(A)** Detection of cleaved caspase 3 levels via Western blotting. **(B)** Quantification of cleaved caspase 3 expression levels using FIJI image analysis software. Shown are mean ± SD, n = 3, $^{*}P \leq 0.05$, $^{****}P \leq 0.0001$, two-way ANOVA after Šídák's multiple comparisons test. **(C)** HeLa and SW620 cell lines received DMSO or (R)-GNE-140 and BMS-986205 mono or combination treatment for 96 hours, followed by detection of cleaved caspase 3 using Western blotting.

In summary, these data show that inhibition of cell proliferation by (R)-GNE-140 and BMS-986205 is observed in a variety of different cancer cell lines of different origin.

Interestingly, this comparative analysis also revealed three cell lines that were refractory to this drug combination, excluding the occurrence of general cytotoxicity. The cellular effects were heterogeneous and the causes of this differential behavior will be the subject of future investigation.

4 Discussion

4.1 Generation of a suitable ovarian cancer cell line

Despite some progress for the treatment of individual cancer types such as acute childhood leukaemia and the avenue of new treatment options including checkpoint inhibitors (Borella *et al.*, 2020; Walsh, Sundar and Lim, 2023), cancer remains a major challenge to human health and continues to be the second leading cause of death in the United States. This work focuses on the most prevalent ovarian cancer subtype HGSOC, which ranks fifth in cancer deaths among women worldwide (Bell *et al.*, 2011; Lisio *et al.*, 2019). Cancer research benefits from highly defined models, ranging from well-characterized tumor cell lines to organoids and animal models. Although each of these model systems has clear limitations, as discussed elsewhere (Hasan, Ohman and Dinulescu, 2015; Warren *et al.*, 2015; Katt *et al.*, 2016; Bose, Clevers and Shen, 2021; Antunes *et al.*, 2022), well-characterized cell models can be a valuable tool for preclinical research (Gillet, Varma and Gottesman, 2013).

HGSOC is a molecularly heterogenous disease with diverse clinical presentation but a simple mutational profile compared to other cancers (Bell *et al.*, 2011). Since prolonged culture of well-established cellular model system leads to genetic and transcriptional evolution, which has been shown to alter drug response (Torsvik *et al.*, 2014; Ben-David *et al.*, 2018), I developed a new genetically highly defined cancer cell line for HGSOC research. As a starting point, fallopian tube secretory epithelial cells were chosen as it is believed that HGSOC develops from the fallopian tubes (Karst, Levanon and Drapkin, 2011; Erickson, Conner and Landen, 2013). Although mutant KRAS is underrepresented in HGSOC (<1% of all cases), KRAS was used for the generation of cancer cells for two reasons (Bell *et al.*, 2011): First, mutant KRAS is known to transform healthy cells into cancer cells (Der and Cooper, 1983; Parada and Weinberg, 1983). Secondly, PI3K/RAS signaling is altered in 45% of HGSOC patients and is associated with cancer proliferation and reduced patient survival (Bell *et al.*, 2011). MYC was chosen because it is most frequently amplified in ovarian cancer (McAnulty and DiFeo, 2020). The resulting KRAS^{G12V}/MYC cancer cells exhibit many hallmarks of cancer cells, as evidenced by their high proliferation rate, gene expression pattern, and their ability to migrate and invade in transwell assays. Furthermore, the KRAS^{G12V}/MYC cancer cells developed a glycolytic phenotype while maintaining their rate of oxidative phosphorylation.

4.2 Targeting of metabolic pathways as a treatment option for cancer cells

Depending on the tumor type, novel therapeutic concepts may involve immunological approaches, such as checkpoint inhibitors (used to treat melanomas and non-small cell lung cancer, among others), differentiation therapy (e.g. acute promyelocytic leukaemia), or targeted therapy (e.g. PARP inhibitors for mutant BRCA patients) that specifically interferes with molecular alterations or pathways that drive cancer growth and survival (Gocek and Marcinkowska, 2011; Galluzzi *et al.*, 2015; Borella *et al.*, 2020; Curtin and Szabo, 2020).

In addition, cancer cells present with a plethora of metabolic vulnerabilities which can be exploited for selective cancer therapies. For example, the clinically approved drugs Ivosidenib and Enasidenib inhibit mutant IDH1/2 enzymes, which produce the oncometabolite 2-hydroxyglutarate (2-HG) to promote AML development (Stein *et al.*, 2017; Roboz *et al.*, 2020; Cerchione *et al.*, 2021). Metabolic drugs currently under investigation in clinical trials are CB-839, TVB-2640 and AZD-3965 among many others. The glutaminase inhibitor CB-839 is used for leakeamia, colorectal and breast cancer therapy as it disrupts the conversion of glutamate to glutamine, an amino acid which is essential for the growth and survival of many cancers (Wise and Thompson, 2010; Gross *et al.*, 2014). The fatty acid synthase (FASN) inhibitor TVB-2640 limits the production of lipids, which is particularly important for cancer cell proliferation (Falchook *et al.*, 2021). Acidification of the TME is highly beneficial for cancer cell survival, as lactate suppresses immune cell activity and serves as a fuel for the growth of cancer cells (Boedtkjer and Pedersen, 2020). Therefore, AZD-3965 is currently being investigated for its ability to suppress lactate export by inhibiting monocarboxylate transporter 1 (MCT1) (Curtis *et al.*, 2017).

The development of chemotherapeutic resistance may also create targetable metabolic vulnerabilities (Obrist *et al.*, 2018; Gremke *et al.*, 2020). In NSCLC, mTOR-mediated drug resistance has been shown to disrupt autophagy, impairing metabolic homeostasis and increasing sensitivity to additional metabolic perturbation by 2-DG or DCA (Gremke *et al.*, 2020). Furthermore, cisplatin resistant cancers are more sensitive to glutamine starvation, thus creating an opportunity for selective cancer therapy by interfering with glutamine metabolism (Obrist *et al.*, 2018).

These and many more studies represent a rational for the development of novel metabolic therapies for cancer treatment. The present study however, aims to achieve synthetic lethality through inhibition of distinct metabolic pathways using two different metabolic inhibitors. The concept of synthetic lethality is based on genetic ablation, where interference with only one gene does not decrease cellular viability, whereas interference with two genes results in cell death (Setton *et al.*, 2021). The primary example for synthetic lethal approaches in the clinics is the use of PARP-inhibitors in patients that already show HR-deficiency (Helleday, 2011). Regarding synthetic lethal metabolic perturbation, it has been demonstrated that sublethal concentrations of the oxidative phosphorylation inhibitor B87 and dimethyl alpha-ketoglutarate (DMKG) achieved synergistic cytotoxicity in combination (Sica *et al.*, 2019). Synergy is achieved through DMKG mediated transcriptional reprogramming, which decreased glycolysis. Thus, combinatorial treatment with B87 and DMKG led to an energetic catastrophe which resulted in the synthetic lethality of cancer cells.

Given the general lack of synthetic lethal metabolic therapies, this study is aiming to identify novel metabolic vulnerabilities of ovarian cancer cells based on the concept of synthetic lethality.

4.3 Energy stress-triggered induction of senescence by (R)-GNE-140 and BMS-986205 combination treatment

The healthy cell versus cancer cell model allowed the identification of a synergistic combination consisting of the drugs (R)-GNE-140 and BMS-986205, which exhibited selectivity towards the KRAS^{G12V}/MYC cancer cells. Here I present a hypothetical model illustrating the effects of (R)-GNE-140 and BMS-986205 combination treatment based on data generated in this study and in light of the current literature linking energy stress to senescence.

4.3.1 Metabolic deregulation after (R)-GNE-140 and BMS-986205 combination treatment

This study shows strong metabolic deregulation in tumor cells upon co-administration of (R)-GNE-140 and BMS-986205. It is well known that (R)-GNE-140 inhibits lactate fermentation, and thereby glycolysis, through inhibition of LDHA/B (Boudreau *et al.*, 2016; Pathria *et al.*, 2018; Ždralević *et al.*, 2018), while BMS-986205 interferes with tryptophan catabolism through inhibition of IDO1 (Siu *et al.*, 2017). Seahorse metabolic flux analyses unexpectedly revealed inhibition of oxidative phosphorylation upon BMS-986205 treatment. Interestingly, there are no data available for BMS-986205 to support its potent inhibition of oxidative phosphorylation. This is also clinically relevant, as this compound is currently being tested in several Phase II clinical trials (Siu *et al.*, 2017; Luke *et al.*, 2019; Bristol-Myers Squibb, 2022).

Targeted metabolomic profiling revealed a decrease in succinate and FAD following BMS-986205 treatment. Succinate and FAD are used to generate fumarate and $FADH_2$ by the enzyme succinate dehydrogenase (SDH), also known as complex II of the ETC (Cecchini, 2003). Reduced levels of FAD and succinate may result in decreased complex II, providing an explanation for the inhibition of oxidative phosphorylation, which is under further investigation.

Another plausible link between inhibition of tryptophan catabolism and oxidative phosphorylation is the *de novo* synthesis of NAD^+ through the kynurenine pathway downstream of IDO1 (Kurnasov *et al.*, 2003). NAD^+ is an electron acceptor and an important component of the TCA cycle (Xiao *et al.*, 2018). Therefore, IDO1 inhibition could lead to a reduction in NAD^+ levels below the critical threshold required for proper TCA cycling. This would reduce the level of NADH, which similar to $FADH_2$, is a major electron donor for oxidative phosphorylation (Nolfi-Donegan, Braganza and Shiva, 2020).

The inhibitory effects of BMS-986205 on the respiratory chain could be attributable to several other effects. One obvious mechanism is directly related to the lack of folding of the inner mitochondrial membrane (Fig. 21). This inevitably leads to a reduction in the surface area available to the components of the respiratory chain. What is the molecular mechanism that mediates the dysfunctional organization of the inner mitochondrial membrane? Candidate proteins responsible for the effects of BMS-986205 on mitochondrial architecture include dynamin-related protein 1 (DRP1), mitofusins (MFN1 and MFN2), components of the cristae organizing system (MICOS) and membrane curvature-sensing proteins (van der Bliek, Shen and Kawajiri, 2013; Kozjak-Pavlovic, 2017). It will therefore be important in future studies to identify the additional target(s) mediating the mitochondrial effects of BMS-986205. As targeting of LDH and IDO1 by other inhibitors and siRNAs failed to recapitulate the potent effects of (R)-GNE-140 and BMS-986205, it is fair to assume that the BMS-986205-dependent effects are also due to the disruption of mitochondrial architecture.

Despite these severe effects, cells survive BMS-986205 mediated inhibition of oxidative phosphorylation by compensatory up-regulation of glycolysis. This makes the cells particularly sensitive to glycolysis inhibition as demonstrated in this study. The combination treatment specific effects on cell survival can thus be attributed to the decrease of ATP and the resulting energy stress, as comprehensively shown by metabolomic analysis and the activation of energy stress-sensing signaling pathways.

In this context, combination treatment-induced energy stress led to activation of AMPK, marked by dephosphorylation of 4E-BP1 at Thr-37/46 and Ser-65 and phosphorylation of acetyl-CoA carboxylase (ACC) at Ser-79. Dephosphorylation of 4E-BP1 is a direct consequence of AMPK-mediated mTOR inhibition, leading to a halt in protein translation to conserve energy (Thomson, Fick and Gordon, 2008). Phosphorylation of ACC induces a switch from energy-consuming fatty acid synthesis to energy-producing fatty acid ß-oxidation (M. Lee *et al.*, 2018; Lally *et al.*, 2019). By restoring ATP levels - at least to a level that allows survival - AMPK activation attempts to counteract the effects of the combination treatment. Another compensatory mechanism involves AMPK-mediated mitochondrial biogenesis through PGC1α expression and direct activation of PGC1α by phosphorylation (Wu *et al.*, 1999; Jäger *et al.*, 2007; Settembre *et al.*, 2013). PGC1α stimulates the expression of key mitochondrial proteins resulting in the formation of new mitochondria (Lin *et al.*, 2002; Herzig and Shaw, 2018). Combination treatment significantly increased the number of mitochondria per cell, indicating activation of mitochondrial biogenesis pathways. At least in KRAS^{G12V}/MYC cancer cells, although an increased number of mitochondria was detected, a significant decrease of mitochondrial areas was noticed. This indicates the activity of mitochondrial fission. Similar to mitochondrial biogenesis, mitochondrial fission is also governed by AMPK. AMPK-mediated phosphorylation of the mitochondrial fission factor (MFF) leads to the recruitment of dynamin-like protein 1 (DRP1) to the outer mitochondrial membrane, inducing mitochondria constriction and separation (Smirnova *et al.*, 2001; Otera *et al.*, 2010; Ducommun *et al.*, 2015; Herzig and Shaw, 2018). Several studies have reported AMPK-mediated mitochondrial fission as a response to energy stress upon ETC inhibition (Toyama *et al.*, 2016; Trefts and Shaw, 2021). These studies may explain the observed mitochondrial phenotype induced by (R)-GNE-140 and BMS-986205 combination treatment, however, specific analysis of respective pathways must be conducted to report the underlying mechanisms.

In addition, pathway analysis of the significantly reduced metabolite levels upon combination treatment indicated a deregulation of redox homeostasis (glutathione and NAD metabolism), potentially responsible for the impairment of TCA resulting in inhibition of oxidative phosphorylation (Xiao *et al.*, 2018; Xu *et al.*, 2020). Since glutathione metabolism constitutes one of the cells most efficient ROS scavenging systems, impairment is likely to contribute to the 8-fold increase of ROS, which was detected upon combination treatment (Armstrong *et al.*, 2002).

Another indicator of severe metabolic perturbation, which was specifically detected after combining (R)-GNE-140 and BMS-986205, is the decrease in acetyl-CoA. Acetyl-CoA is considered to be one of the most import metabolic intermediates due to its pleiotropic functions in carbon metabolism, energy production, protein acetylation and more (Shi and Tu, 2015). The role of acetyl-CoA as a source for post-translational acetylation of proteins underscores its importance. Numerous studies have shown that enzymatic or non-enzymatic acetylation regulates the stability, localization and activity of glycolytic enzymes (Choudhary *et al.*, 2009; Li, *et al.*, 2019). For example, acetylation decreases the activity of GLUT1, HK and LDHA but increases the activity of GAPDH and PGK1 (Zhao *et al.*, 2013; Hitosugi and Chen, 2014; Bond *et al.*, 2017; Prakasam *et al.*, 2018; Tamura *et al.*, 2021). The rate of glycolysis in turn regulates histone acetylation, thereby shaping the cells chromatin architecture and transcriptional profile (Cluntun *et al.*, 2015).

In summary, (R)-GNE-140 and BMS-986205 mono treatment inhibits glycolysis and oxidative phosphorylation, respectively. As the inhibition of only one energy-producing pathway can be compensated for by an increase of the other, cells are able to withstand the mono treatment but experience excessive stress upon combination treatment. While the mechanistic link between (R)-GNE-140 and glycolysis inhibition is well-characterized, further studies are required to unravel the mechanism behind BMS-986205 mediated inhibition of oxidative phosphorylation.

4.4 From energy stress to senescence

Energy homeostasis is fundamental to ensure proper cellular function. Therefore, it is not surprising that disruption of energy metabolism is closely linked to severe cellular stress and the induction of senescence (Miwa et al., 2022). Since the majority of cellular energy is produced by mitochondrial respiration, mitochondrial dysfunction is considered to be one of the major drivers of senescence (Martini and Passos, 2023). One of the senescence-inducing mechanisms underlying mitochondrial dysfunction is the deregulation of nicotinamide metabolism, which directly impairs the electron transport chain and causes formation of ROS, which in turn induces DNA-damage, activation of the G2/M DNA damage checkpoint, leading to cell-cycle arrest and ultimately leading to the development of senescence, as shown by others (Finkel and Holbrook, 2000; Wiley *et al.*, 2016; Kwon *et al.*, 2019; Wang *et al.*, 2019; Kumari and Jat, 2021; Wiley and Campisi, 2021). The present study has provided evidence to support this mechanism. However, as the development of senescence is highly complex and poorly understood, several other mechanisms may contribute to the observed phenotype, as schematically summarized in Fig. 31.

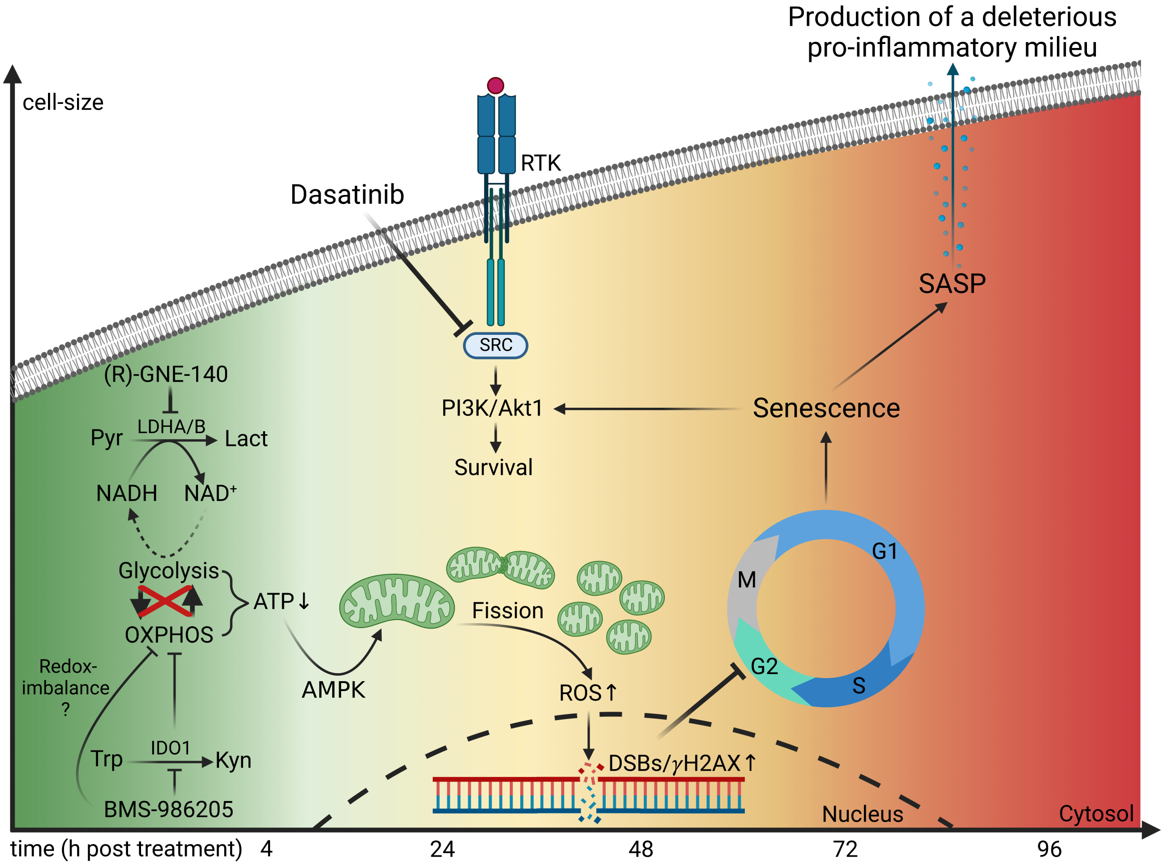

Fig. 31: The mechanism of (R)-GNE-140 and BMS-986205 combination treatment in KRAS^{G12V}/MYC cancer cells.
(R)-GNE-140 indirectly inhibits glycolysis through inhibition of LDHA/B which leads to reduced levels of cytosolic NAD$^+$, required for several glycolytic enzymes. BMS-986205 inhibits IDO1 and mitochondrial respiration. Cells survive treatment with either (R)-GNE-140 or BMS-986205 due to the mutual compensation of glycolysis and oxidative phosphorylation. However, upon combination treatment, compensatory ability is lost and ATP decrease, leading to severe energy stress. Energy stress is sensed by AMPK, mitochondrial fission is induced and ROS levels increase. ROS-induced DNA damage leads to activation of the G2/M checkpoint and cell cycle arrest. Ultimately, all of these processes contribute to the induction of senescence and the development of the SASP. Senescent KRAS^{G12V}/MYC cells can then be eliminated through apoptosis using Dasatinib, a SRC inhibitor that interferes with PI3K/Akt1 mediated survival signaling. Pyruvate, Pyr; lactate, Lact; tryptophan, Trp; kynurenine, Kyn; adenosine triphosphate, ATP; adenosin monophosphate-activated kinase, AMPK; reactive oxygen species, ROS; receptor-tyrosine kinase, RTK; SRC kinase, SRC; DNA double-strand breaks, DSBs; senescence-associated secretory phenotype, SASP. X-axis: hours post treatment versus Y-axis: cell size. Created with BioRender.

4.4.1 The (R)-GNE-140 and BMS-986205 induced senescence phenotype

Combined treatment with (R)-GNE-140 and BMS-986205 selectively induced senescence in cancer cells, as evidenced by the increase in ß-galactosidase activity, enlarged and flattened morphology and cell cycle arrest in KRAS^{G12V}/MYC cells but not in healthy empty vector cells. Another hallmark of cellular senescence is the development of a pro-inflammatory secretion program, the SASP. qPCR and conditioned medium experiments showed the selective development of SASP in KRAS^{G12V}/MYC cells after 4 days of combination treatment. This was supported by longitudinal transcriptomic data that revealed the onset of a pro-inflammatory gene expression signature after 3 days of combination treatment, which increase steadily until 5 days post-treatment (data not shown). OLINK secretome analysis confirmed that the senescent cancer cells produce a pro-inflammatory secretome consisting of the core SASP components IL6, GDF15, IL1 and a plethora of MMPs (data not shown).

Using the senolytic drug Dasatinib, it was possible to selectively eliminate senescence KRAS^{G12V}/MYC cells through apoptosis. The ability of Dasatinib to effectively induce apoptosis in senescent cells is mediated by inhibition of SRC (Araujo and Logothetis, 2010). SRC is a receptor tyrosine kinase capable of phosphorylating the regulatory subunit of PI3K, leading to its activation, which in turn activates AKT1 (Hatton *et al.*, 2012). Dasatinib is able to induce apoptosis by interfering with PI3K/AKT1-mediated anti-apoptotic signaling of senescent cells (Zhu *et al.*, 2015; Soto-Gamez and Demaria, 2017). Thus the (R)-GNE-140 and BMS-986205 induced senescent phenotype in KRAS^{G12V}/MYC cancer cells relies on PI3K/AKT1-mediated pro-survival signaling.

4.5 Cancer cell selectivity of (R)-GNE-140 and BMS-986205

Cancer cells adapt their metabolism during development to support their increased proliferation rate. Following this idea, therapies that target cancer-associated metabolic pathways may also have severe effects on highly proliferating normal cells or cells that are intrinsically dependent on pathways that are exploited for cancer therapy (Galluzzi *et al.*, 2013; Luengo, Gui and Vander Heiden, 2017).

In this work, the combination of (R)-GNE-140 and BMS-986205 preferentially prevented the proliferation of KRAS^{G12V}/MYC cancer cells, but also showed limited effects on non-cancerous empty vector cells. Since cancer cells divide faster than healthy cells, DMSO-treated cancer cells will reach confluence faster than DMSO-treated non-cancer cells. Therefore, cell viability assays may be partially biased towards a higher treatment response of cancer cells. This experimental bias could not be avoided. However, in most phenotypic observations as well as biochemical and molecular assays (cell morphology, mitochondrial number, ROS levels, DNA damage, cell cycle arrest, SA-ß-gal activity/senescence and SASP gene expression and secretion), KRAS^{G12V}/MYC cancer cells showed a significantly stronger response to the (R)-GNE-140 and BMS-986205 combination treatment than non-cancerous empty vector cells. This selectivity can be explained by the higher energy requirements of cancer cells. As shown by metabolic flux analyses, the combination treatment leads to simultaneous inhibition of glycolysis and oxidative phosphorylation. Therefore, over the same treatment period, the energy deficit of the cancer cells becomes much greater than that of healthy cells, explaining the higher stress response of KRAS^{G12V}/MYC cells. This was particularly highlighted by the increased oxidative stress, which was reflected by an 8-fold increase of ROS levels in KRAS^{G12V}/MYC cells, compared to a 3-fold increase in empty vector cells. Consequently, cancer cells were more severely damaged, which ultimately contributed to the selective induction of senescence. In addition, the non-cancerous empty vector control cells, used to study drug selectivity in this work, cannot be compared to healthy tissue cells, which proliferate much slower. Therefore, the drug combinations cancer selectivity may be even more pronounced when tested on healthy primary tissue cells or *in vivo*.

Despite this selectivity, simultaneous inhibition of glycolysis and oxidative phosphorylation, pathways all tissue cells survival relies on, can cause severe side-effects on the organismal level. In fact, Metformin and 2-DG, a combination that simultaneously inhibits oxidative phosphorylation and glycolysis, has not been clinically applicable due to their relatively high cytotoxicity (Stein *et al.*, 2010; Garon *et al.*, 2014; Mathews Samuel *et al.*, 2019; Zhao *et al.*, 2019; Gremke *et al.*, 2020; Tan *et al.*, 2020). Nevertheless, this work suggests that the combination of (R)-GNE-140 and BMS-986205 is superior to the combination of Metformin and (R)-GNE-140, as the latter also induced a high level of toxicity towards non-cancerous empty vector cells. The exact mechanisms behind the inhibition of oxidative phosphorylation by Metformin remain a matter of speculation (Luengo, Sullivan and Heiden, 2014; Fontaine, 2018). Notably, Metformin has been shown to have additional inhibitory effects on complexes III and IV (Fontaine, 2018), which may contribute to the observed higher cytotoxicity compared to BMS-986205.

This work provides further evidence that not all cell lines were equally damaged by the combination treatment. 3 out of 11 human cell lines and 2 out of 4 murine cell lines (data not shown) showed little or no response, suggesting that some cell lines can compensate for or avoid the effects of the combination treatment. The cancer cell selectivity of (R)-GNE-140 and BMS-986205 combination treatment needs to be further analyzed. To this end, the drug combination will be validated in a mouse model of small cell lung cancer (SCLC). In addition to analyzing the tumor response, potential organ toxicity will be investigated. In conclusion, the (R)-GNE-140 and BMS-986205 combination therapy has promising potential to be cancer selective, which will be tested *in vivo*.

4.6 Opportunities for (R)-GNE-140 and BMS-986205 combination therapy

4.6.1 Tumor microenvironment targeted therapy

Conventional cancer therapies target rapidly proliferating cells by interfering with DNA replication or other hallmarks of cancer to achieve selectivity. Frequent relapse due to the development of treatment resistance raises the importance of new treatment strategies. A novel target being investigated for antitumor therapy is the TME. In most cases, the TME is of pro-tumorigenic nature. This is largely due to a unique secretome comprised of anti-inflammatory molecules which suppress the immune system and promote tumor growth. Therefore, combined treatment of conventional chemotherapy and TME-targeted therapy holds great future potential e.g. for ovarian cancer, where clinical studies have shown that initial platinum-based chemotherapy results in increased immune cell infiltration through interferon signaling and concomitant upregulation of PD-L1, resulting in immune suppression (Galluzzi *et al.*, 2015; Färkkilä *et al.*, 2020; Yaniz *et al.*, 2020).

In addition to anti-inflammatory cytokines, secreted immunosuppressive metabolites play a critical role in determining the tumorigenic properties of a TME. Two key metabolites with immunosuppressive functions that have been identified in the TME are lactate and kynurenine (Munn *et al.*, 1999; Opitz *et al.*, 2011; Romero-Garcia *et al.*, 2016; Corbet and Feron, 2017; Boedtkjer and Pedersen, 2020; García-Cañaveras and Lahoz, 2021). Many cancer cells have developed a strong glycolytic phenotype, resulting in the production and secretion of lactic acid, enabling cancer cells to acidify the extracellular pH to 6.0 – 6.5 (Xie *et al.*, 2014). Such acidic environments, serve as metabolic fuel for cancer cells, promote angiogenesis and inhibit immune cell function (Fischer *et al.*, 2007; Mendler *et al.*, 2012). Kynurenine is a metabolite produced from tryptophan by the enzyme IDO1 and exerts its immunosuppressive function by inhibiting effector T cells and NK cells leading to the differentiation and activation of regulatory T cells (Chung *et al.*, 2009). In this regard, the combination of (R)-GNE-140 and BMS-986205 has the ability to target cancer cells from two independent sites. On the one hand, the combination exerts its toxic effects directly on rapidly proliferating cancer cells by limiting energy availability. On the other hand, according to literature, inhibition of LDHA/B and IDO1 reduces lactate and kynurenine production, thereby decreasing their extracellular levels, which could reduce the immunosuppressive functions of the TME (Prendergast *et al.*, 2018; Serganova *et al.*, 2018). For these reasons, BMS-986205 has already been used in several clinical trials (Luke *et al.*, 2019; Sonpavde *et al.*, 2020; Bristol-Myers Squibb, 2022). It will be interesting to compare the effects of the (R)-GNE-140 and BMS-986205 combination treatment between immunodeficient and immunocompetent mice to clarify the contribution of a potentially reactivated immune system.

Another way in which (R)-GNE-140 and BMS-986205 could remodel the composition of the TME is by inducing senescence in cancer cells. Senescent cells will develop a pro-inflammatory SASP, which may be able to transform an anti-inflammatory TME into a pro-inflammatory TME, thus stimulating the immune response. Prolonged SASP-induced tissue damage can then be suppressed by eliminating senescent cells with senolytics, as this study has shown with the use of Dasatinib. In conclusion, (R)-GNE-140 and BMS-986205 may exert significant anti-tumor activity by simultaneously limiting the energy availability of tumor cells and remodeling the anti-inflammatory into a pro-inflammatory TME *in vivo*.

4.6.2 Improving the selectivity of cancer treatment strategies

The combination treatment of (R)-GNE-140 and BMS-986205 may cause severe side effects due to the simultaneous inhibition of glycolysis and oxidative phosphorylation. In this case, the drug combination could still be of future clinical use, just not conventionally as a "naked" drug. The relatively new but rapidly growing field of nanoparticle-based drug delivery represents a promising opportunity to reduce side effects by delivering drugs directly to tumors (Amreddy *et al.*, 2015; Patra *et al.*, 2018; Yao *et al.*, 2020). Nanoparticles encapsulating the drugs of interest can be coated with receptors or other molecules that interact with receptors that are overexpressed on cancer cells and present at low levels on normal cells, e.g. transferrin receptors (Cui *et al.*, 2017). Coating with folic acid has also been shown to enable cancer-selective drug delivery as ~40% of cancers show an increased expression of the alpha isoform of the folate receptor (FR-alpha) (Low and Kularatne, 2009; Muralidharan *et al.*, 2016). Others have successfully used pH-responsive nanoparticles, which primarily dissolve in the acidic tumor microenvironment (Zhuo *et al.*, 2020; AlSawaftah *et al.*, 2022).

Another approach to improve drug delivery to tumors involves the use of microenvironment priming agents. These priming agents alter the structure and functions of tissues or the TME to facilitate localized drug delivery. For example, the application of proteases into the TME to digest the ECM barrier resulted in enhanced drug diffusion to the solid tumor (Eikenes *et al.*, 2010). In addition, priming agents can be used to reduce drug uptake by healthy tissue cells (Kennel *et al.*, 2008; Ohara *et al.*, 2012; Khalid *et al.*, 2017).

Recently (03.03.2023), another exciting strategy for the selective delivery of anti-cancer drugs has attracted the attention of BioNTech in a $1.67 billion collaboration agreement (BioNTech, 2023). Using antibody-drug conjugates, drugs can be targeted to cancer cells via neoantigens present on the cell surface (Fu *et al.*, 2022). A cleavable (pH-sensitive) linker allows the drug to be released, for example, in the acidic TME. Strategies such as these could pave the way for drugs that have failed in the past to be used in the clinical in the future.

4.7 Heterogenic responses to (R)-GNE-140 and BMS-986205 combination treatment

The combination of (R)-GNE-140 and BMS-986205 has a synergistic cytotoxic effect on most of the cell lines tested in this study, demonstrating the high metabolic sensitivity of cancer cells to this treatment. Interestingly, cells responded with senescence or apoptosis or only with cell cycle arrest. Despite these heterogeneous responses, I assume that the basic mechanism behind the synergy of the combination treatment (simultaneous inhibition of glycolysis and oxidative phosphorylation) is similar in all cell lines. This hypothesis is supported by the observed changes in the pH of the cell culture medium. In particular, the acidic pH after treatment with BMS-986205 indicates a drastic increase in glycolysis to compensate for the inhibition of the previously described oxidative phosphorylation. This metabolic reprogramming was similar among all cell lines tested and explains why addition of the glycolysis inhibitor (R)-GNE-140 causes an energetic catastrophe.

Why are some cell lines more sensitive to the combination of (R)-GNE-140 and BMS-986205 than others? Don’t all cells experience the same degree of stress? It is known that a cell succumbs to apoptosis when subjected to intolerable stress, whereas senescence is a consequence of milder damage. For example, studies have shown that low doses of Adriamycin induce senescence, whereas high doses induce apoptosis in MCF-7 cells (Song, Lee and Hwang, 2005). Oxidative damage also shows a dose-dependent induction of senescence or apoptosis (Chen and Ames, 1994; Chen, Liu and Merrett, 2000). Therefore, some cells may be able to withstand the combination treatment of (R)-GNE-140 and BMS-986205 by developing strategies to compensate for the energy stress to reduce damage. Consequently, cells that can compensate for the energy deficit are only slightly affected, while cells with partial compensatory ability initiate senescence to reduce energy consumption and thus survive and cells that cannot compensate for the energy deficit, however, induce apoptosis.

The compensatory capacity of cells is determined by their ability to adapt and remodel their metabolism and signaling cascades in response to stress. For example, energy stress results in decreased ATP and increased AMP levels (Cheung *et al.*, 2000). AMPK will be activated by increased AMP levels and inactivates ACC through phosphorylation at Ser-79, leading to inhibition of energy-consuming fatty acid synthesis and upregulation of energy-producing mitochondrial ß-oxidation (Fullerton *et al.*, 2013; Lally *et al.*, 2019). In addition, AMPK can compensate energy stress by reducing cholesterol synthesis through HMG-CoA inhibition (Zhang *et al.*, 2015). Another compensatory strategy involves the upregulation of glutaminolysis. Glutamine plays a central role in energy metabolism as it is important for maintaining redox homeostasis, the generation of nucleotides, pyruvate and other macromolecules (Tong, Zhao and Thompson, 2009; Yoo *et al.*, 2020; Kao *et al.*, 2022). The importance of glutamine becomes clear when the glutamine dependence of some cancer cell lines is examined. Interestingly, mutant KRAS and MYC driven cancers have been shown to be glutamine addicted (Wise and Thompson, 2010; Suzuki *et al.*, 2022). For example, oncogenic MYC induces the expression of glutamine importers SLC1A5 and SLC38A5 as well as the enzyme glutamine synthetase (Wise *et al.*, 2008; Bott *et al.*, 2015). Thus, cells capable of reprogramming their metabolism or exhibiting intrinsic upregulation of alternative energy generation pathways may be able to compensate for or circumvent the deleterious effects of (R)-GNE-140 and BMS-986205 combination treatment (Fig. 32).

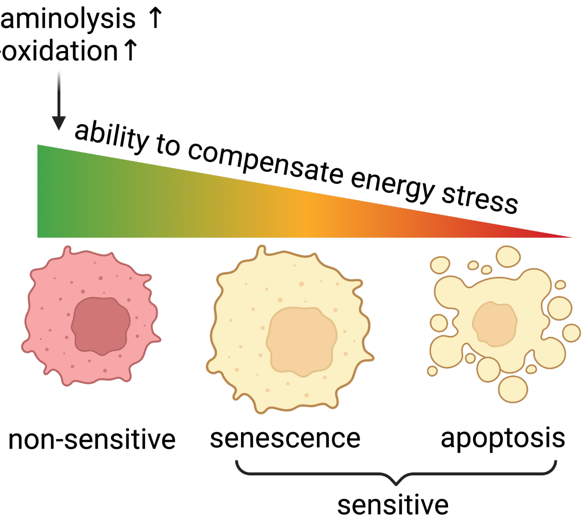

Fig. 32: Heterogenous responses to (R)-GNE-140 and BMS-986205 could be explained by the cells different ability to adapt to energy-stress.
The ability of cells to efficiently use pathways that contribute to energy-homeostasis, determines their ability to compensate for energy-stress. This is underscored by the varying degrees of sensitivity to the combined treatment with (R)-GNE-140 and BMS-986205, as reflected by the heterogeneous responses of the cell lines tested in this study. Created with BioRender.

Future studies could include transcriptomic, proteomic and, most valuable for metabolic perturbation studies, metabolomic screens of a whole battery of cell lines subjected to the combination treatment. The aim would be to identify similar response patterns and investigate whether there is a correlation with the overall cellular response. I am currently planning to perform this screening at the transcriptomic level for all the cell lines tested in this study.

Summary

Despite advances in the therapy of high-grade serous ovarian cancer, overall survival rates remain stagnant, highlighting the need for innovative treatment strategies. In the present study, immortalized fallopian tube secretory epithelial cells were transformed to cancer cells upon expression of KRAS^{G12V} and MYC, allowing the side-to-side comparison of an ovarian cancer cell line with its immortalized precursor. A synthetic lethal screen using sublethal concentrations of two inhibitors targeting distinct metabolic pathways showed that the combination of (R)-GNE-140 and BMS-986205 preferentially prevented the proliferation of KRAS^{G12V}/MYC cancer cells. While it is known that (R)-GNE-140 prevents lactate fermentation and glycolysis upon inhibition of LDHA/B, the clinically used drug BMS-986205 reportedly inhibits IDO1 and - as revealed in this study - also proper folding of mitochondrial cristae. Accordingly, this study showed that BMS-986205 inhibited oxidative phosphorylation and led to decreased abundance of FAD and succinate, which are important for the activity of electron transport chain complex II. The synergistic activity of BMS-986205 and (R)-GNE-140 on the inhibition of cell proliferation was not recapitulated by using other inhibitors or siRNAs against their known targets LDHA/B and IDO1, underscoring the functional importance of BMS-986205-dependent restructuring of the inner mitochondrial membrane. The combination of BMS-986205 (inhibiting oxidative phosphorylation) and (R)-GNE-140 (interfering with regeneration of NAD$^+$ for effective glycolysis) resulted in a decrease of cellular ATP and caused an energetic catastrophe, selectively inducing senescence in KRAS^{G12V}/MYC cancer cells. Senescent cancer cells showed increased ß-galactosidase activity, increased ROS production, DNA damage, G2/M cell cycle arrest and the development of the senescence-associated secretory phenotype. These senescent cells were effectively eliminated by apoptosis in the presence of the senolytic compound Dasatinib. In addition to KRAS^{G12V}/MYC cancer cells, 16 out of 22 well-established human and murine cancer cell lines were sensitive to the combination treatment. As 6 cell lines were not or only slightly affected by (R)-GNE-140 and BMS-986205, a general cytotoxicity of this drug combination can be excluded. While this synthetic lethal approach demonstrates the feasibility of simultaneously blocking multiple metabolic pathways

in cell culture experiments, future studies will determine whether this approach also works in suitable mouse models.

Zusammenfassung

Trotz Fortschritten in der Therapie von hochgradigen serösen Ovarialkarzinomen stagniert die Gesamtüberlebensrate, was die Notwendigkeit innovativer Behandlungsstrategien unterstreicht. In der vorliegenden Studie wurden immortalisierte sekretorische Epithelzellen des Eileiters durch Expression von $KRAS^{G12V}$ und MYC in Krebszellen transformiert, was den Vergleich einer Ovarialkarzinom-Zelllinie mit ihrem immortalisierten Vorläufer ermöglichte. Ein synthetisches Letalitäts-Screening subletaler Konzentrationen von zwei Inhibitoren, die unterschiedliche Stoffwechselwege hemmen, zeigte, dass die Kombination von (R)-GNE-140 und BMS-986205 bevorzugt die Proliferation von $KRAS^{G12V}$/MYC-Krebszellen verhindert. Während bekannt ist, dass (R)-GNE-140 durch die Hemmung von LDHA/B die Laktatfermentation und Glykolyse verhindert, hemmt das klinisch eingesetzte Medikament BMS-986205 laut Literatur IDO1 und - wie in dieser Studie gezeigt wurde - auch die korrekte Faltung der mitochondrialen Cristae und somit die oxidative Phosphorylierung. Dementsprechend konnte nachgewiesen werden, dass BMS-986205 zu einer Reduktion von FAD und Succinat Leveln führte, welche wichtig für die Aktivität von Komplex II der Elektronentransportkette sind. Die durch BMS-986205 und (R)-GNE-140 vermittelte synergistische Hemmung der Zellproliferation konnte durch die Verwendung anderer Inhibitoren oder siRNAs, gegen die bekannten Zielmoleküle LDHA/B und IDO1, nicht rekapituliert werden. Dies unterstreicht die funktionelle Bedeutung der BMS-986205-abhängigen Umstrukturierung der inneren Mitochondrienmembran. Die Kombination von BMS-986205 (Hemmung der oxidativen Phosphorylierung) und (R)-GNE-140 (Beeinträchtigung der Regeneration von NAD^+ für eine effektive Glykolyse) führte zu einem deutlichen Rückgang des zellulären ATPs und verursachte eine energetische Katastrophe, die selektiv Seneszenz in $KRAS^{G12V}$/MYC-Krebszellen auslöste. Diese seneszenten Krebszellen zeigten eine erhöhte ß-Galaktosidase-Aktivität, erhöhte ROS-Produktion, DNA-Schäden, G2/M-Zellzyklus-Arrest und die Entwicklung des seneszenz-assoziierten sekretorischen Phänotyps. Mit Hilfe des senolytisch aktiven Medikamentes Dasatinib war es möglich, selektiv Apoptose in seneszenten Krebszellen auszulösen.

Zusätzlich zu den KRAS^{G12V}/MYC-Krebszellen waren 16 von 22 etablierten menschlichen und murinen Krebszelllinien empfindlich gegenüber der Kombinationsbehandlung. Da 6 Zelllinien nicht oder nur geringfügig von (R)-GNE-140 und BMS-986205 betroffen waren, kann eine allgemeine Zytotoxizität dieser Wirkstoffkombination ausgeschlossen werden. Während dieser synthetisch-letale Ansatz die Machbarkeit der gleichzeitigen Blockierung mehrerer Stoffwechselwege in Zellkulturexperimenten demonstriert, werden zukünftige Studien zeigen, ob dieser Ansatz auch in geeigneten Mausmodellen antitumorale Wirkungen erzielt.

Abbreviations

% (v/v)	volume/volume percentage (ml/100 ml)
% (w/v)	weight/volume percentage (g/100 ml)
°C	Celsius
2-DG	2-deoxyglucose
2-HG	2-hydroxyglutarate
4E-BP1	4E-binding protein 1
ACC	acetyl-CoA carboxylase
AKT1	AKT serine/threonine kinase 1
AML	acute myeloid leukemia
AMPK	AMP-activated protein kinase
ATM	Ataxia telangiectasia mutated
ATP	adenosine triphosphate
ATR	Ataxia telangiectasia mutated and Rad3-related
BrdU	bromodesoxyuridin
BSD	blasticin S deaminase
CAF	cancer associated fibroblast
CDI	coefficient of drug interaction
cDNA	complementary DNA
CM	conditioned medium
C_T	cycle threshold
Da	Dalton
DAMP	damage-associated molecular pattern
Das	Dasatinib
DCA	dichloroacetate
DMEM	Dulbecco’s modified eagle medium
DMKG	dimethyl alpha-ketoglutarate
DNA	deoxyribonucleic acid
DRP	dynamine-related protein
dsDNA	double-stranded DNA
ECAR	extracellular acidification rate

ECM	extracellular matrix
eIF4E	eukaryotic initiation factor 4E
ETC	electron transport chain
FASN	fatty acid synthase
FDR	false discovery rate
FIJI	FIJI is just image J
FR	folate receptor
FTSEC	fallopian tube secretory epithelial cells
GAPDH	glyceraldehyde 3-phosphate
GLUT1	glucose transporter 1
GNE	(R)-GNE-140
GO	gene ontology
GSH	glutathione
HGSOC	high-grade serous ovarian cancer
HK	hexokinase
HR	homologous recombination
HRP	horseradish peroxidase
IDH	isocitrate dehydrogenase
IDO	indoleamine 2,3-dioxygenase
IL	interleukin
KRAS	Kirsten rat sarcoma virus
LB	lysogeny broth
LDH	lactate dehydrogenase
MCT-1	monocarboxylate transporter 1
MFN	mitofusin
MICOS	mitochondrial contact site and cristae organizing system
MMP	matrix metalloprotease
mTOR	mammalian target of rapamycin
mtROS	mitochondrial ROS
MYC	Myelocytomatosis
NAC	N-acetylcysteine
NF-κB	nuclear factor κB

NK	natural killer
NR	nicotinamide ribosie
NSCLC	non-small cell lung cancers
OCR	oxygen consumption rate
OD	optical density
OXPHOS	oxidative phosphorylation
PARP	poly (ADP-ribose) polymerase
PGC1α	PPARgamma co-activator-1
PGK1	phosphoglycerate kinase
PI	propidium iodide
PI3K	Phophatidylinositol 3-kinase
qPCR	quantitative real-time polymerase chain reaction
Rb	Retinoblastoma
RNA	ribonucleic acid
ROS	reactive oxygen species
RT	room temperature
RTK	receptor tyrosine kinase
SA-ß-gal	senescence-associated ß-gal
SASP	senescence-associated secretory phenotype
SD	standard deviation
SDH	succinate dehydrogenase
shRNA	short-hairpin RNA
siRNA	short-interfering RNA
SLCL	small cell lung cancer
ß-gal	beta-galactosidase
STIC	serous tubal intraepithelial carcinoma
TAM	tumor-associated macrophage
TCA	tricarboxic acid cycle
TCGA	The cancer genome atlas (project)
TDO	tryptophan 2,3-dioxygnase
TEM	transmission electron microscopy
Th	T-helper
TME	tumor microenvironment

TNFα	tumor necrosis factor α
V	volt
VEGF	vascular endothelial growth factor
wt	wildtype

Collaborations

The experiments were designed, performed, and evaluated by Jan Dreute and Prof. Lienhard Schmitz, unless otherwise stated. Since Jan Dreute supervised the medical doctoral students Julia Stengel, Till Wöckener and David van den Borre and the intern Chloe Leff, the following experiments were designed, performed or evaluated in close collaboration. Additional collaborations with other laboratories are listed.

Fig. 6C:	KRAS^{G12V}/MYC transduced iFTSEC show increased migratory and invasive capacity. Collaboration with **Veronika Shinkevich** (AG Worzfeld).
Fig. 8	Transcriptome analysis reveals upregulated KRAS and MYC signaling. Collaboration with **Jasmin Priester** (AG Kracht).
Fig. 9	Glycolysis is upregulated in KRAS^{G12V}/MYC cancer cells. Collaboration with **Vidya Lakshmi** (AG Sommer).
Fig. 10	The combination of (R)-GNE-140 and BMS-986205 exerts synergistic cytotoxicity. Collaboration with **Julia Stengel**.
Fig. 12	(R)-GNE-140 and BMS-986205 combination treatment increases cell size. Collaboration with **Julia Stengel.**
Fig. 13	(R)-GNE-140 and BMS-986205 selectively induces senescence in KRASG12V/MYC cells. Collaboration with **Julia Stengel**, **Till Wöckener** and **Chloe Leff**.

Fig. 14	Senescence induction is p16/p21 independent. Collaboration with **Julia Stengel**.
Fig. 15	Combination of (R)-GNE-140 and BMS-986205 induces pro-inflammatory gene expression after prolonged treatment. Collaboration with **Chloe Leff**.
Fig. 17	Induction of apoptosis in senescent cells using the senolytic Dasatinib. Collaboration with **David v.d. Borre**.
Fig. 18B	Cell cycle arrest, DNA damage and increased ROS levels after (R)-GNE-140 and BMS-986205 combination treatment. Collaboration with **Julia Stengel**.
Fig. 19	Different supplementation strategies failed to rescue the effects of (R)-GNE-140 and BMS-986205 combination treatment. Collaboration with **Julia Stengel**.
Fig. 20	Increase in mitochondrial abundance after (R)-GNE-140 and BMS-986205 combination treatment. In collaboration with **Dr. Ulrich Gärtner, Tamara Papadakis** (Institute for Anatomy and Cell Biology at the Justus Liebig University Giessen) and **David v.d. Borre**.
Fig. 22	Simultaneous inhibition of glycolysis and oxidative phosphorylation upon (R)-GNE-140 and BMS-986205 combination treatment. Collaboration with **Vidya Lakshmi** (AG Sommer).
Fig. 23	Effects of (R)-GNE-140 and BMS-986205 on metabolic pathways. Collaboration with **Dr. Stephan Klatt (**Institute for Vascular Signaling, University Hospital Frankfurt/Goethe University).

Fig. 24	Activation of AMPK signaling after (R)-GNE-140 and BMS-986205 combination treatment. Collaboration with **David v.d. Borre**.
Fig. 25	Other inhibitors targeting LDHA/B and IDO1 cannot recapitulate the effects (R)-GNE-140 and BMS-986205 combination treatment. Collaboration with **Julia Stengel**.
Figs. 27-30	Translation of (R)-GNE-140 and BMS-986205 combination treatment to other well-established cancer cell lines. Collaboration with **Julia Stengel** und **Till Wöckener**.

References

Agarwal, A., Gupta, S. and Sharma, R.K. (2005) ‘Role of oxidative stress in female reproduction’, *Reproductive biology and endocrinology : RB&E*, 3, p. 28. Available at: https://doi.org/10.1186/1477-7827-3-28.

Akdemir, K.C. *et al.* (2020) ‘Somatic mutation distributions in cancer genomes vary with three-dimensional chromatin structure’, *Nature Genetics*, 52(11), pp. 1178–1188. Available at: https://doi.org/10.1038/s41588-020-0708-0.

Al Tameemi, W. *et al.* (2019) ‘Hypoxia-Modified Cancer Cell Metabolism’, *Frontiers in Cell and Developmental Biology*, 7. Available at: https://www.frontiersin.org/articles/10.3389/fcell.2019.00004 (Accessed: 13 April 2023).

AlSawaftah, N.M. *et al.* (2022) ‘pH-Responsive Nanocarriers in Cancer Therapy’, *Polymers*, 14(5), p. 936. Available at: https://doi.org/10.3390/polym14050936.

Am, K. and R, D. (2010) ‘Ovarian cancer pathogenesis: a model in evolution’, *Journal of oncology*, 2010. Available at: https://doi.org/10.1155/2010/932371.

Amreddy, N. *et al.* (2015) ‘Tumor-targeted and pH-controlled delivery of doxorubicin using gold nanorods for lung cancer therapy’, *International Journal of Nanomedicine*, 10, pp. 6773–6788. Available at: https://doi.org/10.2147/IJN.S93237.

Anderson, S.N. *et al.* (2007) ‘A High-Throughput Soft Agar Assay for Identification of Anticancer Compound’, *SLAS Discovery*, 12(7), pp. 938–945. Available at: https://doi.org/10.1177/1087057107306130.

Antunes, N. *et al.* (2022) ‘In Vitro Cancer Models: A Closer Look at Limitations on Translation’, *Bioengineering*, 9(4), p. 166. Available at: https://doi.org/10.3390/bioengineering9040166.

Araujo, J. and Logothetis, C. (2010) ‘Dasatinib: a potent SRC inhibitor in clinical development for the treatment of solid tumors’, *Cancer treatment reviews*, 36(6), pp. 492–500. Available at: https://doi.org/10.1016/j.ctrv.2010.02.015.

Armstrong, J.S. *et al.* (2002) ‘Role of glutathione depletion and reactive oxygen species generation in apoptotic signaling in a human B lymphoma cell line’, *Cell Death & Differentiation*, 9(3), pp. 252–263. Available at: https://doi.org/10.1038/sj.cdd.4400959.

Arora, T., Mullangi, S. and Lekkala, M.R. (2022) ‘Ovarian Cancer’, in *StatPearls*. Treasure Island (FL): StatPearls Publishing. Available at: http://www.ncbi.nlm.nih.gov/books/NBK567760/ (Accessed: 23 February 2023).

Asangba, A.E. *et al.* (2023) ‘Diagnostic and prognostic potential of the microbiome in ovarian cancer treatment response’, *Scientific Reports*, 13(1), p. 730. Available at: https://doi.org/10.1038/s41598-023-27555-x.

Baghban, R. *et al.* (2020) ‘Tumor microenvironment complexity and therapeutic implications at a glance’, *Cell Communication and Signaling*, 18(1), p. 59. Available at: https://doi.org/10.1186/s12964-020-0530-4.

Balog, A. *et al.* (2021) ‘Preclinical Characterization of Linrodostat Mesylate, a Novel, Potent, and Selective Oral Indoleamine 2,3-Dioxygenase 1 Inhibitor’, *Molecular Cancer Therapeutics*, 20(3), pp. 467–476. Available at: https://doi.org/10.1158/1535-7163.MCT-20-0251.

Basisty, N. *et al.* (2020) ‘A proteomic atlas of senescence-associated secretomes for aging biomarker development’, *PLOS Biology*, 18(1), p. e3000599. Available at: https://doi.org/10.1371/journal.pbio.3000599.

Baz-Martínez, M. *et al.* (2016) ‘Cell senescence is an antiviral defense mechanism’, *Scientific Reports*, 6, p. 37007. Available at: https://doi.org/10.1038/srep37007.

Bell, D. *et al.* (2011) ‘Integrated genomic analyses of ovarian carcinoma’, *Nature*, 474(7353), pp. 609–615. Available at: https://doi.org/10.1038/nature10166.

Ben-David, U. *et al.* (2018) ‘Genetic and transcriptional evolution alters cancer cell line drug response’, *Nature*, 560(7718), pp. 325–330. Available at: https://doi.org/10.1038/s41586-018-0409-3.

van der Bliek, A.M., Shen, Q. and Kawajiri, S. (2013) ‘Mechanisms of Mitochondrial Fission and Fusion’, *Cold Spring Harbor Perspectives in Biology*, 5(6), p. a011072. Available at: https://doi.org/10.1101/cshperspect.a011072.

Boedtkjer, E. and Pedersen, S.F. (2020) ‘The Acidic Tumor Microenvironment as a Driver of Cancer’, *Annual Review of Physiology*, 82, pp. 103–126. Available at: https://doi.org/10.1146/annurev-physiol-021119-034627.

Bond, S.T. *et al.* (2017) ‘Lysine post-translational modification of glyceraldehyde-3-phosphate dehydrogenase regulates hepatic and systemic metabolism’, *FASEB journal: official publication of the Federation of American Societies for Experimental Biology*, 31(6), pp. 2592–2602. Available at: https://doi.org/10.1096/fj.201601215R.

Borella, F. *et al.* (2020) ‘Immune Checkpoint Inhibitors in Epithelial Ovarian Cancer: An Overview on Efficacy and Future Perspectives’, *Diagnostics*, 10(3), p. 146. Available at: https://doi.org/10.3390/diagnostics10030146.

Borowicz, S. *et al.* (2014) ‘The Soft Agar Colony Formation Assay’, *Journal of Visualized Experiments : JoVE*, (92), p. 51998. Available at: https://doi.org/10.3791/51998.

Bose, S., Clevers, H. and Shen, X. (2021) ‘Promises and Challenges of Organoid-Guided Precision Medicine’, *Med (New York, N.Y.)*, 2(9), pp. 1011–1026. Available at: https://doi.org/10.1016/j.medj.2021.08.005.

Bott, A.J. *et al.* (2015) ‘Oncogenic Myc induces expression of glutamine synthetase through promoter demethylation’, *Cell metabolism*, 22(6), pp. 1068–1077. Available at: https://doi.org/10.1016/j.cmet.2015.09.025.

Boudreau, A. *et al.* (2016) ‘Metabolic plasticity underpins innate and acquired resistance to LDHA inhibition’, *Nature Chemical Biology*, 12(10), pp. 779–786. Available at: https://doi.org/10.1038/nchembio.2143.

Bristol-Myers Squibb (2022) *A Phase 1/2a Study of BMS-986205 Administered in Combination With Nivolumab (Anti-PD-1 Monoclonal Antibody) and in Combination With Both Nivolumab and Ipilimumab (Anti-CTLA-4 Monoclonal Antibody) in Advanced Malignant Tumors*. Clinical trial registration NCT02658890. clinicaltrials.gov. Available at: https://clinicaltrials.gov/ct2/show/NCT02658890 (Accessed: 17 February 2023).

Bronder, D. *et al.* (2021) ‘TP53 loss initiates chromosomal instability in fallopian tube epithelial cells’, *Disease Models & Mechanisms*, 14(11), p. dmm049001. Available at: https://doi.org/10.1242/dmm.049001.

Brown, T.A. (2002) *Mutation, Repair and Recombination*, *Genomes. 2nd edition*. Wiley-Liss. Available at: https://www.ncbi.nlm.nih.gov/books/NBK21114/ (Accessed: 22 February 2023).

Buckley, A.M. *et al.* (2020) ‘Targeting hallmarks of cancer to enhance radiosensitivity in gastrointestinal cancers’, *Nature Reviews Gastroenterology & Hepatology*, 17(5), pp. 298–313. Available at: https://doi.org/10.1038/s41575-019-0247-2.

Butler, M., Meer, L.T. van der and Leeuwen, F.N. van (2021) ‘Amino Acid Depletion Therapies: Starving Cancer Cells to Death’, *Trends in Endocrinology & Metabolism*, 32(6), pp. 367–381. Available at: https://doi.org/10.1016/j.tem.2021.03.003.

Byun, J.M. *et al.* (2023) ‘Frequency of serous tubal intraepithelial carcinoma (STIC) in patients with high grade serous ovarian cancer’, *Taiwanese Journal of Obstetrics & Gynecology*, 62(1), pp. 107–111. Available at: https://doi.org/10.1016/j.tjog.2022.09.006.

Castro-Portuguez, R. and Sutphin, G.L. (2020) ‘Kynurenine pathway, NAD+ synthesis, and mitochondrial function: targeting tryptophan metabolism to promote longevity and healthspan’, *Experimental gerontology*, 132, p. 110841. Available at: https://doi.org/10.1016/j.exger.2020.110841.

Cecchini, G. (2003) ‘Function and structure of complex II of the respiratory chain’, *Annual Review of Biochemistry*, 72, pp. 77–109. Available at: https://doi.org/10.1146/annurev.biochem.72.121801.161700.

Cerchione, C. *et al.* (2021) ‘IDH1/IDH2 Inhibition in Acute Myeloid Leukemia’, *Frontiers in Oncology*, 11. Available at: https://www.frontiersin.org/articles/10.3389/fonc.2021.639387 (Accessed: 22 February 2023).

Chaib, S., Tchkonia, T. and Kirkland, J.L. (2022) ‘Cellular senescence and senolytics: the path to the clinic’, *Nature Medicine*, 28(8), pp. 1556–1568. Available at: https://doi.org/10.1038/s41591-022-01923-y.

Chatterjee, N. and Walker, G.C. (2017) ‘Mechanisms of DNA damage, repair and mutagenesis’, *Environmental and molecular mutagenesis*, 58(5), p. 235. Available at: https://doi.org/10.1002/em.22087.

Chaudhry, R. and Varacallo, M. (2022) ‘Biochemistry, Glycolysis’, in *StatPearls*. Treasure Island (FL): StatPearls Publishing. Available at: http://www.ncbi.nlm.nih.gov/books/NBK482303/ (Accessed: 22 February 2023).

Chazotte, B. (2011) ‘Labeling mitochondria with MitoTracker dyes’, *Cold Spring Harbor Protocols*, 2011(8), pp. 990–992. Available at: https://doi.org/10.1101/pdb.prot5648.

Chen, L. *et al.* (2014) ‘Autophagy Inhibition Contributes to the Synergistic Interaction between EGCG and Doxorubicin to Kill the Hepatoma Hep3B Cells’, *PLOS ONE*, 9(1), p. e85771. Available at: https://doi.org/10.1371/journal.pone.0085771.

Chen, Q. and Ames, B.N. (1994) ‘Senescence-like growth arrest induced by hydrogen peroxide in human diploid fibroblast F65 cells’, *Proceedings of the National Academy of Sciences of the United States of America*, 91(10), pp. 4130–4134. Available at: https://doi.org/10.1073/pnas.91.10.4130.

Chen, Q.M., Liu, J. and Merrett, J.B. (2000) ‘Apoptosis or senescence-like growth arrest: influence of cell-cycle position, p53, p21 and bax in H2O2 response of normal human fibroblasts’, *The Biochemical Journal*, 347(Pt 2), pp. 543–551. Available at: https://doi.org/10.1042/0264-6021:3470543.

Chen, X. and Song, E. (2019) ‘Turning foes to friends: targeting cancer-associated fibroblasts’, *Nature Reviews. Drug Discovery*, 18(2), pp. 99–115. Available at: https://doi.org/10.1038/s41573-018-0004-1.

Chernoff, J. (2021) ‘The two-hit theory hits 50’, *Molecular Biology of the Cell*, 32(22), p. rt1. Available at: https://doi.org/10.1091/mbc.E21-08-0407.

Cheung, P.C. *et al.* (2000) ‘Characterization of AMP-activated protein kinase gamma-subunit isoforms and their role in AMP binding.’, *Biochemical Journal*, 346(Pt 3), pp. 659–669.

Chien, Y. *et al.* (2011) ‘Control of the senescence-associated secretory phenotype by NF-κB promotes senescence and enhances chemosensitivity’, *Genes & Development*, 25(20), pp. 2125–2136. Available at: https://doi.org/10.1101/gad.17276711.

Chikuma, S., Abbas, A.K. and Bluestone, J.A. (2005) ‘B7-independent inhibition of T cells by CTLA-4’, *Journal of Immunology (Baltimore, Md.: 1950)*, 175(1), pp. 177–181. Available at: https://doi.org/10.4049/jimmunol.175.1.177.

Childs, B.G. *et al.* (2014) ‘Senescence and apoptosis: dueling or complementary cell fates?’, *EMBO reports*, 15(11), pp. 1139–1153. Available at: https://doi.org/10.15252/embr.201439245.

Choudhary, C. *et al.* (2009) ‘Lysine acetylation targets protein complexes and co-regulates major cellular functions’, *Science (New York, N.Y.)*, 325(5942), pp. 834–840. Available at: https://doi.org/10.1126/science.1175371.

Chung, D.J. *et al.* (2009) ‘Indoleamine 2,3-dioxygenase-expressing mature human monocyte-derived dendritic cells expand potent autologous regulatory T cells’, *Blood*, 114(3), pp. 555–563. Available at: https://doi.org/10.1182/blood-2008-11-191197.

Cluntun, A.A. *et al.* (2015) ‘The rate of glycolysis quantitatively mediates specific histone acetylation sites’, *Cancer & Metabolism*, 3, p. 10. Available at: https://doi.org/10.1186/s40170-015-0135-3.

Cohn, R.L. *et al.* (2023) ‘The heterogeneity of cellular senescence: insights at the single-cell level’, *Trends in Cell Biology*, 33(1), pp. 9–17. Available at: https://doi.org/10.1016/j.tcb.2022.04.011.

Cojocaru, E., Parkinson, C.A. and Brenton, J.D. (2018) ‘Personalising Treatment for High-Grade Serous Ovarian Carcinoma’, *Clinical Oncology (Royal College of Radiologists (Great Britain))*, 30(8), pp. 515–524. Available at: https://doi.org/10.1016/j.clon.2018.05.008.

Cole, A.J. *et al.* (2016) ‘Assessing mutant p53 in primary high-grade serous ovarian cancer using immunohistochemistry and massively parallel sequencing’, *Scientific Reports*, 6(1), p. 26191. Available at: https://doi.org/10.1038/srep26191.

Colvin, E.K. and Howell, V.M. (2020) ‘Why the dual origins of high grade serous ovarian cancer matter’, *Nature Communications*, 11(1), p. 1200. Available at: https://doi.org/10.1038/s41467-020-15089-z.

Cooper, G.M. (2000) ‘The Development and Causes of Cancer’, *The Cell: A Molecular Approach. 2nd edition* [Preprint]. Available at: https://www.ncbi.nlm.nih.gov/books/NBK9963/ (Accessed: 23 February 2023).

Coppé, J.-P. *et al.* (2010) ‘The Senescence-Associated Secretory Phenotype: The Dark Side of Tumor Suppression’, *Annual review of pathology*, 5, pp. 99–118. Available at: https://doi.org/10.1146/annurev-pathol-121808-102144.

Corbet, C. and Feron, O. (2017) ‘Tumour acidosis: from the passenger to the driver’s seat’, *Nature Reviews. Cancer*, 17(10), pp. 577–593. Available at: https://doi.org/10.1038/nrc.2017.77.

Covarrubias, A.J. *et al.* (2021) ‘NAD+ metabolism and its roles in cellular processes during ageing’, *Nature reviews. Molecular cell biology*, 22(2), pp. 119–141. Available at: https://doi.org/10.1038/s41580-020-00313-x.

Cui, Y.-N. *et al.* (2017) ‘Enhanced intracellular delivery and controlled drug release of magnetic PLGA nanoparticles modified with transferrin’, *Acta Pharmacologica Sinica*, 38(6), pp. 943–953. Available at: https://doi.org/10.1038/aps.2017.45.

Curtin, N.J. and Szabo, C. (2020) ‘Poly(ADP-ribose) polymerase inhibition: past, present and future’, *Nature Reviews Drug Discovery*, 19(10), pp. 711–736. Available at: https://doi.org/10.1038/s41573-020-0076-6.

Curtis, N.J. *et al.* (2017) ‘Pre-clinical pharmacology of AZD3965, a selective inhibitor of MCT1: DLBCL, NHL and Burkitt’s lymphoma anti-tumor activity’, *Oncotarget*, 8(41), pp. 69219–69236. Available at: https://doi.org/10.18632/oncotarget.18215.

Dalmartello, M. *et al.* (2022) ‘European cancer mortality predictions for the year 2022 with focus on ovarian cancer’, *Annals of Oncology: Official Journal of the European Society for Medical Oncology*, 33(3), pp. 330–339. Available at: https://doi.org/10.1016/j.annonc.2021.12.007.

Dang, C.V. (2012) ‘MYC on the Path to Cancer’, *Cell*, 149(1), pp. 22–35. Available at: https://doi.org/10.1016/j.cell.2012.03.003.

Dang, L. *et al.* (2009) ‘Cancer-associated IDH1 mutations produce 2-hydroxyglutarate’, *Nature*, 462(7274), p. 739. Available at: https://doi.org/10.1038/nature08617.

Dauplat, J. *et al.* (2000) ‘Cytoreductive surgery for advanced stages of ovarian cancer’, *Seminars in Surgical Oncology*, 19(1), pp. 42–48. Available at: https://doi.org/10.1002/1098-2388(200007/08)19:1<42::aid-ssu7>3.0.co;2-m.

Davalli, P. *et al.* (2016) ‘ROS, Cell Senescence, and Novel Molecular Mechanisms in Aging and Age-Related Diseases’, *Oxidative Medicine and Cellular Longevity*, 2016, p. 3565127. Available at: https://doi.org/10.1155/2016/3565127.

De Pergola, G. and Silvestris, F. (2013) ‘Obesity as a Major Risk Factor for Cancer’, *Journal of Obesity*, 2013, p. 291546. Available at: https://doi.org/10.1155/2013/291546.

De Sousa Linhares, A. *et al.* (2019) ‘Therapeutic PD-L1 antibodies are more effective than PD-1 antibodies in blocking PD-1/PD-L1 signaling’, *Scientific Reports*, 9(1), p. 11472. Available at: https://doi.org/10.1038/s41598-019-47910-1.

Der, C.J. and Cooper, G.M. (1983) ‘Altered gene products are associated with activation of cellular rasK genes in human lung and colon carcinomas’, *Cell*, 32(1), pp. 201–208. Available at: https://doi.org/10.1016/0092-8674(83)90510-x.

Desai, M.M. and Fisher, D.S. (2007) ‘Beneficial Mutation–Selection Balance and the Effect of Linkage on Positive Selection’, *Genetics*, 176(3), pp. 1759–1798. Available at: https://doi.org/10.1534/genetics.106.067678.

Deshpande, O.A. and Mohiuddin, S.S. (2022) ‘Biochemistry, Oxidative Phosphorylation’, in *StatPearls*. Treasure Island (FL): StatPearls Publishing. Available at: http://www.ncbi.nlm.nih.gov/books/NBK553192/ (Accessed: 22 February 2023).

Di Blasio, S. *et al.* (2020) ‘The tumour microenvironment shapes dendritic cell plasticity in a human organotypic melanoma culture’, *Nature Communications*, 11(1), p. 2749. Available at: https://doi.org/10.1038/s41467-020-16583-0.

Dimri, G.P. *et al.* (1995) 'A biomarker that identifies senescent human cells in culture and in aging skin in vivo', *Proceedings of the National Academy of Sciences of the United States of America*, 92(20), pp. 9363–9367. Available at: https://doi.org/10.1073/pnas.92.20.9363.

Dodig, S., Čepelak, I. and Pavić, I. (2019) 'Hallmarks of senescence and aging', *Biochemia Medica*, 29(3), p. 030501. Available at: https://doi.org/10.11613/BM.2019.030501.

Doherty, J.R. *et al.* (2014) 'Blocking lactate export by inhibiting the Myc target MCT1 Disables glycolysis and glutathione synthesis', *Cancer Research*, 74(3), pp. 908–920. Available at: https://doi.org/10.1158/0008-5472.CAN-13-2034.

Ducommun, S. *et al.* (2015) 'Motif affinity and mass spectrometry proteomic approach for the discovery of cellular AMPK targets: identification of mitochondrial fission factor as a new AMPK substrate', *Cellular Signalling*, 27(5), pp. 978–988. Available at: https://doi.org/10.1016/j.cellsig.2015.02.008.

Eckert, M.A. *et al.* (2016) 'Genomics of Ovarian Cancer Progression Reveals Diverse Metastatic Trajectories Including Intraepithelial Metastasis to the Fallopian Tube', *Cancer Discovery*, 6(12), pp. 1342–1351. Available at: https://doi.org/10.1158/2159-8290.CD-16-0607.

Eikenes, L. *et al.* (2010) 'Effect of collagenase and hyaluronidase on free and anomalous diffusion in multicellular spheroids and xenografts', *Anticancer Research*, 30(2), pp. 359–368.

Erickson, B.K., Conner, M.G. and Landen, C.N. (2013) 'The role of the fallopian tube in the origin of ovarian cancer', *American Journal of Obstetrics and Gynecology*, 209(5), pp. 409–414. Available at: https://doi.org/10.1016/j.ajog.2013.04.019.

Falchook, G. *et al.* (2021) 'First-in-human study of the safety, pharmacokinetics, and pharmacodynamics of first-in-class fatty acid synthase inhibitor TVB-2640 alone and with a taxane in advanced tumors', *EClinicalMedicine*, 34, p. 100797. Available at: https://doi.org/10.1016/j.eclinm.2021.100797.

Färkkilä, A. *et al.* (2020) 'Immunogenomic profiling determines responses to combined PARP and PD-1 inhibition in ovarian cancer', *Nature Communications*, 11, p. 1459. Available at: https://doi.org/10.1038/s41467-020-15315-8.

Finkel, T. and Holbrook, N.J. (2000) 'Oxidants, oxidative stress and the biology of ageing', *Nature*, 408(6809), pp. 239–247. Available at: https://doi.org/10.1038/35041687.

Fischer, K. *et al.* (2007) 'Inhibitory effect of tumor cell-derived lactic acid on human T cells', *Blood*, 109(9), pp. 3812–3819. Available at: https://doi.org/10.1182/blood-2006-07-035972.

Flavin, R. *et al.* (2010) 'Fatty acid synthase as a potential therapeutic target in cancer', *Future Oncology*, 6(4), pp. 551–562. Available at: https://doi.org/10.2217/fon.10.11.

Fontaine, E. (2018) ‘Metformin-Induced Mitochondrial Complex I Inhibition: Facts, Uncertainties, and Consequences’, *Frontiers in Endocrinology*, 9, p. 753. Available at: https://doi.org/10.3389/fendo.2018.00753.

Fu, Z. *et al.* (2022) ‘Antibody drug conjugate: the “biological missile” for targeted cancer therapy’, *Signal Transduction and Targeted Therapy*, 7(1), pp. 1–25. Available at: https://doi.org/10.1038/s41392-022-00947-7.

Fullerton, M.D. *et al.* (2013) ‘Single phosphorylation sites in Acc1 and Acc2 regulate lipid homeostasis and the insulin-sensitizing effects of metformin’, *Nature Medicine*, 19(12), pp. 1649–1654. Available at: https://doi.org/10.1038/nm.3372.

Gadducci, A. *et al.* (2019) ‘Current strategies for the targeted treatment of high-grade serous epithelial ovarian cancer and relevance of BRCA mutational status’, *Journal of Ovarian Research*, 12(1), p. 9. Available at: https://doi.org/10.1186/s13048-019-0484-6.

Galluzzi, L. *et al.* (2013) ‘Metabolic targets for cancer therapy’, *Nature Reviews. Drug Discovery*, 12(11), pp. 829–846. Available at: https://doi.org/10.1038/nrd4145.

Galluzzi, L. *et al.* (2015) ‘Immunological Effects of Conventional Chemotherapy and Targeted Anticancer Agents’, *Cancer Cell*, 28(6), pp. 690–714. Available at: https://doi.org/10.1016/j.ccell.2015.10.012.

Garcia, D. and Shaw, R.J. (2017) ‘AMPK: Mechanisms of Cellular Energy Sensing and Restoration of Metabolic Balance’, *Molecular Cell*, 66(6), pp. 789–800. Available at: https://doi.org/10.1016/j.molcel.2017.05.032.

García-Cañaveras, J.C. and Lahoz, A. (2021) ‘Tumor Microenvironment-Derived Metabolites: A Guide to Find New Metabolic Therapeutic Targets and Biomarkers’, *Cancers*, 13(13), p. 3230. Available at: https://doi.org/10.3390/cancers13133230.

Garon, E.B. *et al.* (2014) ‘Dichloroacetate should be considered with platinum-based chemotherapy in hypoxic tumors rather than as a single agent in advanced non-small cell lung cancer’, *Journal of Cancer Research and Clinical Oncology*, 140(3), pp. 443–452. Available at: https://doi.org/10.1007/s00432-014-1583-9.

Giacomelli, A.O. *et al.* (2018) ‘Mutational processes shape the landscape of TP53 mutations in human cancer’, *Nature Genetics*, 50(10), pp. 1381–1387. Available at: https://doi.org/10.1038/s41588-018-0204-y.

Gillet, J.-P., Varma, S. and Gottesman, M.M. (2013) ‘The Clinical Relevance of Cancer Cell Lines’, *JNCI Journal of the National Cancer Institute*, 105(7), pp. 452–458. Available at: https://doi.org/10.1093/jnci/djt007.

Gocek, E. and Marcinkowska, E. (2011) ‘Differentiation Therapy of Acute Myeloid Leukemia’, *Cancers*, 3(2), pp. 2402–2420. Available at: https://doi.org/10.3390/cancers3022402.

Gómez-Valenzuela, F. *et al.* (2021) 'The Inflammatory Profile of the Tumor Microenvironment, Orchestrated by Cyclooxygenase-2, Promotes Epithelial-Mesenchymal Transition', *Frontiers in Oncology*, 11. Available at: https://www.frontiersin.org/articles/10.3389/fonc.2021.686792 (Accessed: 22 February 2023).

González, A. *et al.* (2008) 'Immunosuppression routed via the kynurenine pathway: a biochemical and pathophysiologic approach', *Advances in Clinical Chemistry*, 45, pp. 155–197. Available at: https://doi.org/10.1016/s0065-2423(07)00007-8.

Gordon, S. (2003) 'Alternative activation of macrophages', *Nature Reviews. Immunology*, 3(1), pp. 23–35. Available at: https://doi.org/10.1038/nri978.

Gremke, N. *et al.* (2020) 'mTOR-mediated cancer drug resistance suppresses autophagy and generates a druggable metabolic vulnerability', *Nature Communications*, 11(1), p. 4684. Available at: https://doi.org/10.1038/s41467-020-18504-7.

Gross, M.I. *et al.* (2014) 'Antitumor activity of the glutaminase inhibitor CB-839 in triple-negative breast cancer', *Molecular Cancer Therapeutics*, 13(4), pp. 890–901. Available at: https://doi.org/10.1158/1535-7163.MCT-13-0870.

Haddad, A. and Mohiuddin, S.S. (2022) 'Biochemistry, Citric Acid Cycle', in *StatPearls*. Treasure Island (FL): StatPearls Publishing. Available at: http://www.ncbi.nlm.nih.gov/books/NBK541072/ (Accessed: 22 February 2023).

Hanahan, D. (2022) 'Hallmarks of Cancer: New Dimensions', *Cancer Discovery*, 12(1), pp. 31–46. Available at: https://doi.org/10.1158/2159-8290.CD-21-1059.

Hanahan, D. and Weinberg, R.A. (2000) 'The hallmarks of cancer', *Cell*, 100(1), pp. 57–70. Available at: https://doi.org/10.1016/s0092-8674(00)81683-9.

Hanahan, D. and Weinberg, R.A. (2011) 'Hallmarks of cancer: the next generation', *Cell*, 144(5), pp. 646–674. Available at: https://doi.org/10.1016/j.cell.2011.02.013.

Hasan, N., Ohman, A.W. and Dinulescu, D.M. (2015) 'The promise and challenge of ovarian cancer models', *Translational cancer research*, 4(1), pp. 14–28. Available at: https://doi.org/10.3978/j.issn.2218-676X.2015.01.02.

Hatton, O. *et al.* (2012) 'Src Kinase and Syk Activation Initiate PI3K Signaling by a Chimeric Latent Membrane Protein 1 in Epstein-Barr Virus (EBV)+ B Cell Lymphomas', *PLoS ONE*, 7(8), p. e42610. Available at: https://doi.org/10.1371/journal.pone.0042610.

Hayflick, L. and Moorhead, P.S. (1961) 'The serial cultivation of human diploid cell strains', *Experimental Cell Research*, 25, pp. 585–621. Available at: https://doi.org/10.1016/0014-4827(61)90192-6.

Helleday, T. (2011) 'The underlying mechanism for the PARP and BRCA synthetic lethality: Clearing up the misunderstandings', *Molecular Oncology*, 5(4), pp. 387–393. Available at: https://doi.org/10.1016/j.molonc.2011.07.001.

Herzig, S. and Shaw, R.J. (2018) ‘AMPK: guardian of metabolism and mitochondrial homeostasis’, *Nature Reviews Molecular Cell Biology*, 19(2), pp. 121–135. Available at: https://doi.org/10.1038/nrm.2017.95.

Hitosugi, T. and Chen, J. (2014) ‘Post-translational modifications and the Warburg effect’, *Oncogene*, 33(34), pp. 4279–4285. Available at: https://doi.org/10.1038/onc.2013.406.

Huebner, R.J. and Todaro, G.J. (1969) ‘Oncogenes of RNA tumor viruses as determinants of cancer’, *Proceedings of the National Academy of Sciences of the United States of America*, 64(3), pp. 1087–1094. Available at: https://doi.org/10.1073/pnas.64.3.1087.

Jäger, S. *et al.* (2007) ‘AMP-activated protein kinase (AMPK) action in skeletal muscle via direct phosphorylation of PGC-1alpha’, *Proceedings of the National Academy of Sciences of the United States of America*, 104(29), pp. 12017–12022. Available at: https://doi.org/10.1073/pnas.0705070104.

Jiang, Y., Li, Y. and Zhu, B. (2015) ‘T-cell exhaustion in the tumor microenvironment’, *Cell Death & Disease*, 6(6), pp. e1792–e1792. Available at: https://doi.org/10.1038/cddis.2015.162.

Jiménez-Sánchez, A. *et al.* (2020) ‘Unraveling tumor-immune heterogeneity in advanced ovarian cancer uncovers immunogenic effect of chemotherapy’, *Nature Genetics*, 52(6), pp. 582–593. Available at: https://doi.org/10.1038/s41588-020-0630-5.

Jiricny, J. (2006) ‘The multifaceted mismatch-repair system’, *Nature Reviews. Molecular Cell Biology*, 7(5), pp. 335–346. Available at: https://doi.org/10.1038/nrm1907.

Kang, Z.-J. *et al.* (2016) ‘The Philadelphia chromosome in leukemogenesis’, *Chinese Journal of Cancer*, 35, p. 48. Available at: https://doi.org/10.1186/s40880-016-0108-0.

Kao, T.-W. *et al.* (2022) ‘Therapeutic Targeting of Glutaminolysis as a Novel Strategy to Combat Cancer Stem Cells’, *International Journal of Molecular Sciences*, 23(23), p. 15296. Available at: https://doi.org/10.3390/ijms232315296.

Karst, A.M. and Drapkin, R. (2012) ‘Primary culture and immortalization of human fallopian tube secretory epithelial cells.’, *Nature protocols*, 7(9), pp. 1755–1764. Available at: https://doi.org/10.1038/nprot.2012.097.

Karst, A.M., Levanon, K. and Drapkin, R. (2011) ‘Modeling high-grade serous ovarian carcinogenesis from the fallopian tube’, *Proceedings of the National Academy of Sciences*, 108(18), pp. 7547–7552. Available at: https://doi.org/10.1073/pnas.1017300108.

Katt, M.E. *et al.* (2016) 'In Vitro Tumor Models: Advantages, Disadvantages, Variables, and Selecting the Right Platform', *Frontiers in Bioengineering and Biotechnology*, 4. Available at: https://www.frontiersin.org/articles/10.3389/fbioe.2016.00012 (Accessed: 7 July 2023).

Kennel, S.J. *et al.* (2008) 'The fate of MAb-targeted Cd(125m)Te/ZnS nanoparticles in vivo', *Nuclear Medicine and Biology*, 35(4), pp. 501–514. Available at: https://doi.org/10.1016/j.nucmedbio.2008.02.001.

Khalid, A. *et al.* (2017) 'Strategies for improving drug delivery: Nanocarriers and microenvironmental priming', *Expert opinion on drug delivery*, 14(7), pp. 865–877. Available at: https://doi.org/10.1080/17425247.2017.1243527.

Khashaba, M. *et al.* (2022) 'Subtyping of high grade serous ovarian carcinoma: histopathological and immunohistochemical approach', *Journal of the Egyptian National Cancer Institute*, 34(1), p. 6. Available at: https://doi.org/10.1186/s43046-022-00104-9.

Kim, J. and DeBerardinis, R.J. (2019) 'Mechanisms and Implications of Metabolic Heterogeneity in Cancer', *Cell Metabolism*, 30(3), pp. 434–446. Available at: https://doi.org/10.1016/j.cmet.2019.08.013.

Kim, J.H. *et al.* (2011) 'High cleavage efficiency of a 2A peptide derived from porcine teschovirus-1 in human cell lines, zebrafish and mice', *PloS One*, 6(4), p. e18556. Available at: https://doi.org/10.1371/journal.pone.0018556.

Kindelberger, D.W. *et al.* (2007) 'Intraepithelial Carcinoma of the Fimbria and Pelvic Serous Carcinoma: Evidence for a Causal Relationship', *The American Journal of Surgical Pathology*, 31(2), p. 161. Available at: https://doi.org/10.1097/01.pas.0000213335.40358.47.

Kirschner, K. *et al.* (2020) 'Functional heterogeneity in senescence', *Biochemical Society Transactions*, 48(3), pp. 765–773. Available at: https://doi.org/10.1042/BST20190109.

Klemm, F. and Joyce, J.A. (2015) 'Microenvironmental regulation of therapeutic response in cancer', *Trends in cell biology*, 25(4), pp. 198–213. Available at: https://doi.org/10.1016/j.tcb.2014.11.006.

Koshiyama, M., Matsumura, N. and Konishi, I. (2014) 'Recent Concepts of Ovarian Carcinogenesis: Type I and Type II', *BioMed Research International*, 2014, p. 934261. Available at: https://doi.org/10.1155/2014/934261.

Koshiyama, M., Matsumura, N. and Konishi, I. (2017) 'Subtypes of Ovarian Cancer and Ovarian Cancer Screening', *Diagnostics*, 7(1), p. 12. Available at: https://doi.org/10.3390/diagnostics7010012.

Kozjak-Pavlovic, V. (2017) 'The MICOS complex of human mitochondria', *Cell and Tissue Research*, 367(1), pp. 83–93. Available at: https://doi.org/10.1007/s00441-016-2433-7.

Kroeger, P.T. and Drapkin, R. (2017) ‘Pathogenesis and heterogeneity of ovarian cancer’, *Current Opinion in Obstetrics & Gynecology*, 29(1), pp. 26–34. Available at: https://doi.org/10.1097/GCO.0000000000000340.

Kumari, R. and Jat, P. (2021) ‘Mechanisms of Cellular Senescence: Cell Cycle Arrest and Senescence Associated Secretory Phenotype’, *Frontiers in Cell and Developmental Biology*, 9. Available at: https://www.frontiersin.org/articles/10.3389/fcell.2021.645593 (Accessed: 16 February 2023).

Kurnasov, O. *et al.* (2003) ‘NAD Biosynthesis: Identification of the Tryptophan to Quinolinate Pathway in Bacteria’, *Chemistry & Biology*, 10(12), pp. 1195–1204. Available at: https://doi.org/10.1016/j.chembiol.2003.11.011.

Kwon, S.M. *et al.* (2019) ‘Metabolic features and regulation in cell senescence’, *BMB Reports*, 52(1), pp. 5–12. Available at: https://doi.org/10.5483/BMBRep.2019.52.1.291.

Labidi-Galy, S.I. *et al.* (2017a) ‘High grade serous ovarian carcinomas originate in the fallopian tube’, *Nature Communications*, 8(1), p. 1093. Available at: https://doi.org/10.1038/s41467-017-00962-1.

Labidi-Galy, S.I. *et al.* (2017b) ‘High grade serous ovarian carcinomas originate in the fallopian tube’, *Nature Communications*, 8(1), p. 1093. Available at: https://doi.org/10.1038/s41467-017-00962-1.

Lally, J.S.V. *et al.* (2019) ‘Inhibition of Acetyl-CoA Carboxylase by Phosphorylation or the Inhibitor ND-654 Suppresses Lipogenesis and Hepatocellular Carcinoma’, *Cell Metabolism*, 29(1), pp. 174-182.e5. Available at: https://doi.org/10.1016/j.cmet.2018.08.020.

Leach, D.R., Krummel, M.F. and Allison, J.P. (1996) ‘Enhancement of Antitumor Immunity by CTLA-4 Blockade’, *Science*, 271(5256), pp. 1734–1736. Available at: https://doi.org/10.1126/science.271.5256.1734.

Leanderson, P. and Tagesson, C. (1992) ‘Cigarette smoke-induced DNA damage in cultured human lung cells: role of hydroxyl radicals and endonuclease activation’, *Chemico-Biological Interactions*, 81(1–2), pp. 197–208. Available at: https://doi.org/10.1016/0009-2797(92)90034-i.

Lee, E.Y.H.P. and Muller, W.J. (2010) ‘Oncogenes and Tumor Suppressor Genes’, *Cold Spring Harbor Perspectives in Biology*, 2(10). Available at: https://doi.org/10.1101/cshperspect.a003236.

Lee, J.-Y. *et al.* (2018) ‘Changes in ovarian cancer survival during the 20 years before the era of targeted therapy’, *BMC Cancer*, 18, p. 601. Available at: https://doi.org/10.1186/s12885-018-4498-z.

Lee, M. *et al.* (2018) ‘Phosphorylation of Acetyl-CoA Carboxylase by AMPK Reduces Renal Fibrosis and Is Essential for the Anti-Fibrotic Effect of Metformin’, *Journal of the American Society of Nephrology : JASN*, 29(9), pp. 2326–2336. Available at: https://doi.org/10.1681/ASN.2018010050.

Lee, Y. *et al.* (2007) 'A candidate precursor to serous carcinoma that originates in the distal fallopian tube', *The Journal of Pathology*, 211(1), pp. 26–35. Available at: https://doi.org/10.1002/path.2091.

Lengyel, E. (2010) 'Ovarian Cancer Development and Metastasis', *The American Journal of Pathology*, 177(3), p. 1053. Available at: https://doi.org/10.2353/ajpath.2010.100105.

Li, C. *et al.* (2020) 'Regulatory T cells in tumor microenvironment: new mechanisms, potential therapeutic strategies and future prospects', *Molecular Cancer*, 19(1), p. 116. Available at: https://doi.org/10.1186/s12943-020-01234-1.

Li, J. *et al.* (2019) 'Enzymatic and nonenzymatic protein acetylations control glycolysis process in liver diseases', *The FASEB Journal*, 33(11), pp. 11640–11654. Available at: https://doi.org/10.1096/fj.201901175R.

Li, Z. *et al.* (2021) 'Non-immune Cell Components in the Gastrointestinal Tumor Microenvironment Influencing Tumor Immunotherapy', *Frontiers in Cell and Developmental Biology*, 9. Available at: https://www.frontiersin.org/articles/10.3389/fcell.2021.729941 (Accessed: 13 March 2023).

Ligresti, G. *et al.* (2009) 'PIK3CA mutations in human solid tumors', *Cell Cycle*, 8(9), pp. 1352–1358. Available at: https://doi.org/10.4161/cc.8.9.8255.

Lin, J. *et al.* (2002) 'Transcriptional co-activator PGC-1 alpha drives the formation of slow-twitch muscle fibres', *Nature*, 418(6899), pp. 797–801. Available at: https://doi.org/10.1038/nature00904.

Lisio, M.-A. *et al.* (2019) 'High-Grade Serous Ovarian Cancer: Basic Sciences, Clinical and Therapeutic Standpoints', *International Journal of Molecular Sciences*, 20(4), p. 952. Available at: https://doi.org/10.3390/ijms20040952.

Liu, Z. *et al.* (2017) 'Systematic comparison of 2A peptides for cloning multi-genes in a polycistronic vector', *Scientific Reports*, 7(1), p. 2193. Available at: https://doi.org/10.1038/s41598-017-02460-2.

Livak, K.J. and Schmittgen, T.D. (2001) 'Analysis of relative gene expression data using real-time quantitative PCR and the 2(-Delta Delta C(T)) Method', *Methods (San Diego, Calif.)*, 25(4), pp. 402–408. Available at: https://doi.org/10.1006/meth.2001.1262.

Low, P.S. and Kularatne, S.A. (2009) 'Folate-targeted therapeutic and imaging agents for cancer', *Current Opinion in Chemical Biology*, 13(3), pp. 256–262. Available at: https://doi.org/10.1016/j.cbpa.2009.03.022.

Lucas, H.B. *et al.* (2021) 'Factors Associated with Mutations: Their Matching Rates to Cardiovascular and Neurological Diseases', *International Journal of Molecular Sciences*, 22(10), p. 5057. Available at: https://doi.org/10.3390/ijms22105057.

Luengo, A., Gui, D.Y. and Vander Heiden, M.G. (2017) ‘Targeting Metabolism for Cancer Therapy’, *Cell Chemical Biology*, 24(9), pp. 1161–1180. Available at: https://doi.org/10.1016/j.chembiol.2017.08.028.

Luengo, A., Sullivan, L.B. and Heiden, M.G.V. (2014) ‘Understanding the complex-I-ty of metformin action: limiting mitochondrial respiration to improve cancer therapy’, *BMC Biology*, 12(1), p. 82. Available at: https://doi.org/10.1186/s12915-014-0082-4.

Luke, J.J. *et al.* (2019) ‘BMS-986205, an indoleamine 2, 3-dioxygenase 1 inhibitor (IDO1i), in combination with nivolumab (nivo): Updated safety across all tumor cohorts and efficacy in advanced bladder cancer (advBC).’, *Journal of Clinical Oncology*, 37(7_suppl), pp. 358–358. Available at: https://doi.org/10.1200/JCO.2019.37.7_suppl.358.

Luyckx, M. *et al.* (2022) ‘Recurrent High Grade Serous Ovarian Cancer Management’, in S. Lele (ed.) *Ovarian Cancer*. Brisbane (AU): Exon Publications. Available at: http://www.ncbi.nlm.nih.gov/books/NBK585985/ (Accessed: 22 June 2023).

Mahmood, R.D. *et al.* (2020) ‘First-Line Management of Advanced High-Grade Serous Ovarian Cancer’, *Current Oncology Reports*, 22(6), p. 64. Available at: https://doi.org/10.1007/s11912-020-00933-8.

Mantovani, F., Collavin, L. and Del Sal, G. (2019) ‘Mutant p53 as a guardian of the cancer cell’, *Cell Death & Differentiation*, 26(2), pp. 199–212. Available at: https://doi.org/10.1038/s41418-018-0246-9.

Martini, H. and Passos, J.F. (2023) ‘Cellular senescence: all roads lead to mitochondria’, *The FEBS Journal*, 290(5), pp. 1186–1202. Available at: https://doi.org/10.1111/febs.16361.

Martins, F.C. *et al.* (2022) ‘Clonal somatic copy number altered driver events inform drug sensitivity in high-grade serous ovarian cancer’, *Nature Communications*, 13(1), p. 6360. Available at: https://doi.org/10.1038/s41467-022-33870-0.

Mathews Samuel, S. *et al.* (2019) ‘Treatment with a Combination of Metformin and 2-Deoxyglucose Upregulates Thrombospondin-1 in Microvascular Endothelial Cells: Implications in Anti-Angiogenic Cancer Therapy’, *Cancers*, 11(11), p. 1737. Available at: https://doi.org/10.3390/cancers11111737.

McAnulty, J. and DiFeo, A. (2020) ‘The Molecular “Myc-anisms” behind Myc-Driven Tumorigenesis and the Relevant Myc-Directed Therapeutics’, *International Journal of Molecular Sciences*, 21(24), p. 9486. Available at: https://doi.org/10.3390/ijms21249486.

Mei, J. *et al.* (2021) ‘Cellular models of development of ovarian high-grade serous carcinoma: A review of cell of origin and mechanisms of carcinogenesis’, *Cell Proliferation*, 54(5), p. e13029. Available at: https://doi.org/10.1111/cpr.13029.

Mendler, A.N. *et al.* (2012) ‘Tumor lactic acidosis suppresses CTL function by inhibition of p38 and JNK/c-Jun activation’, *International Journal of Cancer*, 131(3), pp. 633–640. Available at: https://doi.org/10.1002/ijc.26410.

Mf, F. (1971) ‘Incessant ovulation--a factor in ovarian neoplasia?’, *Lancet (London, England)*, 2(7716). Available at: https://doi.org/10.1016/s0140-6736(71)92335-x.

Miwa, S. *et al.* (no date) ‘Mitochondrial dysfunction in cell senescence and aging’, *The Journal of Clinical Investigation*, 132(13), p. e158447. Available at: https://doi.org/10.1172/JCI158447.

Morris, J.D., Eddleston, A.L. and Crook, T. (1995) ‘Viral infection and cancer’, *Lancet (London, England)*, 346(8977), pp. 754–758. Available at: https://doi.org/10.1016/s0140-6736(95)91510-9.

Muller, P.A.J. and Vousden, K.H. (2013) ‘p53 mutations in cancer’, *Nature Cell Biology*, 15(1), pp. 2–8. Available at: https://doi.org/10.1038/ncb2641.

Munn, D.H. *et al.* (1999) ‘Inhibition of T Cell Proliferation by Macrophage Tryptophan Catabolism’, *The Journal of Experimental Medicine*, 189(9), pp. 1363–1372.

Muralidharan, R. *et al.* (2016) ‘Folate receptor-targeted nanoparticle delivery of HuR-RNAi suppresses lung cancer cell proliferation and migration’, *Journal of Nanobiotechnology*, 14(1), p. 47. Available at: https://doi.org/10.1186/s12951-016-0201-1.

Nakajima, J. *et al.* (2008) ‘Anti-tumor activity of ESX1 on cancer cells harboring oncogenic K-ras mutation’, *Biochemical and Biophysical Research Communications*, 370(1), pp. 189–194. Available at: https://doi.org/10.1016/j.bbrc.2008.03.062.

Nakamura, K. *et al.* (2017) ‘Reconstitution of high-grade serous ovarian carcinoma from primary fallopian tube secretory epithelial cells’, *Oncotarget*, 9(16), pp. 12609–12619. Available at: https://doi.org/10.18632/oncotarget.23035.

Nelson, G. *et al.* (2018) ‘The senescent bystander effect is caused by ROS-activated NF-κB signalling’, *Mechanisms of Ageing and Development*, 170, pp. 30–36. Available at: https://doi.org/10.1016/j.mad.2017.08.005.

Ni, R. *et al.* (2016) ‘Therapeutic inhibition of mitochondrial reactive oxygen species with mito-TEMPO reduces diabetic cardiomyopathy’, *Free Radical Biology & Medicine*, 90, pp. 12–23. Available at: https://doi.org/10.1016/j.freeradbiomed.2015.11.013.

Nolfi-Donegan, D., Braganza, A. and Shiva, S. (2020) ‘Mitochondrial electron transport chain: Oxidative phosphorylation, oxidant production, and methods of measurement’, *Redox Biology*, 37, p. 101674. Available at: https://doi.org/10.1016/j.redox.2020.101674.

Nordling, C.O. (1953) ‘A New Theory on the Cancer-inducing Mechanism’, *British Journal of Cancer*, 7(1), pp. 68–72.

Obrist, F. *et al.* (2018) ‘Metabolic vulnerability of cisplatin-resistant cancers’, *The EMBO Journal*, 37(14), p. e98597. Available at: https://doi.org/10.15252/embj.201798597.

Ogrunc, M. *et al.* (2014) ‘Oncogene-induced reactive oxygen species fuel hyperproliferation and DNA damage response activation’, *Cell Death and Differentiation*, 21(6), pp. 998–1012. Available at: https://doi.org/10.1038/cdd.2014.16.

Ohara, Y. *et al.* (2012) ‘Effective delivery of chemotherapeutic nanoparticles by depleting host Kupffer cells’, *International Journal of Cancer*, 131(10), pp. 2402–2410. Available at: https://doi.org/10.1002/ijc.27502.

O’Neil, N.J., Bailey, M.L. and Hieter, P. (2017) ‘Synthetic lethality and cancer’, *Nature Reviews Genetics*, 18(10), pp. 613–623. Available at: https://doi.org/10.1038/nrg.2017.47.

Opitz, C.A. *et al.* (2011) ‘An endogenous tumour-promoting ligand of the human aryl hydrocarbon receptor’, *Nature*, 478(7368), pp. 197–203. Available at: https://doi.org/10.1038/nature10491.

Ortiz-Montero, P., Londoño-Vallejo, A. and Vernot, J.-P. (2017) ‘Senescence-associated IL-6 and IL-8 cytokines induce a self- and cross-reinforced senescence/inflammatory milieu strengthening tumorigenic capabilities in the MCF-7 breast cancer cell line’, *Cell communication and signaling: CCS*, 15(1), p. 17. Available at: https://doi.org/10.1186/s12964-017-0172-3.

Otera, H. *et al.* (2010) ‘Mff is an essential factor for mitochondrial recruitment of Drp1 during mitochondrial fission in mammalian cells’, *The Journal of Cell Biology*, 191(6), pp. 1141–1158. Available at: https://doi.org/10.1083/jcb.201007152.

Parada, L.F. and Weinberg, R.A. (1983) ‘Presence of a Kirsten murine sarcoma virus ras oncogene in cells transformed by 3-methylcholanthrene.’, *Molecular and Cellular Biology*, 3(12), pp. 2298–2301.

Pathria, G. *et al.* (2018) ‘Targeting the Warburg effect via LDHA inhibition engages ATF4 signaling for cancer cell survival’, *The EMBO Journal*, 37(20), p. e99735. Available at: https://doi.org/10.15252/embj.201899735.

Patra, J.K. *et al.* (2018) ‘Nano based drug delivery systems: recent developments and future prospects’, *Journal of Nanobiotechnology*, 16(1), p. 71. Available at: https://doi.org/10.1186/s12951-018-0392-8.

Pearson, C.E., Edamura, K.N. and Cleary, J.D. (2005) ‘Repeat instability: mechanisms of dynamic mutations’, *Nature Reviews Genetics*, 6(10), pp. 729–742. Available at: https://doi.org/10.1038/nrg1689.

Perry, S.W. *et al.* (2011) ‘Mitochondrial membrane potential probes and the proton gradient: a practical usage guide’, *BioTechniques*, 50(2), pp. 98–115. Available at: https://doi.org/10.2144/000113610.

Petitprez, F. *et al.* (2020) 'The Tumor Microenvironment in the Response to Immune Checkpoint Blockade Therapies', *Frontiers in Immunology*, 11, p. 784. Available at: https://doi.org/10.3389/fimmu.2020.00784.

Poirier, M.C. (2004) 'Chemical-induced DNA damage and human cancer risk', *Nature Reviews Cancer*, 4(8), pp. 630–637. Available at: https://doi.org/10.1038/nrc1410.

Prakasam, G. *et al.* (2018) 'Posttranslational Modifications of Pyruvate Kinase M2: Tweaks that Benefit Cancer', *Frontiers in Oncology*, 8, p. 22. Available at: https://doi.org/10.3389/fonc.2018.00022.

Prat, J. (2015) 'FIGO's staging classification for cancer of the ovary, fallopian tube, and peritoneum: abridged republication', *Journal of Gynecologic Oncology*, 26(2), pp. 87–89. Available at: https://doi.org/10.3802/jgo.2015.26.2.87.

Prendergast, G.C. *et al.* (2018) 'Inflammatory reprogramming with IDO1 inhibitors: turning immunologically unresponsive "cold" tumors "hot"', *Trends in cancer*, 4(1), pp. 38–58. Available at: https://doi.org/10.1016/j.trecan.2017.11.005.

Purkey, H.E. *et al.* (2016) 'Cell Active Hydroxylactam Inhibitors of Human Lactate Dehydrogenase with Oral Bioavailability in Mice', *ACS medicinal chemistry letters*, 7(10), pp. 896–901. Available at: https://doi.org/10.1021/acsmedchemlett.6b00190.

Radziszewska, A.U. *et al.* (2018) 'Survival rates among women with ovarian cancers diagnosed in the area of Podkarpacie province in the years 1990–2015', *Contemporary Oncology*, 22(3), p. 151. Available at: https://doi.org/10.5114/wo.2018.78935.

Ray, P.D., Huang, B.-W. and Tsuji, Y. (2012) 'Reactive oxygen species (ROS) homeostasis and redox regulation in cellular signaling', *Cellular signalling*, 24(5), pp. 981–990. Available at: https://doi.org/10.1016/j.cellsig.2012.01.008.

Reid, B.M., Permuth, J.B. and Sellers, T.A. (2017) 'Epidemiology of ovarian cancer: a review', *Cancer Biology & Medicine*, 14(1), p. 9. Available at: https://doi.org/10.20892/j.issn.2095-3941.2016.0084.

Rheinbay, E. *et al.* (2020) 'Analyses of non-coding somatic drivers in 2,658 cancer whole genomes', *Nature*, 578(7793), pp. 102–111. Available at: https://doi.org/10.1038/s41586-020-1965-x.

Richard, D.M. *et al.* (2009) 'L-Tryptophan: Basic Metabolic Functions, Behavioral Research and Therapeutic Indications', *International Journal of Tryptophan Research : IJTR*, 2, pp. 45–60.

Robert, C. (2020) 'A decade of immune-checkpoint inhibitors in cancer therapy', *Nature Communications*, 11(1), p. 3801. Available at: https://doi.org/10.1038/s41467-020-17670-y.

Roboz, G.J. *et al.* (2020) 'Ivosidenib induces deep durable remissions in patients with newly diagnosed IDH1-mutant acute myeloid leukemia', *Blood*, 135(7), pp. 463–471. Available at: https://doi.org/10.1182/blood.2019002140.

Romero-Garcia, S. *et al.* (2016) ‘Lactate Contribution to the Tumor Microenvironment: Mechanisms, Effects on Immune Cells and Therapeutic Relevance’, *Frontiers in Immunology*, 7, p. 52. Available at: https://doi.org/10.3389/fimmu.2016.00052.

Rovillain, E. *et al.* (2011) ‘Activation of nuclear factor-kappa B signalling promotes cellular senescence’, *Oncogene*, 30(20), pp. 2356–2366. Available at: https://doi.org/10.1038/onc.2010.611.

Rudd, C.E., Taylor, A. and Schneider, H. (2009) ‘CD28 and CTLA-4 coreceptor expression and signal transduction’, *Immunological reviews*, 229(1), pp. 12–26. Available at: https://doi.org/10.1111/j.1600-065X.2009.00770.x.

Salminen, A., Kauppinen, A. and Kaarniranta, K. (2012) ‘Emerging role of NF-κB signaling in the induction of senescence-associated secretory phenotype (SASP)’, *Cellular Signalling*, 24(4), pp. 835–845. Available at: https://doi.org/10.1016/j.cellsig.2011.12.006.

Savitz, J. (2020) ‘The kynurenine pathway: a finger in every pie’, *Molecular Psychiatry*, 25(1), pp. 131–147. Available at: https://doi.org/10.1038/s41380-019-0414-4.

Schuch, A.P. *et al.* (2017) ‘Sunlight damage to cellular DNA: Focus on oxidatively generated lesions’, *Free Radical Biology & Medicine*, 107, pp. 110–124. Available at: https://doi.org/10.1016/j.freeradbiomed.2017.01.029.

Schwarz, R.F. *et al.* (2015) ‘Spatial and Temporal Heterogeneity in High-Grade Serous Ovarian Cancer: A Phylogenetic Analysis’, *PLoS Medicine*, 12(2), p. e1001789. Available at: https://doi.org/10.1371/journal.pmed.1001789.

Sedgwick, B. *et al.* (2007) ‘Repair of alkylated DNA: recent advances’, *DNA repair*, 6(4), pp. 429–442. Available at: https://doi.org/10.1016/j.dnarep.2006.10.005.

Serganova, I. *et al.* (2018) ‘LDH-A regulates the tumor microenvironment via HIF-signaling and modulates the immune response’, *PLoS ONE*, 13(9), p. e0203965. Available at: https://doi.org/10.1371/journal.pone.0203965.

Serio, P.A. de M.P. *et al.* (2021) ‘Somatic Mutational Profile of High-Grade Serous Ovarian Carcinoma and Triple-Negative Breast Carcinoma in Young and Elderly Patients: Similarities and Divergences’, *Cells*, 10(12), p. 3586. Available at: https://doi.org/10.3390/cells10123586.

Settembre, C. *et al.* (2013) ‘TFEB controls cellular lipid metabolism through a starvation-induced autoregulatory loop’, *Nature Cell Biology*, 15(6), pp. 647–658. Available at: https://doi.org/10.1038/ncb2718.

Setton, J. *et al.* (2021) ‘Synthetic Lethality in Cancer Therapeutics: The Next Generation’, *Cancer discovery*, 11(7), pp. 1626–1635. Available at: https://doi.org/10.1158/2159-8290.CD-20-1503.

Shan, F. *et al.* (2022) ‘Therapeutic targeting of regulatory T cells in cancer’, *Trends in Cancer*, 8(11), pp. 944–961. Available at: https://doi.org/10.1016/j.trecan.2022.06.008.

Shi, L. and Tu, B.P. (2015) ‘Acetyl-CoA and the Regulation of Metabolism: Mechanisms and Consequences’, *Current opinion in cell biology*, 33, pp. 125–131. Available at: https://doi.org/10.1016/j.ceb.2015.02.003.

Short, S. *et al.* (2019) ‘Senolytics and senostatics as adjuvant tumour therapy’, *EBioMedicine*, 41, pp. 683–692. Available at: https://doi.org/10.1016/j.ebiom.2019.01.056.

Sica, V. *et al.* (2019) ‘Lethal Poisoning of Cancer Cells by Respiratory Chain Inhibition plus Dimethyl α-Ketoglutarate’, *Cell Reports*, 27(3), pp. 820-834.e9. Available at: https://doi.org/10.1016/j.celrep.2019.03.058.

Simón, L. *et al.* (2022) ‘Role of the Pro-Inflammatory Tumor Microenvironment in Extracellular Vesicle-Mediated Transfer of Therapy Resistance’, *Frontiers in Oncology*, 12. Available at: https://www.frontiersin.org/articles/10.3389/fonc.2022.897205 (Accessed: 22 February 2023).

Sipos, A. *et al.* (2021) ‘The role of the microbiome in ovarian cancer: mechanistic insights into oncobiosis and to bacterial metabolite signaling’, *Molecular Medicine*, 27(1), p. 33. Available at: https://doi.org/10.1186/s10020-021-00295-2.

Siu, L.L. *et al.* (2017) ‘Abstract CT116: BMS-986205, an optimized indoleamine 2,3-dioxygenase 1 (IDO1) inhibitor, is well tolerated with potent pharmacodynamic (PD) activity, alone and in combination with nivolumab (nivo) in advanced cancers in a phase 1/2a trial’, *Cancer Research*, 77(13_Supplement), p. CT116. Available at: https://doi.org/10.1158/1538-7445.AM2017-CT116.

Smirnova, E. *et al.* (2001) ‘Dynamin-related protein Drp1 is required for mitochondrial division in mammalian cells’, *Molecular Biology of the Cell*, 12(8), pp. 2245–2256. Available at: https://doi.org/10.1091/mbc.12.8.2245.

Song, Y.S., Lee, B.Y. and Hwang, E.S. (2005) ‘Dinstinct ROS and biochemical profiles in cells undergoing DNA damage-induced senescence and apoptosis’, *Mechanisms of Ageing and Development*, 126(5), pp. 580–590. Available at: https://doi.org/10.1016/j.mad.2004.11.008.

Sonpavde, G. *et al.* (2020) ‘ENERGIZE: a Phase III study of neoadjuvant chemotherapy alone or with nivolumab with/without linrodostat mesylate for muscle-invasive bladder cancer’, *Future Oncology*, 16(2), pp. 4359–4368. Available at: https://doi.org/10.2217/fon-2019-0611.

Soto-Gamez, A. and Demaria, M. (2017) ‘Therapeutic interventions for aging: the case of cellular senescence’, *Drug Discovery Today*, 22(5), pp. 786–795. Available at: https://doi.org/10.1016/j.drudis.2017.01.004.

Spinelli, J.B. and Haigis, M.C. (2018) ‘The Multifaceted Contributions of Mitochondria to Cellular Metabolism’, *Nature cell biology*, 20(7), pp. 745–754. Available at: https://doi.org/10.1038/s41556-018-0124-1.

Srinivas, U.S. *et al.* (2019) ‘ROS and the DNA damage response in cancer’, *Redox Biology*, 25, p. 101084. Available at: https://doi.org/10.1016/j.redox.2018.101084.

Stein, E.M. *et al.* (2017) ‘Enasidenib in mutant IDH2 relapsed or refractory acute myeloid leukemia’, *Blood*, 130(6), pp. 722–731. Available at: https://doi.org/10.1182/blood-2017-04-779405.

Stein, G.H. *et al.* (1999) ‘Differential roles for cyclin-dependent kinase inhibitors p21 and p16 in the mechanisms of senescence and differentiation in human fibroblasts’, *Molecular and Cellular Biology*, 19(3), pp. 2109–2117. Available at: https://doi.org/10.1128/MCB.19.3.2109.

Stein, M. *et al.* (2010) ‘Targeting tumor metabolism with 2-deoxyglucose in patients with castrate-resistant prostate cancer and advanced malignancies’, *The Prostate*, 70(13), pp. 1388–1394. Available at: https://doi.org/10.1002/pros.21172.

Suarez-Arnedo, A. *et al.* (2020) ‘An image J plugin for the high throughput image analysis of in vitro scratch wound healing assays’, *PLoS ONE*, 15(7), p. e0232565. Available at: https://doi.org/10.1371/journal.pone.0232565.

Sun, S.-Y. (2010) ‘N-acetylcysteine, reactive oxygen species and beyond’, *Cancer biology & therapy*, 9(2), pp. 109–110.

Sutherl, J.V. and Bailar, J.C. (1984) ‘The multihit model of carcinogenesis: Etiologic implications for colon cancer’, *Journal of Chronic Diseases*, 37(6), pp. 465–480. Available at: https://doi.org/10.1016/0021-9681(84)90030-4.

Suzuki, T. *et al.* (2022) ‘Mutant KRAS drives metabolic reprogramming and autophagic flux in premalignant pancreatic cells’, *Cancer Gene Therapy*, 29(5), pp. 505–518. Available at: https://doi.org/10.1038/s41417-021-00326-4.

Tamura, I. *et al.* (2021) ‘The essential glucose transporter GLUT1 is epigenetically upregulated by C/EBPβ and WT1 during decidualization of the endometrium’, *The Journal of Biological Chemistry*, 297(4), p. 101150. Available at: https://doi.org/10.1016/j.jbc.2021.101150.

Tan, S.Y. *et al.* (2020) ‘Metformin and 2-Deoxyglucose Collaboratively Suppress Human CD4+ T Cell Effector Functions and Activation-Induced Metabolic Reprogramming’, *The Journal of Immunology*, 205(4), pp. 957–967. Available at: https://doi.org/10.4049/jimmunol.2000137.

Tang, X. *et al.* (2013) ‘Anti-tumour strategies aiming to target tumour-associated macrophages’, *Immunology*, 138(2), pp. 93–104. Available at: https://doi.org/10.1111/imm.12023.

Tarhini, A.A. and Iqbal, F. (2010) ‘CTLA-4 blockade: therapeutic potential in cancer treatments’, *OncoTargets and Therapy*, 3, pp. 15–25. Available at: https://doi.org/10.2147/ott.s4833.

Tarrado-Castellarnau, M., de Atauri, P. and Cascante, M. (2016) ‘Oncogenic regulation of tumor metabolic reprogramming’, *Oncotarget*, 7(38), pp. 62726–62753. Available at: https://doi.org/10.18632/oncotarget.10911.

Thiyagarajan, D.K., Basit, H. and Jeanmonod, R. (2022) ‘Physiology, Menstrual Cycle’, in *StatPearls*. Treasure Island (FL): StatPearls Publishing. Available at: http://www.ncbi.nlm.nih.gov/books/NBK500020/ (Accessed: 23 February 2023).

Thomson, D.M., Fick, C.A. and Gordon, S.E. (2008) ‘AMPK activation attenuates S6K1, 4E-BP1, and eEF2 signaling responses to high-frequency electrically stimulated skeletal muscle contractions’, *Journal of Applied Physiology (Bethesda, Md.: 1985)*, 104(3), pp. 625–632. Available at: https://doi.org/10.1152/japplphysiol.00915.2007.

Tong, X., Zhao, F. and Thompson, C.B. (2009) ‘The molecular determinants of de novo nucleotide biosynthesis in cancer cells’, *Current Opinion in Genetics & Development*, 19(1), pp. 32–37. Available at: https://doi.org/10.1016/j.gde.2009.01.002.

Torre, L.A. *et al.* (2018) ‘Ovarian Cancer Statistics, 2018’, *CA: a cancer journal for clinicians*, 68(4), pp. 284–296. Available at: https://doi.org/10.3322/caac.21456.

Torsvik, A. *et al.* (2014) ‘U-251 revisited: genetic drift and phenotypic consequences of long-term cultures of glioblastoma cells’, *Cancer Medicine*, 3(4), pp. 812–824. Available at: https://doi.org/10.1002/cam4.219.

Toyama, E.Q. *et al.* (2016) ‘AMP-activated protein kinase mediates mitochondrial fission in response to energy stress’, *Science (New York, N.Y.)*, 351(6270), pp. 275–281. Available at: https://doi.org/10.1126/science.aab4138.

Trefts, E. and Shaw, R.J. (2021) ‘AMPK: restoring metabolic homeostasis over space and time’, *Molecular Cell*, 81(18), pp. 3677–3690. Available at: https://doi.org/10.1016/j.molcel.2021.08.015.

Tuna, M. *et al.* (2020) ‘Clinical relevance of TP53 hotspot mutations in high-grade serous ovarian cancers’, *British Journal of Cancer*, 122(3), pp. 405–412. Available at: https://doi.org/10.1038/s41416-019-0654-8.

Turner, M.C. *et al.* (2020) ‘Outdoor Air Pollution and Cancer: An Overview of the Current Evidence and Public Health Recommendations’, *CA: a cancer journal for clinicians*, p. 10.3322/caac.21632. Available at: https://doi.org/10.3322/caac.21632.

Van Deursen and M, J. (2014) ‘The role of senescent cells in ageing’, *Nature*, 509(7501), pp. 439–446. Available at: https://doi.org/10.1038/nature13193.

Walsh, R.J., Sundar, R. and Lim, J.S.J. (2023) ‘Immune checkpoint inhibitor combinations—current and emerging strategies’, *British Journal of Cancer*, 128(8), pp. 1415–1417. Available at: https://doi.org/10.1038/s41416-023-02181-6.

Wang, L., Lankhorst, L. and Bernards, R. (2022) ‘Exploiting senescence for the treatment of cancer’, *Nature Reviews Cancer*, 22(6), pp. 340–355. Available at: https://doi.org/10.1038/s41568-022-00450-9.

Wang, S. *et al.* (2019) ‘Induction of ROS and DNA damage-dependent senescence by icaritin contributes to its antitumor activity in hepatocellular carcinoma cells’, *Pharmaceutical Biology*, 57(1), pp. 424–431. Available at: https://doi.org/10.1080/13880209.2019.1628073.

Wang, X. *et al.* (2016) ‘PD-L1 expression in human cancers and its association with clinical outcomes’, *OncoTargets and therapy*, 9, pp. 5023–5039. Available at: https://doi.org/10.2147/OTT.S105862.

Warburg, O. (1956) ‘On the origin of cancer cells’, *Science (New York, N.Y.)*, 123(3191), pp. 309–314. Available at: https://doi.org/10.1126/science.123.3191.309.

Warren, H.S. *et al.* (2015) ‘Mice are not men’, *Proceedings of the National Academy of Sciences of the United States of America*, 112(4), p. E345. Available at: https://doi.org/10.1073/pnas.1414857111.

Wei, R. *et al.* (2020) ‘Cellular and Extracellular Components in Tumor Microenvironment and Their Application in Early Diagnosis of Cancers’, *Analytical Cellular Pathology (Amsterdam)*, 2020, p. 6283796. Available at: https://doi.org/10.1155/2020/6283796.

Weinberg, F., Ramnath, N. and Nagrath, D. (2019) ‘Reactive Oxygen Species in the Tumor Microenvironment: An Overview’, *Cancers*, 11(8), p. 1191. Available at: https://doi.org/10.3390/cancers11081191.

Wiley, C.D. *et al.* (2016) ‘Mitochondrial Dysfunction Induces Senescence with a Distinct Secretory Phenotype’, *Cell Metabolism*, 23(2), pp. 303–314. Available at: https://doi.org/10.1016/j.cmet.2015.11.011.

Wiley, C.D. and Campisi, J. (2021) ‘The metabolic roots of senescence: mechanisms and opportunities for intervention’, *Nature Metabolism*, 3(10), pp. 1290–1301. Available at: https://doi.org/10.1038/s42255-021-00483-8.

Wise, D.R. *et al.* (2008) ‘Myc regulates a transcriptional program that stimulates mitochondrial glutaminolysis and leads to glutamine addiction’, *Proceedings of the National Academy of Sciences of the United States of America*, 105(48), pp. 18782–18787. Available at: https://doi.org/10.1073/pnas.0810199105.

Wise, D.R. and Thompson, C.B. (2010) ‘Glutamine Addiction: A New Therapeutic Target in Cancer’, *Trends in biochemical sciences*, 35(8), pp. 427–433. Available at: https://doi.org/10.1016/j.tibs.2010.05.003.

Woodward, G.E. and Hudson, M.T. (1954) ‘The effect of 2-desoxy-D-glucose on glycolysis and respiration of tumor and normal tissues’, *Cancer Research*, 14(8), pp. 599–605.

Wu, C.-W. and Storey, K.B. (2021) ‘mTOR Signaling in Metabolic Stress Adaptation’, *Biomolecules*, 11(5), p. 681. Available at: https://doi.org/10.3390/biom11050681.

Wu, S.-G. *et al.* (2019) ‘Real-World Impact of Survival by Period of Diagnosis in Epithelial Ovarian Cancer Between 1990 and 2014’, *Frontiers in Oncology*, 9, p. 639. Available at: https://doi.org/10.3389/fonc.2019.00639.

Wu, Y. *et al.* (1997) ‘CTLA-4–B7 Interaction Is Sufficient to Costimulate T Cell Clonal Expansion’, *The Journal of Experimental Medicine*, 185(7), pp. 1327–1336.

Wu, Z. *et al.* (1999) ‘Mechanisms controlling mitochondrial biogenesis and respiration through the thermogenic coactivator PGC-1’, *Cell*, 98(1), pp. 115–124. Available at: https://doi.org/10.1016/S0092-8674(00)80611-X.

Xiao, W. *et al.* (2018) ‘NAD(H) and NADP(H) Redox Couples and Cellular Energy Metabolism’, *Antioxidants & Redox Signaling*, 28(3), pp. 251–272. Available at: https://doi.org/10.1089/ars.2017.7216.

Xie, H. *et al.* (2014) ‘Targeting lactate dehydrogenase--a inhibits tumorigenesis and tumor progression in mouse models of lung cancer and impacts tumor-initiating cells’, *Cell Metabolism*, 19(5), pp. 795–809. Available at: https://doi.org/10.1016/j.cmet.2014.03.003.

Xu, L. *et al.* (2020) ‘Mitochondrial superoxide contributes to oxidative stress exacerbated by DNA damage response in RAD51-depleted ovarian cancer cells’, *Redox Biology*, 36, p. 101604. Available at: https://doi.org/10.1016/j.redox.2020.101604.

Yamulla, R.J. *et al.* (2020) ‘Most Commonly Mutated Genes in High-Grade Serous Ovarian Carcinoma Are Nonessential for Ovarian Surface Epithelial Stem Cell Transformation’, *Cell Reports*, 32(9), p. 108086. Available at: https://doi.org/10.1016/j.celrep.2020.108086.

Yang, Yanfei *et al.* (2020) ‘Tumor Microenvironment in Ovarian Cancer: Function and Therapeutic Strategy’, *Frontiers in Cell and Developmental Biology*, 8. Available at: https://www.frontiersin.org/articles/10.3389/fcell.2020.00758 (Accessed: 22 February 2023).

Yaniz, E. *et al.* (2020) ‘Impact of chemotherapy alone or in combination with an anti-angiogenic on the immune tumor microenvironment (TME) of ovarian cancer: Data from the randomized CHIVA trial (a GINECO –GINEGEPS study).’, *Journal of Clinical Oncology*, 38(15_suppl), pp. 6011–6011. Available at: https://doi.org/10.1200/JCO.2020.38.15_suppl.6011.

Yao, Y. *et al.* (2020) ‘Nanoparticle-Based Drug Delivery in Cancer Therapy and Its Role in Overcoming Drug Resistance’, *Frontiers in Molecular Biosciences*, 7. Available at: https://www.frontiersin.org/articles/10.3389/fmolb.2020.00193 (Accessed: 18 February 2023).

Yi, M. *et al.* (2021) ‘Regulation of PD-L1 expression in the tumor microenvironment’, *Journal of Hematology & Oncology*, 14(1), p. 10. Available at: https://doi.org/10.1186/s13045-020-01027-5.

Yoo, H.C. *et al.* (2020) ‘Glutamine reliance in cell metabolism’, *Experimental & Molecular Medicine*, 52(9), pp. 1496–1516. Available at: https://doi.org/10.1038/s12276-020-00504-8.

Yue, X. *et al.* (2017) ‘Mutant p53 in cancer: accumulation, gain-of-function and therapy’, *Journal of molecular biology*, 429(11), pp. 1595–1606. Available at: https://doi.org/10.1016/j.jmb.2017.03.030.

Ždralević, M. *et al.* (2018) ‘Double genetic disruption of lactate dehydrogenases A and B is required to ablate the “Warburg effect” restricting tumor growth to oxidative metabolism’, *The Journal of Biological Chemistry*, 293(41), pp. 15947–15961. Available at: https://doi.org/10.1074/jbc.RA118.004180.

Zhang, J. *et al.* (2020) ‘The Functional Effects of Key Driver KRAS Mutations on Gene Expression in Lung Cancer’, *Frontiers in Genetics*, 11, p. 17. Available at: https://doi.org/10.3389/fgene.2020.00017.

Zhang, L. *et al.* (2023) ‘Targeting cellular senescence with senotherapeutics: senolytics and senomorphics’, *The FEBS Journal*, 290(5), pp. 1362–1383. Available at: https://doi.org/10.1111/febs.16350.

Zhang, S. *et al.* (2019) ‘Both fallopian tube and ovarian surface epithelium are cells-of-origin for high-grade serous ovarian carcinoma’, *Nature Communications*, 10(1), p. 5367. Available at: https://doi.org/10.1038/s41467-019-13116-2.

Zhang, X. *et al.* (2015) ‘Thyroid-stimulating hormone decreases HMG-CoA reductase phosphorylation via AMP-activated protein kinase in the liver’, *Journal of Lipid Research*, 56(5), pp. 963–971. Available at: https://doi.org/10.1194/jlr.M047654.

Zhang, Z. *et al.* (2020) ‘T Cell Dysfunction and Exhaustion in Cancer’, *Frontiers in Cell and Developmental Biology*, 8. Available at: https://www.frontiersin.org/articles/10.3389/fcell.2020.00017 (Accessed: 22 February 2023).

Zhao, D. *et al.* (2013) ‘Lysine-5 Acetylation Negatively Regulates Lactate Dehydrogenase A and Is Decreased in Pancreatic Cancer’, *Cancer cell*, 23(4), p. 10.1016/j.ccr.2013.02.005. Available at: https://doi.org/10.1016/j.ccr.2013.02.005.

Zhao, J. *et al.* (2019) ‘Low-dose 2-deoxyglucose and metformin synergically inhibit proliferation of human polycystic kidney cells by modulating glucose metabolism’, *Cell Death Discovery*, 5(1), pp. 1–13. Available at: https://doi.org/10.1038/s41420-019-0156-8.

ZHENG, J. (2012) ‘Energy metabolism of cancer: Glycolysis versus oxidative phosphorylation (Review)’, *Oncology Letters*, 4(6), pp. 1151–1157. Available at: https://doi.org/10.3892/ol.2012.928.

Zhu, Y. *et al.* (2015) ‘The Achilles’ heel of senescent cells: from transcriptome to senolytic drugs’, *Aging Cell*, 14(4), pp. 644–658. Available at: https://doi.org/10.1111/acel.12344.

Zhuo, S. *et al.* (2020) ‘pH-Sensitive Biomaterials for Drug Delivery’, *Molecules*, 25(23). Available at: https://doi.org/10.3390/molecules25235649.

DANKSAGUNG

Zu aller erst möchte ich mich bei Herrn Prof. Dr. Lienhard Schmitz für sein stetiges Vertrauen, seine Unterstützung und seine Rückendeckung bedanken. Die vielen Stunden lehrreicher Diskussionen haben erheblich zum Projekt, aber auch zu meiner eigenen Weiterentwicklung beigetragen. Ich konnte mich immer auf dich verlassen, was mir die nötige Sicherheit in den Talfahrten des Projekts gegeben hat. Vielen Dank für dieses Projekt und deine außerordentliche Betreuung!

Auch möchte ich mich bei Herrn. Prof. Dr. Reinhard Dammann für die Erstbetreuung und die Begutachtung der Dissertation bedanken. Bei Frau Prof. Dr. S. Hake möchte ich mich für ihre Bereitschaft, mich und meine Arbeit zu prüfen, bedanken. Ganz besonderer Dank gilt Prof. Dr. Tilman Borggrefe. Deine Tipps, Ideen und Diskussionen in den letzten Jahren haben mir sehr geholfen und mich motiviert. Auch möchte ich mich, für deine Bereitschaft mich zu prüfen, bedanken.

Ich möchte mich zudem bei allen Mitgliedern des GRK2573 für die lehrreiche Zeit bedanken. Besonderer Dank gilt meinem Thesis-Betreuungs-Komitee, bestehend neben Prof. Dr. Lienhard Schmitz, aus den Herrn Professoren Michael Kracht und Thorsten Stiewe, die einen großen Einfluss auf dieses Projekt hatten und noch haben.

Obwohl meine Kollaborationspartner in dieser Arbeit aufgelistet sind, möchte ich mich noch einmal bei denen bedanken, die einen größeren Anteil an den Ergebnissen dieser Arbeit aber auch der folgenden Publikation hatten und noch haben werden: Dr. Ulrich Gärtner, Dr. Stephan Klatt, Prof. Dr. Marek Bartkuhn, Dr. Jochen Wilhelm, Prof. Dr. Thorsten Stiewe, Dr. Sabrina Elmshäuser, Prof. Dr. Johannes Graumann.

Großer Dank richtet sich an meine Kollegen, ehemalig oder aktuell. Die Arbeitsatmosphäre ist mit einer der wichtigsten Dinge und können einem so manch schlechten Tag retten. Danke Susanne Bacher, Vera Saul, Maja Treusch,

Olesja Ritter, Ratnal Belapurkar, Shashi Chillappagari, Lu Liu, Roman Robert, Kristin Ott, Lena Schmidt, Amelie Pritz, Martin Brockhaus, Jasmin Priester.

Besonders großer Dank gilt Maximilian Pfisterer. Meine Doktorandenzeit wäre ohne dich um einiges weniger erträglich gewesen. Unsere Diskussionen und deine herausragende Fähigkeit (Brillanz), Probleme zu lösen, hatten erheblichen Anteil an vielen Aspekten dieser Arbeit. Vielen Dank für deine Freundschaft!

Diese Arbeit wäre ohne Julia Stengel, Till Wöckener und David van den Borre, Medizindoktoranden die ich zusammengerechnet 1.5 Jahre betreuen durfte, noch längst nicht da wo sie Momentan steht. Ihr seid jeden Extrameter gegangen den ihr gehen konntet. Dafür und für die wunderschöne Zeit mit euch bin ich sehr dankbar.

Bei Ines Höfliger, Yvonne Horn, Markus Schwinn und Regina Jilg möchte ich mich für eure exzellente organisatorische und technische Unterstützung in den letzten Jahren bedanken. Ihr macht einem das Doktoranden Dasein um einiges leichter. Vielen Dank für alles!

Ohne meine Familie wäre ich nicht dazu in der Lage gewesen, diesen Weg zu gehen. Petra und Achim, ihr seid mir in jeglicher Hinsicht ein Vorbild. Ich bin froh eine so wundervolle Schwester zu haben. Auch möchte ich meinen Großeltern Hilde und Walter, Helmi, sowie meinem Onkel Jürgen für alles was ihr für mich getan habt bedanken. Die Dankbarkeit die ich für euch empfinde lässt sich nicht in Worte fassen.

Danke an meine Freunde aus der Heimat und auch aus Gießen. Immer wenn wir etwas unternehmen bin ich zu Hause. Vielen Dank für alles.

Mein größter Dank gilt meiner Freundin Franziska. Deine Liebe und Unterstützung in den letzten Jahren haben mich und damit dieses Projekt getragen.
Du bist meine mit Abstand wichtigste „Entdeckung“!